

The Development of Novel Model Systems and Imaging Techniques to Advance the Understanding of Calcific Aortic Valve Disease

A dissertation submitted by

Lauren Michelle Baugh

In partial fulfillment of the requirements for the degree of

Doctor in Philosophy

In

Biomedical Engineering

May 2018

Advisor: Lauren D. Black III, PhD

Research Committee:

Lauren D. Black III

Elena Aikawa

Irene Georgakoudi

Philip Hinds

Gordon Huggins

© 2018 Lauren Michelle Baugh

Abstract

As a leading cause of cardiovascular morbidity and mortality, calcific aortic valve disease (CAVD) is responsible for significant health and cost burden around the world. While valve replacement surgery can improve quality of life and increase life expectancy, it is not without risks and costs. However, this is currently the only method available to treat CAVD since a lack of understanding surrounding the disease mechanisms has hindered the development of pharmaceutical interventions. In order to improve our understanding of valve stenosis and calcification, in the hopes of expanding the range of treatment methods for CAVD, we study several aspects of the disease and have developed an imaging method that non-destructively captures mineralization in tissues and *in vitro* culture.

Stenosis and calcification of valve tissue is accompanied by significant changes to the extracellular matrix (ECM) structure and composition. To discern how these variations in ECM could affect valve interstitial cells (VICs) – the most abundant cell type in valve tissue – we developed both *in vitro* and *in vivo* model systems. A 2D, polyacrylamide (PAAM) gel-based cell culture platform showed that hyaluronic acid (HA), an ECM protein found in large abundance in the aortic valve, increased VIC mineralization, but that effect could be mitigated through siRNA knockdown of the HA binding protein CD44. We also developed a Tie2-cre mediated conditional knockout (cKO) of the retinoblastoma protein (pRb) in a mouse model which, compared to control mice, showed increased aortic valve stenosis with age. Significant alterations to the valve leaflet ECM organization and protein composition (as measured by proteomics analysis) were also seen in cKO pRb mice leading to the conclusion that this mouse model may be a useful system for studying CAVD.

To further visualize changes to aortic valve tissue, we also developed a novel imaging technique that used endogenous two-photon excited fluorescence signal from calcific nodules to measure mineralization content. We termed this the mineralization associated fluorescence (MAF). MAF as a quantitative measure of calcification was confirmed using human and mouse valve tissue, rat bone, and the 2D PAAM gel *in vitro* model system. Interestingly, time lapse imaging of our *in vitro* cell culture platform allowed us to measure calcific nodule growth in real time. During the course of the experiment, we noted varying rates of development and growth rates of mineralization which further emphasizes the variability that can occur during valve calcification. Lastly, to further the understanding of the effect ECM proteins can have on valve mineralization, we created a methacrylated hyaluronic acid (MeHA)-based 3D model. To investigate cell response, we can incorporate ECM proteins, identified through the transcriptomic approach of RNA sequencing, into the MeHA gels. Utilizing VICs, we can evaluate the effect of MeHA gel composition on mineralization over time. Using the non-destructive imaging approach that we developed, as well as other nonlinear microscopy techniques, we can track calcification and cell response. Overall, the research described in this thesis highlights the importance of taking a multipronged approach to further the understanding of CAVD with the goal of developing more effective treatment methods.

Acknowledgements

I would like to start by thanking my thesis advisor and mentor Professor Lauren D. Black, III. Sharing our first names isn't the only thing we have in common and I have enjoyed both his friendship and mentorship during the course of my PhD. Lauren allowed me to explore and be creative with my research while always pushing me to do and learn more. His passion for science has allowed me to truly embrace my own love of the subject and I don't think I'll ever stop asking questions. I'm very grateful Lauren was willing to take a chance on me when I first started at Tufts, coming from the seemingly unrelated background of aerospace engineering, and allowed me the time and space to learn confidence in myself. In the past five years, Lauren has helped me grow more confident in myself as a person and as a researcher and I am very grateful to have been a part of his lab.

I am also very thankful to my thesis committee members Professors Elena Aikawa, Irene Georgakoudi, Philip Hinds, and Gordon Huggins; your support and mentorship over the past several years has been greatly appreciated. Elena, your enthusiasm and encouragement was always wonderful to hear and you have been an inspiration in the field of valve disease research. Irene, thank you for letting me use all of your microscopes and for your patience in teaching me how to improve my signal processing, Matlab coding, and writing. Phil and Gordon, thank you for always taking time out of your busy schedules to answer my questions and provide your valuable input.

I am also very grateful to both current and former members of the Black Lab; you made coming to work each day a pleasure. Kelly Sullivan, Kathy Ye Morgan, and Corin Williams

thank you for your mentorship, friendship, lunch dates and for always talking me through my stressful situations. Kathy and Kelly, thank you for paving the way to a PhD in Lauren's lab, your advice was always helpful and appreciated. Kathy, I'll never forget your thorough explanation of Western blotting procedures and advice on all my early experiments. Corin, your detailed lab notebooks were so helpful and an aspiration that I don't think I'll ever achieve. Kelly, I don't know that I would have made it through without your help, guidance and overall support; I also owe my expanded scientific vocabulary to you. Additionally, I would like to thank former Black Lab members Albert Gao and Anthony Rinaldi; your continued friendship has made my graduate school experience worth having. To the current Lab members, Whitney Stoppel, Bre Duffy, Yuqi Wang, Matt Watson, Spencer Fenn, Beth Porter, Luke Perreault, Mark Daley, and Rozanne Mungai, thank you for your support and for making the lab a fun and productive environment. I know you all will achieve great things (because you already have!). I would also like to thank Whitney for all her guidance and help the past four years and to wish her good luck in her next role as a Professor! Also, to Bre, thanks for all our late-night lab talks – good luck being the senior lab member and keep bringing the Arizona heat to Boston! In addition to my fellow lab members, I would also like to thank everyone in the Tufts Biomedical Engineering department for their support over the years – especially to Milva Ricci and Laura Suarez, you guys saved me from my poor planning many times!

Lastly, I would like to thank my family because without your unwavering support, I would not be where I am today. Mom, your confidence in me, even when I doubted myself completely, was always above and beyond what I could hope for. Dad, your overwhelming interest and enthusiasm in my work is incredibly uplifting and appreciated. I would also like to thank my Nana, Nancy Melvin, my Aunt Cynthia and Uncle Matt Fitzgibbon, and

my in-laws Roy, Liza, and Priya Punnoose for your support and encouragement. Finally, to my husband, Andrew: words cannot express how much your love, support and faith in me has meant. I feel incredibly lucky to have had you by my side and to be able to count on your continued love and support.

Table of Contents

Chapter 1.	Introduction and Background.....	1
1.1.1	Introduction and Motivation	1
1.1.2	Valve Anatomy and Normal Function.....	3
1.1.3	Valve Cell Populations and Response to Disease.....	4
1.1.4	Extracellular Matrix in the Valve.....	7
1.1.5	Current Models of CAVD	9
1.1.6	The Use of Imaging Modalities to Study CAVD	10
1.2	Conclusion.....	12
Chapter 2.	CD44 Signaling Modulates Valve Interstitial Cell Calcification in Vitro	13
2.1	Introduction	14
2.2	Methods.....	17
2.2.1	Substrate Preparation	17
2.2.2	Cell Culture	18
2.2.3	Nodule Characterization.....	19
2.2.4	CD44 Blocking with Antibody	20
2.2.5	Immunohistochemistry	20
2.2.6	Transfection with siRNA	21
2.2.7	Western Blotting	22
2.2.8	Quantitative PCR	23
2.2.9	Statistics	23

2.3	Results.....	24
2.3.1	Nodules grown on HA gels grew significantly larger nodules than those on Collagen 24	
2.3.2	ECM binding protein determines cell spreading.....	25
2.3.3	siRNA knockdown of CD44 decreases mineralization.....	26
2.3.4	Knockdown of RHAMM leads to increase in apoptotic markers while CD44 Knockdown shows an increase in osteogenic markers	27
2.4	Discussion.....	29
2.5	Conclusion.....	32
2.6	Figures.....	33
Chapter 3. Conditional deletion of RB1 in the Tie2 lineage leads to aortic valve regurgitation 45		
3.1	Introduction	46
3.2	Methods.....	48
3.2.1	Animals.....	48
3.2.2	Echocardiography.....	50
3.2.3	Blood Pressure Measurement	51
3.2.4	Histology.....	51
3.2.5	Mineralization Associated Fluorescence Intensity Imaging	52
3.2.6	Immunohistochemistry	52
3.2.7	Atomic Force Microscopy	53
3.2.8	Second Harmonic Generation Imaging	54

3.2.9	LC-MS/MS Proteomics.....	54
3.2.10	Serum collection and analysis.....	55
3.2.11	Statistical analysis.....	56
3.3	Results.....	56
3.3.1	Deletion of pRb in murine aortic valve leaflets produces aortic valve regurgitation	56
3.3.2	Loss of pRb causes ECM remodeling and VIC activation.....	58
3.3.3	pRb cKO aortic valve leaflets show similar proliferation and apoptosis	59
3.3.4	pRb cKO valve leaflets have disordered matrix and increased stiffness	59
3.3.5	Loss of pRb in VICs results in structural changes in the ECM of aortic valve leaflets	60
3.3.6	Increased cytokine levels in aged pRb cKO mice	61
3.4	Discussion.....	61
3.4.1	Limitations to present study.....	65
3.5	Conclusion.....	66
3.6	Figures.....	67
Chapter 4.	Non-destructive two-photon excited fluorescence imaging identifies early nodules in calcific aortic-valve disease	79
4.1	Introduction	80
4.2	Methods.....	84

4.2.1	Human CAVD Valve Samples	85
4.2.2	Rat Valve Interstitial Cell (VIC) and Bone Isolation and Culture.....	85
4.2.3	Polyacrylamide (PAAM) Gel Preparation	86
4.2.4	Demineralization with EDTA.....	87
4.2.5	Alizarin Red Staining	88
4.2.6	Intensity correlation analysis between TPEF and Alizarin Red staining images	88
4.2.7	Scanning Electron Microscope Imaging	89
4.2.8	Micro-Structure Correlation Analysis between TPEF and SEM images	89
4.2.9	Fourier Transform Infrared (FT-IR) Spectroscopy	90
4.2.10	Two-Photon Excited Fluorescence Imaging	90
4.2.11	Image-Based Quantitative Assessment of Mineralization Associated Fluorescence (MAF)	92
4.2.12	MAF TPEF Intensity Analysis.....	93
4.2.13	Imaging of Genetic Mouse Model	94
4.2.14	Coherent Anti-Stokes Raman Scattering (CARS) Microscopy with TPEF Imaging	95
4.2.15	Time Lapse Imaging and MAF Quantification	96
4.2.16	Statistical Analysis	97
4.2.17	Data Availability.....	98
4.2.18	Code Availability	98

4.3	Results.....	98
4.3.1	Comparison of Imaging Techniques for Calcification.....	98
4.3.2	Spectral Analysis of Mineralized Tissue.....	99
4.3.3	Using a Ratiometric Approach to Enable Rapid MAF Imaging.....	103
4.3.4	CARS Imaging Confirms Hydroxyapatite Origins of MAF Signal.....	103
4.3.5	Applying the Ratiometric Method to ApoE ^{-/-} Mouse Model.....	104
4.3.6	Time Lapse Imaging Tracks Nodule Growth.....	105
4.4	Discussion.....	107
4.5	Conclusion.....	110
4.6	Figures.....	111
Chapter 5.	Using Large Scale Data Analytics to Direct <i>in vitro</i> 3D Model Experiments in CAVD	125
5.1	Introduction.....	126
5.2	Methods.....	129
5.2.1	RNA-Sequencing and Network Analysis of CAVD versus Normal Human Valves	129
5.2.2	Making Methacrylate Hyaluronic Acid.....	130
5.2.3	Porcine Cell Isolation and Culture.....	130
5.2.4	3D MeHA Gel Formation.....	131
5.2.5	Atomic Force Microscopy of MeHA Gels.....	133
5.2.6	Immunostaining and Single Fluorescence Imaging.....	133
5.2.7	Multiphoton Imaging of MeHa Gels.....	134

5.3	Results.....	134
5.3.1	Network Analysis of the Genes Identified Using RNA-Seq.....	134
5.3.2	Creation and Testing of MeHA Gels.....	135
5.4	Discussion.....	135
5.5	Conclusion.....	138
5.6	Tables and Figures.....	139
Chapter 6.	Conclusions and Future Directions.....	144
6.1	Conclusions.....	144
6.1.1	ECM Driven Treatment Possibilities of CAVD.....	144
6.1.2	Knockdown of pRb Leads to Valve Regurgitation – A Potential Model for CAVD	146
6.1.3	The Development of a Non-Destructive Imaging Approach to Better Visualize Mineralization.....	147
6.1.4	High Throughput Screening and Testing of ECM Proteins that Change in CAVD	149
6.2	Future Directions.....	150
6.2.1	Using Previous Findings and Imaging Techniques to Investigate the Role of pRb	150
6.2.2	How Collagen Crosslinking Can Influence CAVD.....	152
6.2.3	The Role of the Immune System in CAVD.....	155
6.3	Figures.....	158

Chapter 7. References..... 160

List of Tables

Table 2.1: Acrylamide and Bis Acrylamide Concentrations	18
Table 3.1: Hemodynamic evaluation and aortic root diameter of aged mice	57
Table 3.2: Evaluation of heart function, weight, and systemic blood pressure in aged mice	58
Table 5.1: Genes identified through network analysis for testing the MeHA gels ..	139

List of Figures

Figure 2.1: Initial assessment of VICs on PAAM gels.....	33
Figure 2.2: Nodule growth and VIC spread area are effected by the ECM binding protein.	34
Figure 2.3: The effect of siRNA knockdown of RHAMM on nodule growth.	35
Figure 2.4: The effect of siRNA knockdown of CD44 on nodule growth.	36
Figure 2.5: Protein expression analysis of osteogenic and apoptotic markers.	37
Figure 2.6: The relative RNA expression measured for CD44 siRNA knockdown VICs grown on 35 kPa HA PAAM gels.....	38
Figure 2.7: Experimental details and additional information.	39
Figure 2.8: Additional nodule measurement and growth data.	40
Figure 2.9: Knockdown of CD44 using a blocking antibody.	41
Figure 2.10: α SMA expression in CD44 and RHAMM knockdown VICs.	42
Figure 2.11: Images of western blots used for quantitative analysis of protein expression.....	43
Figure 2.12: The relative RNA expression was measured for CD44 siRNA knockdown VICs grown on 35 kPa collagen PAAM gels.	44
Figure 3.1: Tie2-driven loss of pRb causes aortic regurgitation (AR) with age.	67
Figure 3.2: Representative histology of aortic valve leaflets from aged mice demonstrates changes in pRb cKO aortic valve.	68
Figure 3.3: The calculated MAF of Rb het verse Rb cKO mice and representative images of each type of valve leaflet.....	69

Figure 3.4: Aged pRb cKO aortic valves do not have increased proliferation or apoptosis.....	70
Figure 3.5: Structural analysis of aortic valve leaflets reveals differences in stiffness and collagen organization between pRb het and cKO mice.	71
Figure 3.6: Analysis of the aortic valve proteome.	72
Figure 3.7: pRb loss in Tie2 lineage increases circulating cytokines in aged mice. ...	73
Figure 3.8: Survival of pRb het and cKO mice.	74
Figure 3.9: Histological analysis of aortic valve leaflet calcification in aged mice.....	75
Figure 3.10: Histological analysis of aortic valve leaflets from 2-month-old mice. ...	76
Figure 3.11: Differences in ECM protein components between pRb het and pRb cKO mice from proteomics analysis.	77
Figure 3.12: Splenomegaly and bone marrow alterations in pRb cKO mice.	78
Figure 4.1: Visual analysis of TPEF images compared to Alizarin Red staining of a human CAVD nodule, a rat bone, and a PAAM gel grown nodule.	111
Figure 4.2: Representative images of human CAVD nodules, rat bone samples, and PAAM gel nodules taken using SEM and TPEF.	112
Figure 4.3: Effect of EDTA treatment on endogenous TPEF.....	113
Figure 4.4: Analysis of TPEF emission spectra reveals emission spectrum of mineralization associated fluorescence.	114
Figure 4.5: MAF images enable enhanced visualization of mineralized sample regions.	115
Figure 4.6: MAF signal overlaps with CARS images.....	116
Figure 4.7: An ApoE ^{-/-} mouse model confirms the use of the MAF as a quantifiable metric for calcification.	117

Figure 4.8: Time lapse experiment of calcification on PAAM gels shows measured change in nodule size.	118
Figure 4.9: Correlating Alizarin Red images versus TPEF image and the PSD TPEF images versus the PSD of SEM images.	119
Figure 4.10: Representative series of images at different emission spectral bands using an 800 nm excitation.	120
Figure 4.11: Emission spectra acquired using 860 nm excitation and component analysis.	121
Figure 4.12: Representative TPEF and SHG images.	122
Figure 4.13: Additional, representative TPEF and SHG images.	123
Figure 4.14: Summary of the PAAM gel time lapse experiment with representative images.	124
Figure 5.1: Network analysis of ECM proteins identified by RNA-seq.	140
Figure 5.2: Development of a 3D MeHA gel system.	141
Figure 5.3: MeHA gel characteristics.	142
Figure 5.4: Optical measurements of MeHA gels.	143
Figure 6.1: The average nodule size of nodules grown by transfected pVICs in culture.	158
Figure 6.2: Schematic of known pathway links between molecules involved in mineralization.	159

Chapter 1. Introduction and Background

1.1.1 Introduction and Motivation

Calcific aortic valve disease (CAVD) is an active, degenerative process¹ in which fibrotic thickening of aortic valve tissue can lead to frank bone formation.² CAVD is the second-leading cause of cardiovascular disease, responsible for over 14,000 deaths in 2012.³ As valve disease progresses in an individual, and valve stenosis worsens, the only available treatment option available is full valve replacement surgery.⁴ While there has been significant advancement in the field of prosthetic valve development, even the best implantable valves need to be replaced every 10 to 15 years and while the ability to use transcatheterization has cut down on the need for open heart surgery, there are still many risks inherent to surgery.⁵ Given that the life expectancy of patients with severe, symptomatic aortic stenosis is under five years, there is a need for the development of alternative treatment methods. However, in order to develop pharmaceutical methods to treat CAVD, there must first be a better understanding of the disease mechanisms and progression.

The prevalence of valve replacement surgery has increased the availability of extracted, diseased leaflet tissue, aiding in the understanding of late-stage CAVD. This, along with genome-wide association and bioinformatics studies, has led to a robust understanding of the risk factors and end-stage characteristics of CAVD. The increased prevalence of CAVD in individuals with genetic defects that cause a bicuspid aortic valve anatomy, as opposed to the normal tri-leaflet anatomy,⁶ led to the initial theory that mechanical stresses were responsible for the initiation of CAVD.⁷ While it is now acknowledged that

mechanical forces could be involved in the disease progression, current efforts have focused on the cellular activation, inflammatory responses, and the possibility of a genetic component^{1,8} as the major factors involved in CAVD.

Efforts to further understand CAVD have been hindered by the lack of an animal model that truly recapitulates the disease and the inability to visualize early changes in human valve tissue. In fact, the use of hypolipidemic mouse models lead to a costly set of clinical trials that ended in disappointment when patients failed to respond to pathways identified in the genetic mouse models.⁹ In human patients, early changes in valve tissue are not detected since most aortic stenosis is only captured by echocardiography, late in disease progression.^{1,7} Despite these challenges, several risk factors for CAVD have been identified, including obesity, diabetes mellitus, smoking, chronic inflammation, and kidney disease.^{10,11} Additionally, cardiovascular disease, including CAVD, is more prevalent in men than women, with women presenting a better prognosis even after an aortic stenosis diagnosis.^{12,13} While the realization of these factors is important, a deeper understanding of the disease mechanisms is needed in order to direct pharmaceutical innovation. To be successful, this will require several of the following: the development of an animal model that better mimics CAVD in humans and/or the development of *in vitro* model systems to recapitulate the disease, better diagnostic techniques to describe earlier stages of the disease, the use of 'omics' data to describe both the cellular and extracellular processes and signaling, and the constant communication between physicians and researchers.

The efforts described in this thesis aim to both add to the existing body of knowledge on CAVD and to provide novel model systems and diagnostic imaging techniques to aid in

the understanding of disease progression. Several cell culture platforms, animal models, and human tissue samples were used to develop methods to specifically examine the interaction of extracellular matrix (ECM) properties and their effect on cell mineralization. Fluorescence imaging techniques that relied on either fluorescence dye or the endogenous fluorescence were also developed and helped to provide feedback on cell and valve mineralization. Together, these findings contribute to CAVD improved understanding and will enable further research into the inner workings of the disease.

1.1.2 Valve Anatomy and Normal Function

The first step in developing additional therapy methods to treat CAVD is a thorough understanding of normal valve anatomy and function. Typical aortic valve physiology consists of three valve leaflets each containing three layers,¹⁴ with the leaflets arranged in a semi-lunar geometry. The aortic side, termed the fibrosa, is composed primarily of circumferentially aligned collagen fibers. The ventricular side of the valve, the ventricularis, is a radially aligned, elastin rich layer that snaps the leaflet closed following systole, and the mid layer – the spongiosa – is a slippery, lubricating layer composed of proteoglycans.¹⁵ The three leaflets of the aortic valve open and close approximately three billion times in an average human lifespan,¹⁶ ensuring unidirectional flow from the left ventricle to the ascending aorta.

In normal developmental physiology, endocardial cushions form from the cardiac jelly between the atria and ventricles in the outflow tract of the developing heart. Rhythmic contractions, dependent on soluble factors from the myocardium, begin unilateral blood flow that force the endocardial cushion cells through endothelial-to-mesenchymal transformation (EndoMT). The mesenchymal cells then further settle into the aligned,

three-layer valve structure and remodel the ECM to a mature physiology.^{17,18} In humans and mice, this valve remodeling continues through early juvenile stages.¹⁹ In CAVD, there is a reactivation of the valve cell populations,²⁰ an increase in EndoMT,²¹ and renewed remodeling of the valve leaflets,²² showing some similarities to the valve development process.

1.1.3 Valve Cell Populations and Response to Disease

The average aortic valve leaflet is about 0.5 mm in thickness²³ and is covered by an endothelial layer of cells – valve endothelial cells (VECs). The resident cell population of the interior of the leaflets are called valve interstitial cells (VICs) and are now known to be a fairly heterogeneous cell population.²⁴ Both cell types are responsible for the lifetime maintenance and repair of valve tissue. Though typically quiescent, they are activated with injury or outside perturbation to the leaflets. Additionally, surface markers for both VECs and VICs are readily identifiable with endothelial cell markers CD31 and von Willebrand Factor (vWF) for VECs²⁵ and the fibroblast markers vimentin²⁶ and desmin²⁷ for quiescent VICs.

Endothelial cells throughout the body line blood-contacting surfaces and are subjected to a wide range of hemodynamic and mechanical forces. They retain the ability to rapidly respond to alterations in their environment by both changing their cell shape²⁸ and protein and gene expression.²⁹ In the valve, VECs play an important role in maintaining hemostasis by regulating tissue permeability, paracrine signaling, and the adhesion of inflammatory and progenitor cells. In response to injury, VECs go through EndoMT into an activated fibroblast state for valve repair.³⁰ Studies have also shown that VECs can

influence VICs, acting as an inhibitory mechanism, decreasing interstitial cell proliferation and regulating matrix production.³¹

In CAVD and sclerotic valve degeneration, VECs are activated and recruit inflammatory cells.³² The inflammatory cells secrete cytokines, such as transforming growth factor (TGF- β), which can induce EndoMT.³³ Transformed mesenchymal cells will then further activate into myofibroblasts which help with valve maintenance including remodeling and repair of the valve tissue. However, in diseased states, over-activation can lead to valve fibrosis and CAVD. Activated VECs also recruit macrophages and monocytes, increasing their migration into valve tissue.³⁴ In atherosclerosis, a disease that shares many similarities to CAVD,³⁵ calcification is associated with macrophage accumulation.³⁶ However, it is unlikely that VECs alone are responsible for CAVD, in fact, most studies have implicated VICs, the most common cell type in the valve, as the cell population most involved in valve fibrosis and mineralization.³⁷

Fibroblastic-like VICs remain in a quiescent state, responsible for the maintenance of leaflet ECM,³⁸ for the majority of a healthy patient's life. The cells are dispersed throughout the three layers of each leaflet, though studies in the responses of VICs from different regions of the valve show that this is a heterogeneous cell population.^{39,40} Typical VIC morphology is a flattened cell lacking a basement membrane with the ability to synthesize both ECM producing and ECM degrading proteins. For valve repair, VICs become activated to myofibroblasts, expressing smooth muscle alpha-actin (α SMA),⁴¹ and increasing ECM production⁴² to maintain the valve's structural integrity. VICs are also able to differentiate into several different cell types including the activated myofibroblast, progenitor cells, and osteoblast-like cells.³⁷ The maintained differentiated state of these

VICs can lead to fibrosis and CAVD in the valve when increased ECM production creates valve tissue that is thicker and stiffer than the normal leaflet.⁴³

The expression of α SMA in myofibroblast VICs is a hallmark of CAVD.⁴⁴ While myofibroblasts are an initial part of the wound healing response - migrating to the wound location and producing enzymes and matrix proteins necessary for wound healing⁴⁵ - excessive remodeling can cause matrix disorganization and fibrosis.⁴⁶ In an unfortunate feedback loop, as the valve leaflet and cellular environment stiffen, there is an increase in myofibroblast activation, leading to more matrix remodeling.⁴⁷ These activated cells can further transform into osteogenic cells that deposit calcification and further CAVD progression.⁴⁸ The mechanism for the conversion from normal myofibroblasts to disease is still unknown, but there have been studies implicating several proteins and signaling pathways including bone morphogenetic proteins (BMPs),⁴⁹ cadherin-11,⁵⁰ TGF- β ,⁵¹ and the NOTCH1 pathway.⁵² The complexity of these interactions is also compounded by the changes to valve leaflet composition, especially with age,⁵³ suggesting that along with VICs and VECs, the aortic valve ECM may play a role in CAVD.

Finally, there is currently a debate in the field of CAVD cellular response surrounding the cells specifically involved in valve calcification. One school of thought is that VICs and VECs differentiate into osteogenic cells that begin the mineralization process in the valves, and the other, is that circulating osteogenic precursor (COP) cells land on the valve leaflets and begin the mineralization. The latter argument stems from a paper by Egan et al. where the researchers found COP cells in human CAVD valves only around mineralized portions of the tissue and not in the unaffected portions of the leaflets.⁵⁴ The opposing view that VICs and/or VECs take on an osteoblast bone-like phenotype is the basis for

many *in vitro* experiments since VICs especially have been shown to readily calcify especially in osteogenic media or in the presence of TG F- β .⁵⁵ Although most cell types, given the right *in vitro* conditions will calcify, in this thesis I am arguing that most valve mineralization is the result myofibroblast activation and VIC osteogenic differentiation though both cells types are likely to play a role. The bases for this argument is that VICs have been shown to be able differentiate into a number of different cell phenotypes, each that could play a role in valve calcification and there have been a wide variety of studies that show that VICs can calcify under many conditions, but *in vitro* and *in vivo*, indicating there could be many ways that VICs are involved in mineralization.

1.1.4 Extracellular Matrix in the Valve

As previously mentioned, the aortic valve leaflets have a tri-layer structure. The three layers each have different ECM compositions, each serving a specific function. Besides providing mechanical support, the ECM can absorb and sequester different biochemical molecules and release them as needed, directly impacting VIC and VEC behavior.⁵⁶ ECM is a dynamic structure that is constantly being remodeled and valve cells can interact with ECM both directly, through integrin binding, and indirectly, through soluble factors making valve ECM an important player in leaflet health. Gross changes in valve ECM composition occur rapidly during valve development and then stagnate for much of a patient's adult life.⁵⁷ However, slow changes in overall valve ECM do occur with age, including protein migration to different regions of the valve,⁵⁸ and overall ECM composition. For example, glycosaminoglycan (GAG) - found primarily in the spongiosa layer - concentrations are shifted with age to include a higher percentage of the GAG

hyaluronic acid (HA) and a lower percentage of glucuronate.⁵³ These ECM changes could be an important factor in CAVD development.

From studying end-stage CAVD valves, removed from patients during valve replacement surgery, a clear description of fully diseased leaflet ECM can be made. Mild CAVD is characterized by a fibrotic thickening of the leaflets,⁵⁹ typically through an increase in proteoglycan and collagen content. This thickening and change in ECM composition is also accompanied by a loss in the normal collagen architecture⁶⁰ and a pathological stiffening of the cellular mechanical microenvironment.⁶¹ Many of these ECM changes are caused by overactive VICs³⁷ that fail to undergo the normal apoptosis following repair,⁶² leading to a diseased aortic valve.

With good reason, collagen I is perhaps the most studied ECM protein in CAVD. Nearly all calcific nodules begin in the collagen-rich fibrosis, which experiences both strong mechanical forces and turbulent hemodynamic forces.⁶³ However, recent studies have also implicated the adjacent, GAG-rich spongiosa as a source of other ECM components that could play an important role in CAVD.^{64,65} Notably, HA has been shown to localize around calcific nodules in the valve⁶⁵ and the use of prolonged addition of HA as a treatment method to human corneas has been linked to increases in calcification,⁶⁶ suggesting a link between HA and mineralization. Overall, a more in-depth understanding of the changes to the ECM during CAVD, and the impact these changes have on valve cells, is needed in order to better characterize valve disease.

1.1.5 Current Models of CAVD

Aortic stenosis is typically diagnosed by echocardiography⁷ when the patient expresses signs and symptoms associated with heart failure such as fatigue, shortness of breath, or swelling in the lower extremities. Unfortunately, an echocardiogram is most effective at diagnosing CAVD only during advanced stages of the disease.¹⁵ This presents two challenges for physicians and researchers: 1) the ability to only study patients who already have advanced aortic stenosis instead of being able to learn more about the early stages of the disease, and 2) perhaps missing the opportunity to treat the disease more effectively by catching it early in its development. To overcome these challenges, there has been the development of both animal models and *in vitro* systems to mimic the progression of CAVD in humans and advancement in imaging techniques that can pick up calcific nodules much earlier in their development.⁶⁷

To date, many mouse models for CAVD have been created, with many of them drawing on the idea that high levels of lipids in the blood play a key role in CAVD. While many models require the mice be fed a high-fat or “Western” diet in order to induce calcification, some are either genetically engineered to have hypercholesterolemia or attempt calcification through a different mechanism.⁶⁸ While there has been some success in recapitulating parts of the disease, such as in the Apolipoprotein E knockout mouse which develops calcific lesions that stain positive for osteogenic markers like ALP, Runx2, and osteocalcin,³⁶ there are many limitations to using mouse models. Perhaps most notable are the many failed human trials that used statins as a possible treatment regimen based on the results of mouse model studies.⁹ In addition to mice, rabbit and swine models have been used. While rabbits are not naturally susceptible to CAVD, similar

to mouse models, valve stenosis can be induced with a Western diet. Porcine valves can naturally develop calcifications and have the added advantage of having the same anatomical structure as human valves. However, pig models are expensive and generally slow to develop the disease even with a high-fat diet. In order to reduce costs and have more control over the model design, many researchers have turned to *in vitro* model systems to study CAVD.

Model systems of CAVD have been developed in both 2D⁶⁹ and 3D⁷⁰ and can use either VICs or a combination of VICs and VECs to mimic the disease. In 2D culture, VIC activation with TGF- β has been shown to be dose dependent⁶⁹ and substrate stiffness can also activate cells, similar to in human CAVD valves.⁴⁷ Three dimensional models are also used to accurately recapitulate the natural 3D environment of VICs to study myofibroblast differentiation into diseased, osteoblast-like cells in the valve⁷⁰ and have even been used as platforms to test drug therapies.⁷¹ While 2D models are more simplistic than 3D models, they have been shown to create consistent calcifications and can be used as a way to decrease variability in studying CAVD mechanisms.⁷² Consistent and measurable systems are necessary to the development of pharmaceutical treatments and *in vitro* models can provide a platform for this study. Additionally, mechanical insights found in *in vitro* systems can also help with the development of new animal model systems that may better mimic CAVD.

1.1.6 The Use of Imaging Modalities to Study CAVD

Along with the challenge of creating model systems to understand the beginning stages of CAVD is a lack of assessment tools that non-destructively identify changes in the valve tissue. In the past, histological sectioning was the only method of assessing the finer

details of valve biology and the changes associated with CAVD. Bone, similar to the calcifications found in end-stage CAVD, is notoriously difficult to slice, making sectioning a less accurate method of assessing mineralization. Staining for mineralization can also be confounded, especially in mouse models where the presence of small black, non-calcified particles can be confused for nodules labeled with the black calcification stain von Kossa.⁷³ The development of non-destructive imaging methods has greatly improved understanding of CAVD. Along with echocardiography, current non-destructive imaging modalities used to study and diagnose CAVD include computed tomography (CT),⁷⁴ ultrasound,⁷⁵ magnetic resonance imaging (MRI),⁷⁶ molecular imaging with fluorochromes,⁷⁷ and second harmonic generation (SHG) imaging.⁷⁸⁻⁸⁰

While still widely used, echocardiograms and MRI are limited by their spatial resolution (about 0.5 mm),^{77,81,82} but other imaging methods, such as CT, have been developed to improve the visualization of micron-sized nodules that have been shown to exist in human aortic valves.⁸³ Electron beam CT imaging uses dual-scan contrast agents⁸⁴ to provide high resolution images (0.24-0.33 mm for bone in humans⁸²) that can be taken in both humans and animals, such as mice. With the use of radioisotopes like ¹⁸F sodium fluoride (NaF),⁸⁵ actively calcifying cells – which uptake ¹⁸F NaF – can be identified earlier in the disease processes and then confirmed later using CT.⁸⁶ Unfortunately, these modalities still carry the risk of radiation exposure,⁸⁷ but there are other methods that are still in the process of being fully moved into the clinic that could mitigate this issue. Molecular imaging leverages near-infrared light and exogenous chromophores^{77,88} to provide increased image resolution. It has been used to measure inflammation and bone formation *in vivo* and could be applied to CAVD.⁸⁹ Lastly, SHG, a two-photon scattering process that uses the non-centrosymmetric geometry of collagen fibers to visualize the collagen

architecture in valve leaflets has already been used *ex vivo* to assess changes during CAVD⁶⁰ and could be further developed to investigate molecular level changes *in vivo* through the use of fiber optics. Overall, the further development of existing and novel imaging techniques can help provide early insights to the changes that occur in CAVD and may provide clues to a mechanism to stop the progression of valve stenosis.

1.2 Conclusion

A better understanding of CAVD will help both with creation of mitigating techniques at the onset of the disease as well as with the development of preventative measures that will improve quality of life and reduce cost of care. While significant progress has been made in the comprehension of CAVD, including the paradigm shift of treating valve disease as an active, degenerative disease as opposed to a passive, “senile” disease of the elderly, there is still much to learn. This is evident by the lack of any non-surgical, treatment method for CAVD that even slows the progression of the disease. While great strides have been made in developing systems and techniques to study valve stenosis, there are challenges facing a broader understanding of the disease. This thesis aims to provide both a potential mechanism of calcification and an addition to the body of knowledge surrounding ECM changes in CAVD, as well as the addition of a two-photon excited fluorescence imaging technique that uses endogenous fluorescence to capture micron-sized, calcific nodules.

Chapter 2. CD44 Signaling Modulates Valve Interstitial Cell Calcification in Vitro

This chapter is based on work that, at the writing of this thesis, is currently under review for publication. For this chapter, I was involved in the conception and design of the experiments, collection and assembly of data, data analysis and interpretation, manuscript writing, and the final approval of manuscript. Dr. Phil Hinds and Dr. Gordon Huggins contributed to the data interpretation and final approval of the manuscript and contributed financially along with Dr. Lauren Black (NIH – NHLBI Award # R01HL114794). In addition to funding, Dr. Black contributed to the project conception and design, manuscript writing, data interpretation, and final approval of manuscript.

Abstract

The lack of pharmaceutical targets available to treat patients with calcific aortic valve disease (CAVD) necessitates further research into the specific mechanisms of the disease. In this study, we investigate the effect of two extracellular matrix (ECM) components, collagen and hyaluronic acid (HA), on the mineralization of valve interstitial cells (VICs) within the context of a 2D, polyacrylamide model system. Using a novel, non-destructive imaging technique, we were able to track calcific nodule development in culture systems over a three week time frame. We saw a significant increase in the size of the nodules grown on HA PAAM gels as compared to collagen PAAM gels suggesting that HA has a direct effect on mineralization. Directly looking at the two known receptors of HA - CD44 and receptor for HA-mediated motility (RHAMM) – and using siRNA knockdown revealed that a decrease in CD44 expression resulted in a reduction of calcification, leading to a potential new target for CAVD treatment.

2.1 Introduction

Calcific aortic valve disease (CAVD) currently affects over 8 million people in the US.⁹⁰ Several risk factors for CAVD have been identified including smoking, hypertension, hyperlipidemia, and advanced age. Currently more than 48% of CAVD patients are diagnosed with mild to severe calcification, but detecting early stage CAVD can be difficult. Ultimately, the only successful method of treatment is full aortic valve replacement surgery.⁹¹ A more thorough and complete understanding of the earliest states of CAVD, including disease origin and mechanisms contributing to progression, would help advance progress towards less invasive, and potentially more effective,

treatment methods. Hallmarks of advanced CAVD, such as extracellular matrix (ECM) changes, cell activation, and changes in valve mechanics⁹² have been studied in an attempt to identify drug targets, but, to date, there are no FDA approved drugs that slow, halt, or reverse CAVD.

Changes to the aortic valve leaflet structure and composition can be observed throughout the progression of CAVD via histology. Calcific nodules begin in the leaflet layer closest to aorta, called the fibrosa, while advanced nodules can penetrate the trilayer valve anatomy. Disease progression is also marked by an increase in glycosaminoglycans (GAGs) and collagen I content that contribute to an overall fibrotic thickening of the valve leaflet structure.²² Many of these changes are attributed to the activation of a resident cell population called valve interstitial cells (VICs). Phenotypically normal VICs are responsible for the maintenance of valvular ECM homeostasis, and are generally quiescent cells.³⁸ In CAVD, as much as 30% of the total VIC population becomes activated to the myofibroblast phenotype which is characterized by an increase in ECM secretion and VIC proliferation, leading to thicker, fibrotic tissue and a stiffening cellular environment.⁴³ A stiffer cellular environment has been shown to lead to further increases in activation of myofibroblasts⁴⁷ resulting in a positive feedback loop that can drive disease progression. However, while many of these changes have been primarily identified in the context of late-stage CAVD, where stenosis is already present, it is unclear what role the properties of the extracellular matrix play in the initiation of the activation of VICs and the development of calcification.

Changes in ECM composition can also be attributed to changes in VIC behavior.⁵⁷ Hyaluronic acid (HA) has previously been shown to be the largest single contributor of GAG content in heart valves, comprising about 35% of total GAGs in the aortic valves.⁵³

HA content has also been shown to increase with age⁵⁷ which correlates with increased prevalence of CAVD in elderly patients. VIC-HA interactions have been studied previously, demonstrating a significant influence of HA on *in vitro* mineralization.⁶⁴ While it is known that HA receptors can be mechanosensitive,⁹³ there are seemingly contradictory results that show an increase in HA concentration surrounding calcific nodules⁶⁵ and HA playing a role in hindering⁹⁴ mineralization. Additionally, while polyacrylamide (PAAM), 2D cell culture systems have been used to look at mineralization in VICs,^{95,96} the use of these systems has generally been constrained to using collagen only to mimic the ECM and have not been used to study other ECM proteins. The effects of individual ECM proteins, such as HA, on VIC activation and disease states may help define specific pathways that lead to mineralization, and *in vitro* model systems allow for direct control over ECM concentration and cell interaction.

In addition to its high abundance in the valve, HA, and its two cell receptors, CD44 and receptor for HA-mediated motility (RHAMM),⁹⁷ have been studied in the context of atherosclerosis^{98,99}, which has features similar to CAVD.¹⁰⁰ However, there has been little research into how these receptors could affect the mineralization of valve cells or their specific influence on the VIC phenotype. In this manuscript, we used physiologically relevant tissue stiffnesses to mimic both healthy and diseased valve tissue while also using HA as an ECM binding component. Using non-lethal calcium fluorescence labeling, we were able to track nodule growth over a three week culture period and, by selectively inhibiting CD44 or RHAMM, we were able to demonstrate the specific role and mechanosensitivity of these receptors in the context of valve mineralization.

2.2 Methods

2.2.1 Substrate Preparation

Before the creation of PAAM gels, 9 mm x 9 mm glass cover slips were activated to create binding sites for the PAAM as previously described.¹⁰¹ To increase hydrophilicity, cover slips were passed through an open flame and then covered with 0.1M NaOH. After the slips dried, 3-aminopropyltrimethoxy was smeared onto the cover slips and allowed to dry. Slips were then placed into 24-well plates and washed three times in diH₂O using an orbital shaker before 0.5% glutaraldehyde was smeared onto the slips and allowed to set for 30 minutes. After aspirating off the glutaraldehyde, the slips were again washed in diH₂O for three five-minute washes. Activated cover slips were stored in diH₂O at 4°C until use.

PAAM gels were created at three distinct moduli (5 kPa, 20 kPa, and 35 kPa) to create non-activating, transitional, and activating^{47,102} VIC environments by varying the amount of cross-linking between acrylamide and bis acrylamide. Gel stiffness was confirmed using atomic force microscopy (AFM). A total of 200 µg of protein (a combination of either Collagen I and HA) was cross linked to the varying stiffness gels using acrylated N-hydroxysuccinimide (NHS; Sigma-Aldrich, St. Louis, MO [A8060-1G]) ester to create covalent linkages between amine groups. **Table 2.1** provides information on acrylamide and bis acrylamide amounts. 1 N HCl was added to the solution to lower the pH to 6.8-6.9 and acrylamide to bis acrylamide cross-linking was initiated using tetramethylethylenediamine (TEMED; Sigma-Aldrich, St. Louis, MO [411019]) and 10% ammonium persulfate (APS; Sigma-Aldrich, St. Louis, MO [A3678]).

Table 2.1: Acrylamide and Bis Acrylamide Concentrations

Stiffness	Acrylamide ($\mu\text{L}/\text{ml}$)	Bis Acrylamide ($\mu\text{L}/\text{mL}$)
5 kPa Gels	250	17.5
20 kPa Gels	250	22.5
35 kPa Gels	250	50

Activated cover slips were dried in a sterile cell culture hood and 80 μL of each gel solution was placed onto the cover slips. A non-activating cover slip was then placed directly onto the gel solution to reduce airflow and promote polymerization while creating an even gel surface. After 30-45 minutes, the top cover slip was removed from the polymerized gels using a razor blade. The gels were moved to sterile 6-well plates and washed three times for 5 minutes each with sterile 1X PBS.

2.2.2 Cell Culture

VICs were isolated from rat leaflets following surgical removal of the leaflets.¹⁰³ Using standard medium [Dulbecco's Modified Eagle's Medium (DMEM; ThermoFisher Scientific, Waltham, MA [10566016]), 1% Fungizone (ThermoFisher Scientific, Waltham, MA, Antibiotic-Antimycotic [15240062]), and 10% fetal bovine serum (FBS, ThermoFisher Scientific, Waltham, MA [16000-044])], tissue samples were explanted for 1 week at 37°C with 5% CO₂. Following removal of the tissue, VICs from 3 separate isolations were mixed and used at passages 4-6 for experimentation. Cells were seeded on PAAM gels at 12,000 cells/cm². After seeding, seeded gels were dosed for 24 hours with 1.25 ng/mL transforming growth factor beta-1 (TGF- β_1 ; Peprotech, Rocky Hill, NJ [100-21]) diluted in 2% bovine serum albumin (Sigma Aldrich) before being replaced with normal VIC media.

2.2.3 Nodule Characterization

To image calcium nodules in culture, the fluorescent indicator fluo-4 acetoxymethyl (AM; ThermoFisher Scientific, Waltham, MA [F14217]) was used. Fluo-4 AM, a dye typically used for Ca⁺ transient studies,¹⁰⁴ was excited at 488 nm, using a microscope [Olympus MVX10 microscope using cellSens Dimension software (version 1.8.1, Olympus Corporation)]. The PAAM gels were prepared by first removing the culture medium and replacing it with a DMEM solution containing 10 μ L/mL of Fluo-4 AM. The gels were then placed in the incubator for 20 minutes wrapped in aluminum foil to prevent light contamination and to allow the fluo-4 AM to bind to calcium in the culture. The fluo-4 AM solution was then removed and replaced with normal VIC media.

After an additional 4 hours in the incubator, to allow the cells to exocytose the dye from their cytosol,¹⁰⁵ the entire gels were imaged in the Tyrode's solution containing 140 NaCl, 5 KCl, 5 HEPES, 1 NaH₂PO₄, 1 MgCl₂, 1.8 CaCl₂ and 10 glucose (pH 7.4) adjusted with NaOH. All salts and buffers were purchased from ThermoFisher Scientific. Upon imaging completion, the gels were placed in culture medium and continued in culture. Over the 3 week culture period, the gels were imaged at 7, 14, and 21 days.

The images were analyzed using ImageJ¹⁰⁶ (NIH, Bethesda, MD) to determine calcium nodule number and area. A macro program was designed so that for each image, a threshold was set to create a mask for only nodule fluorescence. After the mask was applied, the area of the gel in each image was used to measure the number of positive pixels in the image and converted to an area using a calibrated conversion factor.

Using the masked image, a custom MATLAB script was used to find the average least squares distance between each nodule and its neighbors. The distances between each nodule on a single PAAM gel were then averaged to obtain the average distance between nodules for each condition. This was done for week 1, 2, and 3.

2.2.4 CD44 Blocking with Antibody

VICs were passaged from tissue culture plastic flasks and kept in a 15 mL conical with 1 μ g/mL of an anti-CD44 blocking antibody [KM81] (Abcam, Cambridge, MA [ab112178]) for 45 minutes before seeding onto the PAAM gels. The treated VICs on the PAAM gel were cultured as previously described, including dosing for 24 hours with TGF- β_1 . For the duration of the experiments, media changes were supplemented with the same concentration of the anti-CD44 blocking antibody. Cells were collected for western blot analysis 2 and 6 days after cell seeding and nodule growth experiments were imaged after 1, 2, and 3 weeks in culture.

2.2.5 Immunohistochemistry

To measure cell spread area, following three weeks in culture, PAAM gels were fixed using 4% paraformaldehyde (PFA; Sigma-Aldrich, St. Louis, MO [158127]) for 10 minutes. PAAM gels were then washed with 1X PBS 3 times, for 5 minutes. A 5% donkey serum in 2% BSA (Sigma-Aldrich, St. Louis, MO [A9418]) solution was used to block the gels for at least an hour at room temperature. A concentration of 20 μ l/mL of Alexa Fluor 488 Phalloidin (ThermoFisher Scientific, Waltham, MA [A9418]) in 2% BSA was used to image the VICs on the PAAM gels and a custom CellProfiler¹⁰⁷ pipeline was used to measure cell spread

area. To measure smooth muscle alpha-actin (α SMA; Santa Cruz Biotechnology, Dallas, TX [sc-32251]) intensity, cells were plated onto PAAM gels, dosed with TGF- β_1 , and fixed 48 hours post seeding. Intensity was measured using a separate CellProfiler pipeline. To measure α SMA intensity as well as to count positively expressing RHAMM (Abcam, Cambridge, MA [ab157107]) and CD44 (Developmental Studies Hybridoma Bank, Iowa City, IA [H4C4]), VICs were seeded onto the PAAM gels and then transfected with siRNA. 24 hours following the transfection, the cells were dosed with TGF- β_1 , and then fixed for 10 minutes with 4% PFA 48 hours after dosing. The protocol for blocking described above was used, however, after blocking, the PAAM gels were then placed in primary antibody (either α SMA or RHAMM or CD44) at a 1:200 concentration in 2% BSA for 1 hour. Following 3 washes in 1X PBS, a 1:400 concentration of secondary antibody (ThermoFisher, Waltham, MA) in 2% BSA was used for 1 hour. Samples were imaged following 3 more washes in 1X PBS. Positive cell counts were calculated using a third CellProfiler pipeline.

2.2.6 Transfection with siRNA

VICs were seeded on PAAM gels and allowed to adhere overnight in a 37°C incubator. VICs were then transfected with either CD44 (HCAM) siRNA, RHAMM siRNA, or a scramble Control siRNA-A (all purchased from Santa Cruz Biotechnology, Inc., Dallas, TX; product numbers [sc-35534], [sc-40182], [sc-37007], respectively) using the Santa Cruz Biotechnology, Inc. protocol. Following transfection, the siRNA VICs were treated with 1.25 ng/mL TGF- β_1 for 24 hours. The transfection procedure was then repeated at day 15 to ensure RNA silencing for the entirety of the 3 week experiment as outlined in Supp.

Figure 1 A. Calcific nodule images, using Fluo-4 AM were taken, at day 7, day14, and day 21. siRNA knockdown was confirmed using Western Blot analysis.

2.2.7 Western Blotting

Based on the results of a BCA protein assay, lanes of a 15% gradient gels (Biorad, Hercules, CA [456-1083]) were loaded with equal amounts of protein (typically between 5 and 15 μ g) collected from VICs transfected with either siRNA for RHAAM or CD44 or a scrambled control. After samples were mixed with dithiothreitol, which served as a sample buffer, solutions were heated at 95°C for 5 minutes. Before loading, sample tubes were mixed vigorously with a vortex before being centrifuged. Western gels were run for 35 minutes at a constant 100V. Then protein was transferred to a nitrocellulose membrane using a maximum current of 400mA for 3 hours. Blots were blocked in a solution of 5% milk in TBST (Tris buffered saline and 10% Tween 20) and stained with the following antibodies: CD44 (Abcam, Cambridge, MA; anti-CD44 antibody [157107]), RHAMM (Santa Cruz, Dallas, TX; RHAMM antibody [sc-16170]), runx2 (Abcam; anti-runx2 antibody [ab23981]), osteopontin (Abcam; anti-osteopontin antibody [ab8448]), cleaved PARP (Abcam; anti-cleaved PARP antibody [ab32064]), caspase 3 (Abcam; anti-caspase 3 antibody [ab13847]). Blots were incubated with primary at a 1:200 concentration overnight at 4°C and then rinsed 3 times for 5 minute with TBST. Secondary HRP-conjugated antibodies (ThermoFisher Scientific, Waltham, MA [656120] and [656520]) were incubated for at least one hour at room temperature using a concentration of 1:400. Following three, 5 minute rinses in TBST, blots were developed with enhanced chemiluminescence reagents on G:Box Chemi XR5 (Syngene, Cambridge, UK). Antibody expression was normalized using cellular β -actin expression (primary 1:1000; Sigma-Aldrich; [A5316] and secondary

1:5000; Jackson ImmunoResearch, West Grove, PA; [715-035-150]). Blot band intensities were quantified with ImageJ software (NIH, Bethesda, MD) (n=6 for each condition). The same procedure was used for analyzing protein collected from the CD44 siRNA knockdown VICs on the 35kPa HA and collagen PAAM gel at days 2 and 21.

2.2.8 Quantitative PCR

Quantitative polymer chain reactions (qPCR) was done on VICs grown on PAAM gels using either HA or collagen as the binding protein and transfected with either HCAM siRNA or a control siRNA. RNA was collected on day 2 and on day 21 of the experiment and used to produce cDNA for qPCR. The following Taqman primers (ThermoFisher Scientific, Waltham, MA) were used to measure RNA content in the samples: Runx2 [Rn01512298_m1], Parp1 [Rn00565018_m1], Casp3 [Rn00563902_m1], CD44 [Rn00681157_m1], Hmnr [Rn00564204_m1], acta2 [Rn01759928_g1], TGFB1 [Rn00572010_m1], Gapdh [Rn01775763_g1], SPP1 [Rn00681031_m1]. Real-time PCR reactions, with an n of three with duplicate technical replicates for each group, were done on a Stratagene Mx3000p thermocycler.

2.2.9 Statistics

All results were analyzed by first checking for normality (Shapiro-Wilk) and equal variance (Brown-Forsythe) tests with post hoc Tukey HSD testing when appropriate. When comparing two independent data sets (such as protein expression via Western blot), a two-tailed, unpaired student t-test was used. For data sets failing the normality test, an ANOVA on the ranks was used followed by a Dunn's post-hoc analysis. Two-way or three-way ANOVAs were used for multiple comparisons and are noted in the figure legends.

2.3 Results

2.3.1 Nodules grown on HA gels grew significantly larger nodules than those on Collagen

Rat VICs were seeded onto PAAM gels containing either collagen or HA as the ECM binding protein. PAAM gels had a stiffness of either 5kPa, to simulate a healthy leaflet stiffness, 35 kPa to mimic a CAVD diseased state, or 20kPa stiffness to simulate transitional disease tissue.^{47,102} VICs were stained with smooth muscle alpha-actin (α SMA) to look for VIC activation to myofibroblasts; representative histological images are shown in **Figure 2.1 A**. It should be noted that all samples were activated for 24 hours by dosing with TGF- β_1 , so the α SMA expression is a combined effect of chemical and environmental signals. Myofibroblast activation, as measured by α SMA expression, demonstrated a significant decrease for cells grown on PAAM gels with increasing stiffness, from 20kPa to 35kPa, on the HA gels, and increase in expression on HA gels as compared to the collagen in the 35 kPa conditions. (**Figure 2.1 B**). Cell density was also measured with DAPI staining and showed that there were no significant difference in cell numbers (**Figure 2.1 C**).

Experiments looking for changes in VIC phenotype and calcification were then conducted over a three week period. Calcific nodules found on the PAAM gels were stained with both Alizarin Red and fluo-4 (**Figure 2.8 A**) to confirm the presence of mineralization. Fluo-4 images were then used to analyze nodule growth data over a 3 week culture period (representative images can be found in **Figure 2.4 E** and **Figure 2.7 B**). VICs on both collagen and HA PAAM gels of all stiffnesses grew calcific nodules over the 3 week culture period; however, while collagen PAAM gels produced larger nodules in the first week of

culture, by the third week in culture, HA PAAM gels, especially the 35 kPa gels, had significantly larger nodules than the collagen gels. (**Figure 2.2 B**).

2.3.2 ECM binding protein determines cell spreading

Since our imaging technique using Fluo-4 staining was non-destructive, we could compare nodule growth on the same PAAM gels over the entire experiment. To determine if nodule clustering could play a role in the increased nodule size on HA PAAM gels, the average distance between nodules was determined for each gel. While no statistical differences were observed over the three-week culture period, HA PAAM gels did show a trend toward decreasing average distance between nodules at two weeks and then an increase in the average distance between nodules at three weeks; this trend was not seen in collagen gels (**Figure 2.8 B and C**). This could be a function of a rapid period of mostly random mineralization followed by a merging of smaller particles into one, larger particle. However, there was no difference in the average number of nodules grown in any of the conditions (**Figure 2.8 D**). By measuring the growth rate of nodules on PAAM gels over time, we also see a decrease in the growth rate after the initial growing phase, but then an increase in growth rate, possibly due to nodules merging, after two weeks that is significantly pronounced on the HA PAAM gels for all stiffness groups (**Figure 2.2 C**). Cell spread area, after three weeks, was also assessed using phalloidin to stain VIC F-actin (**Figure 2.2 D**). As shown in **Figure 2.2 E**, the measured cell spread area was significantly larger for VICs grown on HA PAAM gels compared to collagen gels for all stiffnesses. This correlates with previous findings demonstrating that a cell's measured traction force increases with cell spread area¹⁰⁸ and that an increase in cell area leads to stiffer cells.¹⁰⁹

2.3.3 siRNA knockdown of CD44 decreases mineralization

As a first attempt to explore the link between ECM protein composition and mineralization, we blocked a known HA cell-binding protein, CD44,¹¹⁰ with a known CD44 blocking antibody (KM81). Since our previous experiments showed the greatest degree of nodule growth occurred on the 35 kPa stiffness PAAM gels and this stiffness most closely mimics the environment VICs sense during CAVD, we chose to do the remainder of the experiments using only 35 kPa PAAM gels with either HA or collagen as the binding protein. Western blot analysis showed a trend towards decreased CD44 abundance at 2 and 6 days following treatment; the blocking antibody did not significantly impact VIC CD44 expression (**Figure 2.9 A**). Since KM81 only blocked existing CD44 and did not alter CD44 expression within the cell itself, this result is not surprising. Additionally, VICs cultured on PAAM gels for 3 weeks with continuous addition of the CD44 antibody did not show any change in mineralization using either HA (**Figure 2.9 B**) or collagen (**Figure 2.9 C**) as the binding ECM protein.

We then used siRNA transfection to knockdown CD44 and RHAMM – another HA binding protein⁹⁷ that does not have an established blocking antibody – to test their role on calcification. To ensure knockdown of the proteins over the entire experiment, siRNA transfection was performed twice; once immediately following cell seeding and a second time halfway through the experiment (see **Figure 2.7 A**). Western blot analysis demonstrated that siRNA knockdown of CD44 and RHAMM was successful (**Figure 2.3 A**, **4A**, and **Figure 2.11 A**). The presence of CD44 did have a significant effect on nodule size with siRNA knockdown of CD44 leading to smaller nodules on HA PAAM gels, but having no effect on nodules grown on collagen gels (**Figure 2.4 B**). By comparison, RHAMM

knockdown had no significant impact on nodule size (**Figure 2.3 B**). VICs on HA gels did have a significantly larger cell spread area in the control case as compared to collagen (similar to **Figure 2.2 D**) and trended towards a larger area in the siRNA knockdown conditions (**Figure 2.3 C**). There were no differences seen in cell number on the PAAMs gels in any condition (**Figure 2.3 D**). There was a significant increase in cell spread area of the CD44 knockdown VICs compared to the scramble control on the HA PAAM gels.

2.3.4 Knockdown of RHAMM leads to increase in apoptotic markers while CD44 Knockdown shows an increase in osteogenic markers

To determine if either RHAMM or CD44 had an effect on α SMA expression, IHC was used to quantify expression intensity. Similar to the α SMA expression in **Figure 2.1 B**, there was not a significant difference in measured percentage of cells that expressed α SMA between ECM types in the control scramble siRNA; however, there were differences in cell activation in both the CD44 and RHAMM siRNA knockdown PAAM gels (**Figure 2.10 A and B**). On collagen PAAM gels, there was a significant increase in VIC activation with both the CD44 and RHAAM siRNA knockdown cells and on the HA gels. siRNA RHAMM cells showed a trend of less α SMA expression than the CD44 siRNA knockdown VICs. Since these results seemed to contradict our hypothesis of increased VIC activation leading to increased calcification, we next analyzed both protein and RNA expression in the shRNA knockdown VICs.

To assess how VIC protein expression changed with the knockdown of either CD44 or RHAMM, protein taken from cells grown on tissue culture plastic (TCP) from both phase I and phase III of the experiment was analyzed using western blotting. VICs with RHAMM

siRNA knockdown did not show any differences in protein expression compared to the scramble control (**Figure 2.5 A**). Notably, both the scramble and the RHAMM siRNA protein showed a significant increase in PARP, an apoptotic marker, from phase I to phase III. Conversely, knockdown of CD44 demonstrated an upregulation of the osteogenic factors runx2 and osteopontin early in the experiment, but this increase was lost at the later time point (**Figure 2.5 B**). Interestingly, while the scramble siRNA showed a similar trend in increasing PARP expression with time, the CD44 siRNA, while not significant, showed a decreasing trend. Example blot images for all Western data can be found in **Figure 2.11 B and C**.

The lack of any significant differences in either actual mineralization or protein expression with the RHAMM siRNA knockdown allowed us to focus on the CD44 siRNA knockdown. As the mineralization effect was greatest on 35 kPa PAAM gels, we also exclusively utilized these substrates. To assess the difference in gene expression in the CD44 siRNA knockdown VICs, RNA was collected at two days after treatment with TGF- β_1 and at the end of the experiment (21 days). Quantitative PCR (qPCR) was done to look for CD44 and RHAMM expression as well as for osteogenic markers (Runx2 and OPN), apoptotic markers (Casp3 and PARP) and VIC activation markers (α SMA and TGF- β_1) in the CD44 knockdown VICs. Knockdown VICs grown on 35 kPa HA gels showed an increase in OPN, TGF- β_1 , and α SMA at the day 2 time point (**Figure 2.6**). Also of note is the relative expression of CD44 is unchanged from the scramble case. Since the siRNA works to cleave the targeted mRNA, it is reasonable to expect that the mRNA expression of CD44 continues as the siRNA works to reduce it, but the targeted mRNA may not be translated, as we see a significant decrease in CD44 protein expression via Western blot (**Figure 2.4 A and Figure 2.11 A**).

2.4 Discussion

While some progress has been made in elucidating how CAVD initially develops, there have been no conclusive determinations of mechanisms leading to ineffectual pharmaceutical trials and a lack of non-surgical options available for patients. To ameliorate this issue, we developed a simple *in vitro* model system based on PAAM gels to elucidate the effects of the ECM environment on the development and growth of mineralized nodules. This system allows for fine control of stiffness and ECM binding sites, allowing us to study specific details of VIC mediated calcific nodule growth. Using TGF- β_1 mediated VIC activation to initiate nodule growth, we determined that CD44- ECM interactions play a role in calcific nodule growth.

VICs seeded on either healthy, transitional, or diseased stiffness PAAM gels grew calcific nodules over the course of the three week experiments regardless of the binding protein. However, while initial growth rates were consistent during the first week of the experiment, there were interesting discrepancies at later time points. By week three, nodules grown on HA gels, at all stiffnesses, had a faster growth rate than on their respective collagen gels. This growth rate pattern of a slower rate after rapid, initial growth during the first week has also been shown in other calcification models, such as in vascular calcification grown in a monolayer.¹¹¹ Since the VICs are only activated with TGF- β_1 once, for 24 hours, at the onset of the experiment, the initial mineralization may be induced by the cytokine; however, later in the experiment, environmental factors likely become more important in nodule development. Knockdown of the HA cell receptors RHAMM and CD44 showed marked differences in VIC mineralization and protein expression over three weeks. While siRNA knockdown of CD44 decreased overall

mineralization on the PAAM gels, RHAMM knockdown did not significantly alter mineralization or protein expression. These data suggest that ECM-to-cell signaling, through CD44, may play a role in exacerbating valve tissue calcification and could be a target for pharmaceutical intervention.

Quantitative PCR of RNA taken from CD44 knockdown VICs show differences in the relative expression of markers of VIC activation (TGF- β_1 and α SMA) and the osteogenic marker OPN which may provide insight into CD44's role in the mineralization pathway. In the CD44 knockdown VICs, there was an initial increase (at the 2 day time point) in OPN expression over the control case. OPN $-/-$ mice show normal bone formation¹¹² and OPN has been shown to decrease mineralization *in vitro*,¹¹³ which may explain the decreased mineralization measured in the CD44 knockouts. Additionally, there is some evidence that suggests that the knockdown of CD44 actually increases OPN expression. This has been shown, indirectly, with increases in OPN mediated HIF-2 α in cells treated with a blocking anti-CD44 antibody¹¹⁴ and in an increase in both OPN and CD44 even without an increase in HA content. OPN has also been shown to activate fibroblasts in lung tissue,¹¹⁵ which could explain the increase in α SMA and TGF- β_1 expression seen in the qPCR measurements. TGF- β_1 has also been shown to decrease mineralization *in vitro* when collagen gels seeded with osteoblasts were treated with the cytokine¹¹⁶, and TGF- β_1 is known to be mediated by HA through CD44.¹¹⁷ Furthermore, CD44 has also been shown to prevent apoptosis¹¹⁸ which could explain the increasing trend in PARP and Casp3 expression with the knockdown of CD44. However, the relationship between OPN, CD44, TGF- β_1 , and even HA, remains unclear¹¹⁹ and additional research is needed to fully understand this mechanism.

While HA, and even CD44 specific, signaling has been studied in the context of cardiovascular disease, such as atherosclerosis,⁹⁹ and diseased human aortic valves showed an increase in HA immediately surrounding the nodules¹²⁰ there has yet to be a defined mechanism for HA's role in mineralization. It has previously been suggested that glycosaminoglycans, proteoglycans, and HA could contribute to CAVD by retaining water and lipids which attract inflammatory cells and cause calcification via a pathway similar to atherosclerosis.¹²¹ However, our system, lacking in both lipids and monocytes, suggests that HA signaling alone may be enough to promote calcification by OPN downregulation through CD44 signaling. While upregulation of OPN may be a difficult target for therapeutic treatment due to its importance throughout the body¹²² and with previous evidence pointing to high levels of OPN associating with cancer,¹²³ targeting CD44, which has been done with histone deacetylase inhibitors, is a possible alternative.¹²⁴

While we believe that our 2D *in vitro* model system is sufficient to study potential CAVD mechanisms, all model systems inherently contain limitations. 2D culture systems do not fully explain cellular behavior in 3D, *in vivo* tissues and so future studies will investigate 3D culture systems that still segregate ECM components, but that allow for movement between layers to examine VIC movement between and interaction with multiple ECM components. Additionally, we will focus on more potential mechanisms that include CD44 induced pathway. Valve tissue also contains a second type of cell along the tissue edge, valve endothelial cells (VECs), which may also play a role in valve calcification through EMT.¹²⁵ These factors will also need to be explored in future studies to determine if CD44 has as strong of an effect on nodule calcification with these confounding factors; however, it is important to also understand the behaviors of cells in a model system in order to parse out potential mechanisms. To further study the role of CD44 on CAVD, a

CD44 null mouse model could be used. A previous study combined a typical mouse model for cardiovascular disease, an apolipoprotein E knockout, with CD44^{-/-} mice and found that CD44 is an early regulator for atherosclerosis;¹²⁶ however, to the best of our knowledge, this model has never been used to study CAVD. This model for valve disease may provide additional information that our 2D model system is lacking.

2.5 Conclusion

In conclusion, HA, through a CD44 mediated pathway, is a potential pharmaceutical target to slow the progression of CAVD in patients with existing calcification. CD44 was shown to be a driver of calcification of VICs on HA coated PAAM gels, with HA gels developing much larger nodules at a much faster growth rate as compared to nodules formed on collagen PAAM gels. A potential mechanism for the CD44-HA role in calcification is through OPN, which was shown to be upregulated with siRNA knockdown of CD44. While further study is needed to fully elucidate the role of CD44 in CAVD, the results from this study suggest that HA could play a prominent role in CAVD progression.

2.6 Figures

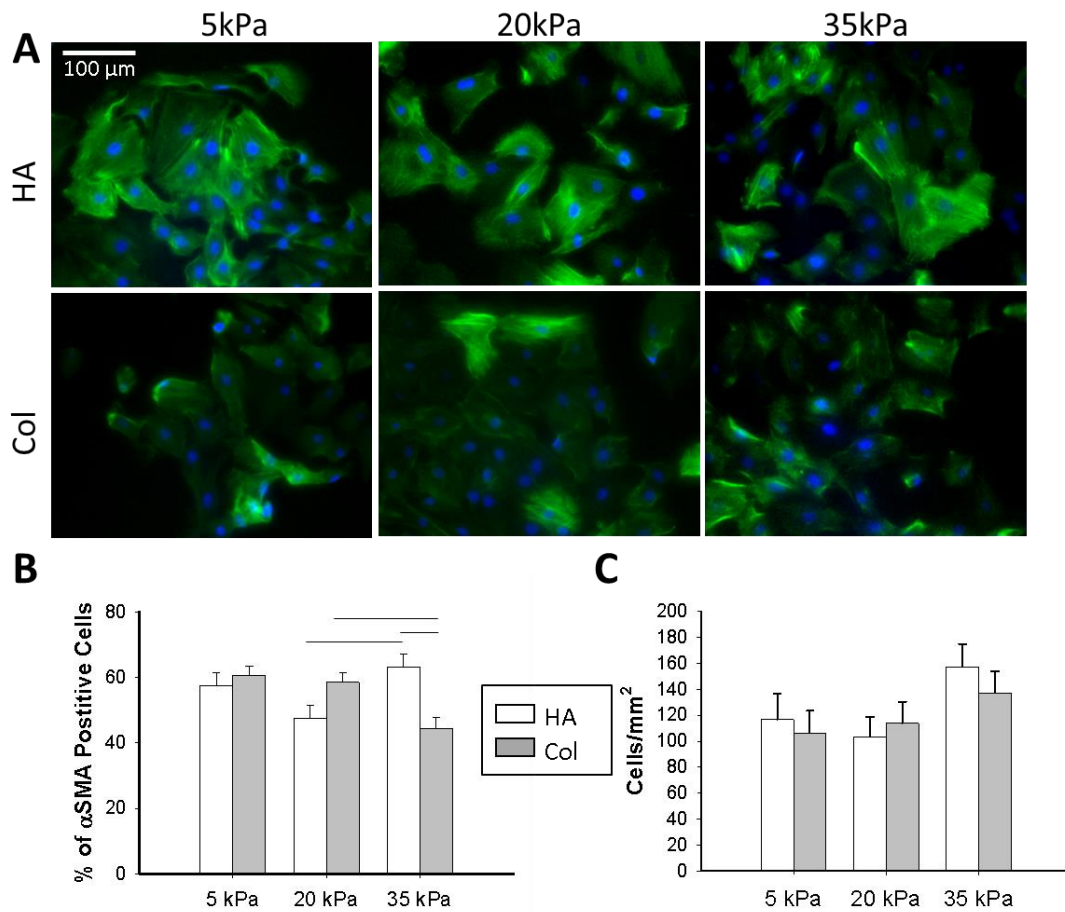


Figure 2.1: Initial assessment of VICs on PAAM gels.

VICs grown on 5 kPa, 20 kPa, and 35kPa PAAM gels with either HA or collagen as the binding protein were allowed to adhere to the gels for 24 hours before being dosed with TGF- β 1 for 24 hours. VICs were stained for α SMA (A) and the average expression was measured (B). This data set failed the normality and equal variance test so statistical analysis was done using a rank test with a Dunn's post-hoc test. After activation, the VICs showed a decrease in α SMA expression on the 35 kPa collagen gels, but an increase in α SMA expression on 35 kPa HA gels. There were no significant differences in cell density between proteins or on different stiffnesses (C). $p < 0.05$

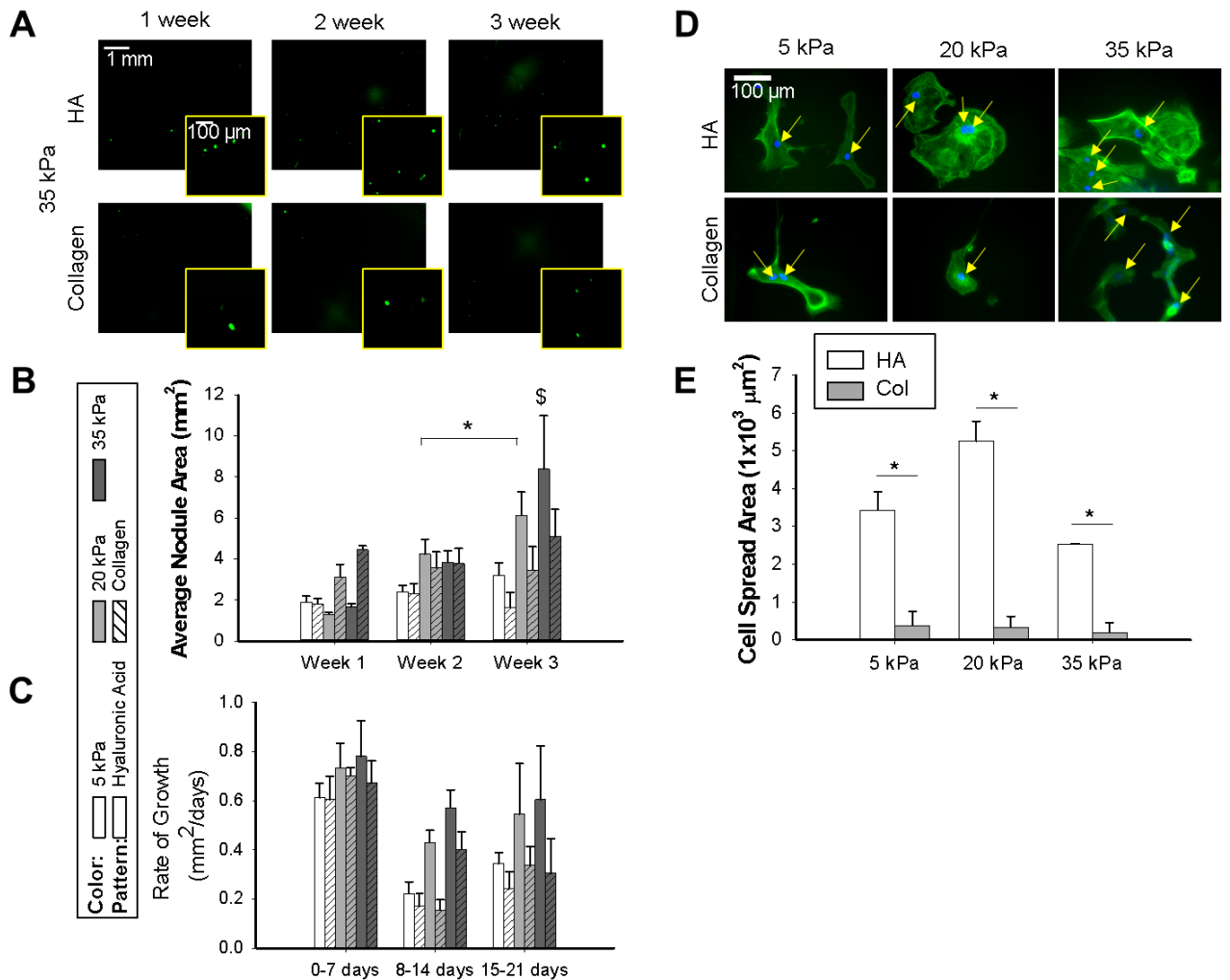


Figure 2.2: Nodule growth and VIC spread area are effected by the ECM binding protein.

Flou-4 AM was used to non-destructively measure the nodule growth over time and representative images are shown in (A). Average nodule size was measured for calcific nodules grown on 5 kPa, 20 kPa, and 35 kPa PAAM gels with either HA or collagen as the ECM protein (B). A three-way ANOVA showed a significant nodule growth with time ($p=0.006$). PAAM gel images were also used to calculate the average distance between nodules (C) in each condition. The rate of growth of the nodules on each of the PAAM gels types for the different protein was also measured. A three-way ANOVA shows that both the ECM protein ($p=0.011$), stiffness ($p=0.017$), and the time point ($p<0.001$) have a significant effect on nodule growth rate. (D) Phalloidin (green) was used to calculate the cell spread area for VICs seeded onto PAAM gels with 5 kPa, 20 kPa, and 35 kPa Young's Moduli using either HA or collagen. (E) As measured by a rank test with Dunn's post-hoc testing, there was a significant increase in the cell spread area of those VICs seeded on HA gels at all stiffness levels. $*p<0.05$

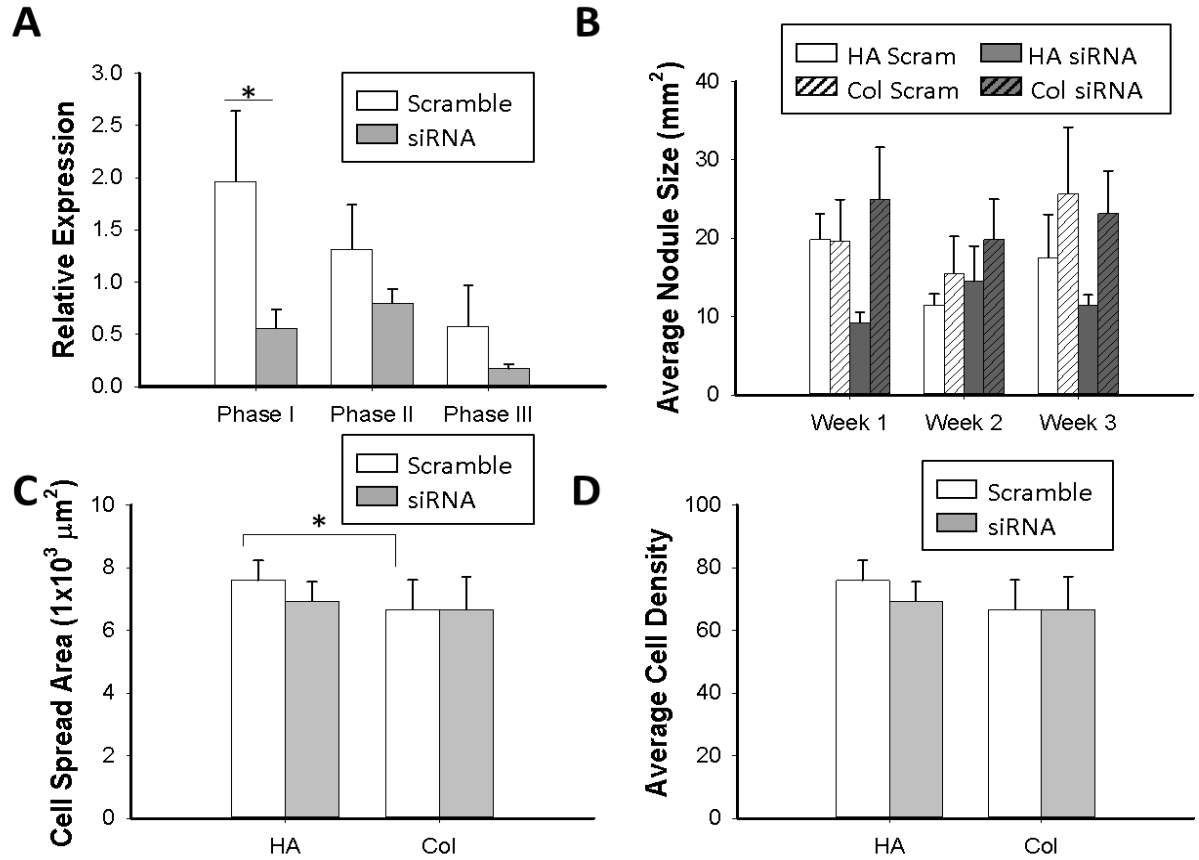


Figure 2.3: The effect of siRNA knockdown of RHAMM on nodule growth.

(A) Western blot analysis shows that RHAMM was knocked-down during the experiment using a two-tailed student t-test for each experimental phase. Nodules grown in the PAAM gel system with RHAMM siRNA for gels with HA and collagen (B). A three-way ANOVA found a significant increase in overall nodule size over time ($p=0.031$), but no effect of siRNA on nodule size. The average cell spread area (C) and cell density (D) for the different PAAM gel conditions were also calculated. A two-way ANOVA of the cell spread area revealed a significant interaction between the knockdown and the binding protein ($p=0.014$) whereas no statistical significance was measured in cell density. * $p<0.05$

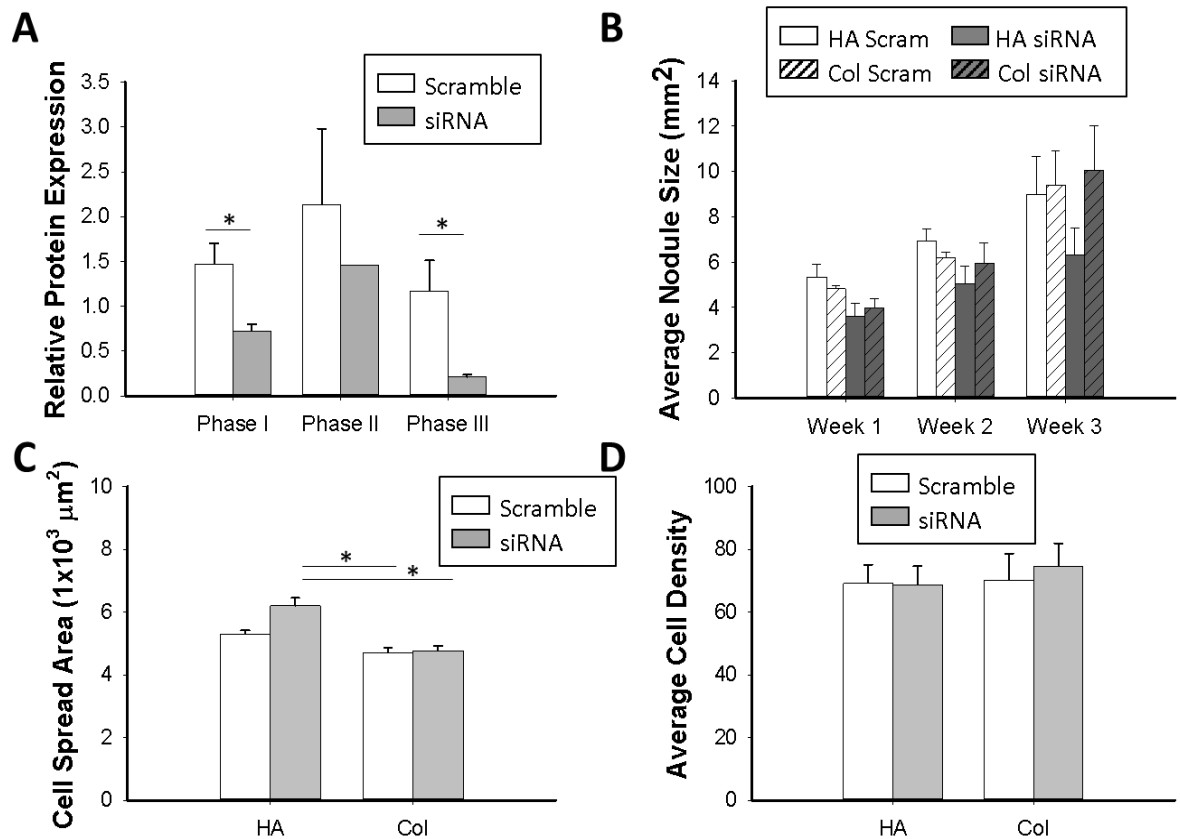


Figure 2.4: The effect of siRNA knockdown of CD44 on nodule growth.

Western blot shows that CD44 was successfully knocked down (A) using a two-tailed student t-test for each experimental phase. siRNA knock down of CD44 significantly reduced ($p=0.031$) the average nodule size for nodules grown on HA PAAM gels while also, overall, growing with time ($p=0.034$) as shown by a two-way ANOVA (B). The collagen nodule data did not have a normal distribution, but a rank test shows the nodules grow with time, but are not affected by the CD44 knockdown. There is also a significant increase in cell spread area of VICs in CD44 siRNA knockdown VICs on HA gels compared to VICs grown on the collagen gels as measured by a rank test since the data set was not a normal distribution (C). There is no significant difference in cell density in the model system (D). * $p<0.05$.

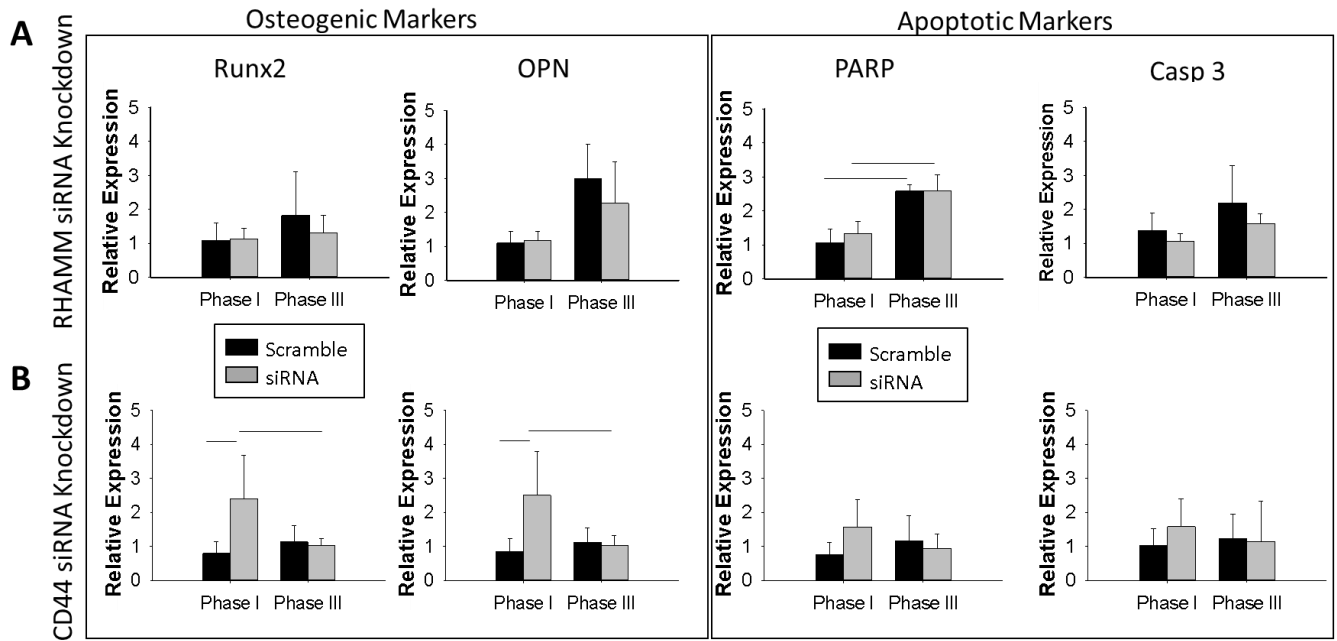


Figure 2.5: Protein expression analysis of osteogenic and apoptotic markers.

Western blot analysis was done on VICs transfected with either RHAMM siRNA (A) or CD44 siRNA (B) and grown on tissue culture plastic for three weeks. Two time points were assessed: at the phase I and phase III of the experiment. The relative expression of two osteogenic markers (Runx 2 and OPN) and two apoptotic markers (PARP and Casp3) were measured. A two-way ANOVA on the RHAMM siRNA VICs shows an increase over time for both OPN ($p=0.033$) and PARP ($p<0.001$). A two-way ANOVA for the CD44 siRNA knockdown VICs shows a significant impact of the siRNA in both Runx2 ($p=0.033$) and OPN ($p=0.03$). Tukey test post-hoc analysis also shows differences in both (A) and (B) where $*p<0.05$.

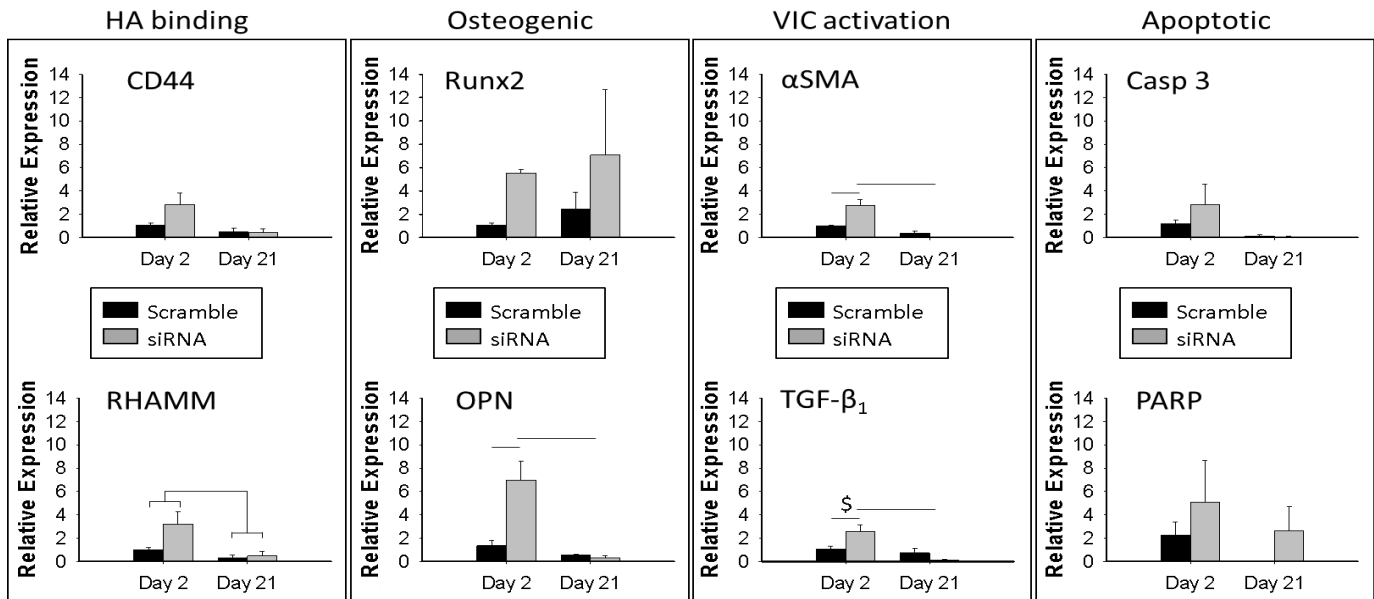


Figure 2.6: The relative RNA expression measured for CD44 siRNA knockdown VICs grown on 35 kPa HA PAAM gels.

The relative RNA expression is normalized to the scrambled siRNA samples at day 2. There were also no significant changes seen in the expression of CD44, the osteogenic marker Runx2 or the apoptotic markers Casp3 and PARP. There were significant changes in the RNA expression of RHAMM with a two-way ANOVA showing an effect of time ($p=0.039$). A two-way ANOVA for the RNA expression of the osteogenic marker, OPN, showed an effect of time ($p=0.008$) and siRNA ($p=0.035$). Additionally, a two-way ANOVA showed that time also had an effect on the expression of the activation markers TGF- β_1 ($p=0.02$) and α SMA ($p=0.002$). Tukey post-hoc testing results are shown with lines over the bar graphs and have a $p<0.05$ except for where the \$ denotes that $p=0.063$.

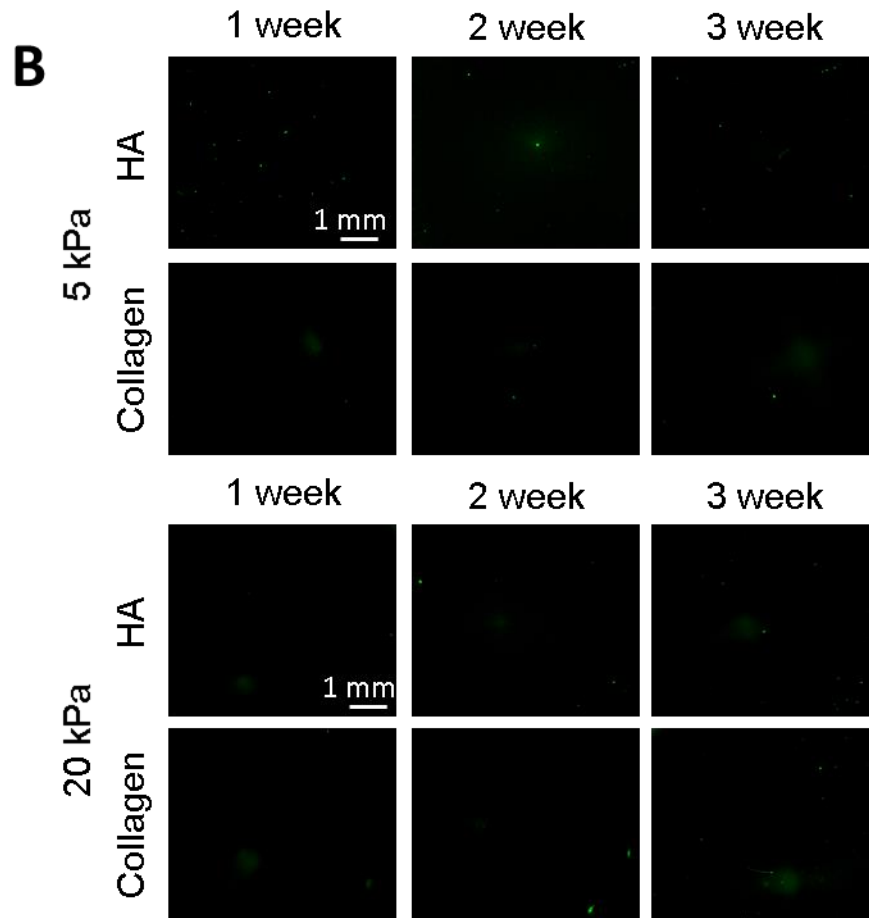
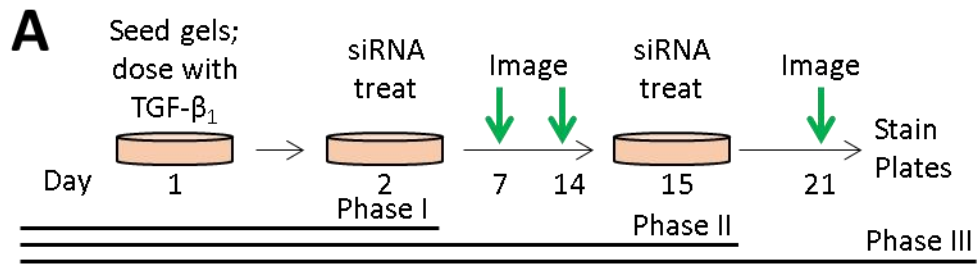


Figure 2.7: Experimental details and additional information.

(A) A schematic of the experimental timeline showing when TGF- β_1 dosing, transfection, and imaging were performed. (B) Representative images of the nodules stained with fluo-4 AM during the first two weeks of the experiment.

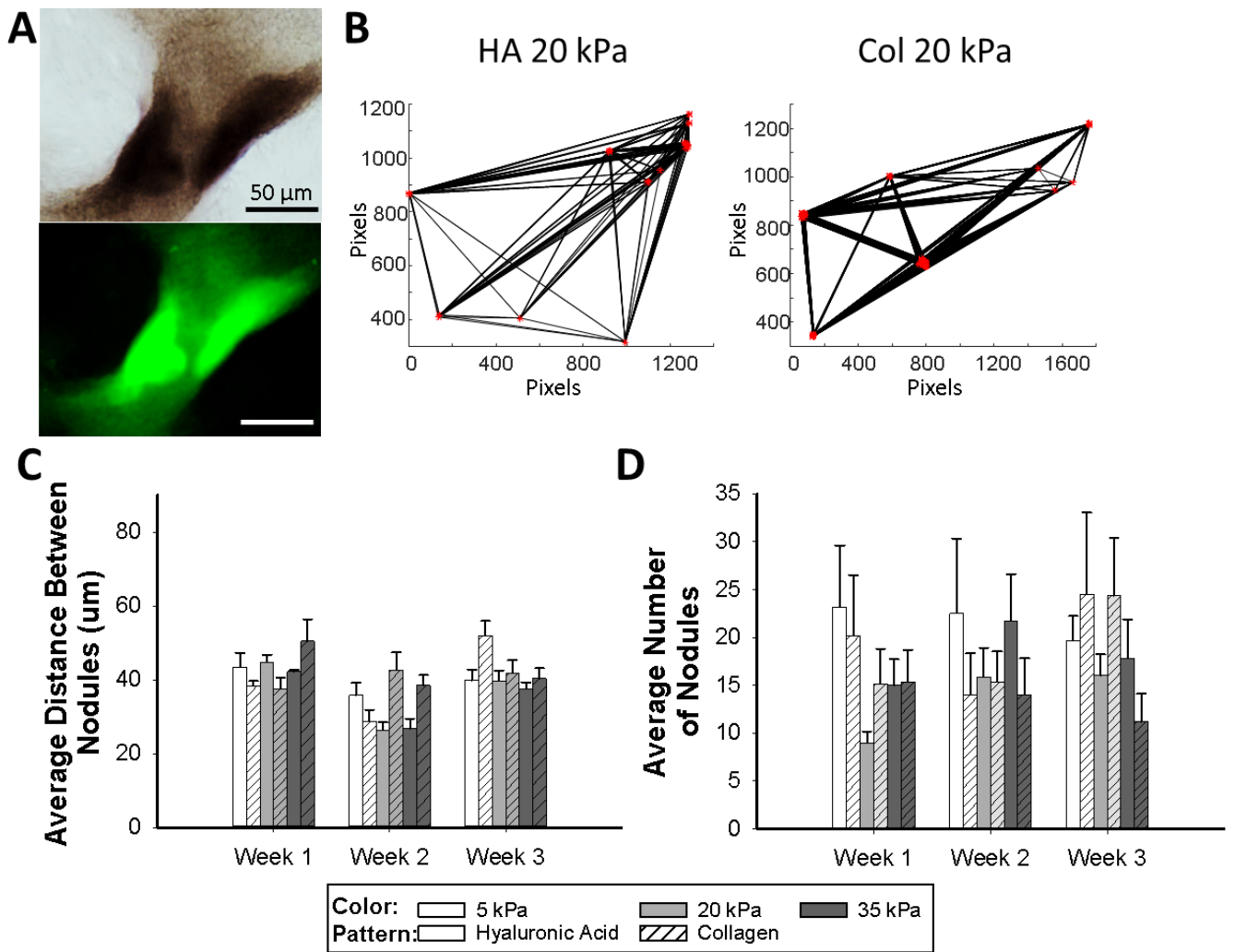


Figure 2.8: Additional nodule measurement and growth data.

(A) Representative images of a calcified nodule stained with Alizarin red (top) and the fluorescence calcium indicator dye fluo-4 am (bottom). (B) Representative plots showing nodules (red dots) and their proximity to other nodules that was used to calculate the average distance between nodules in (C). There was not statistical difference shown in the average distance between the nodules or in the average number of nodules (D).

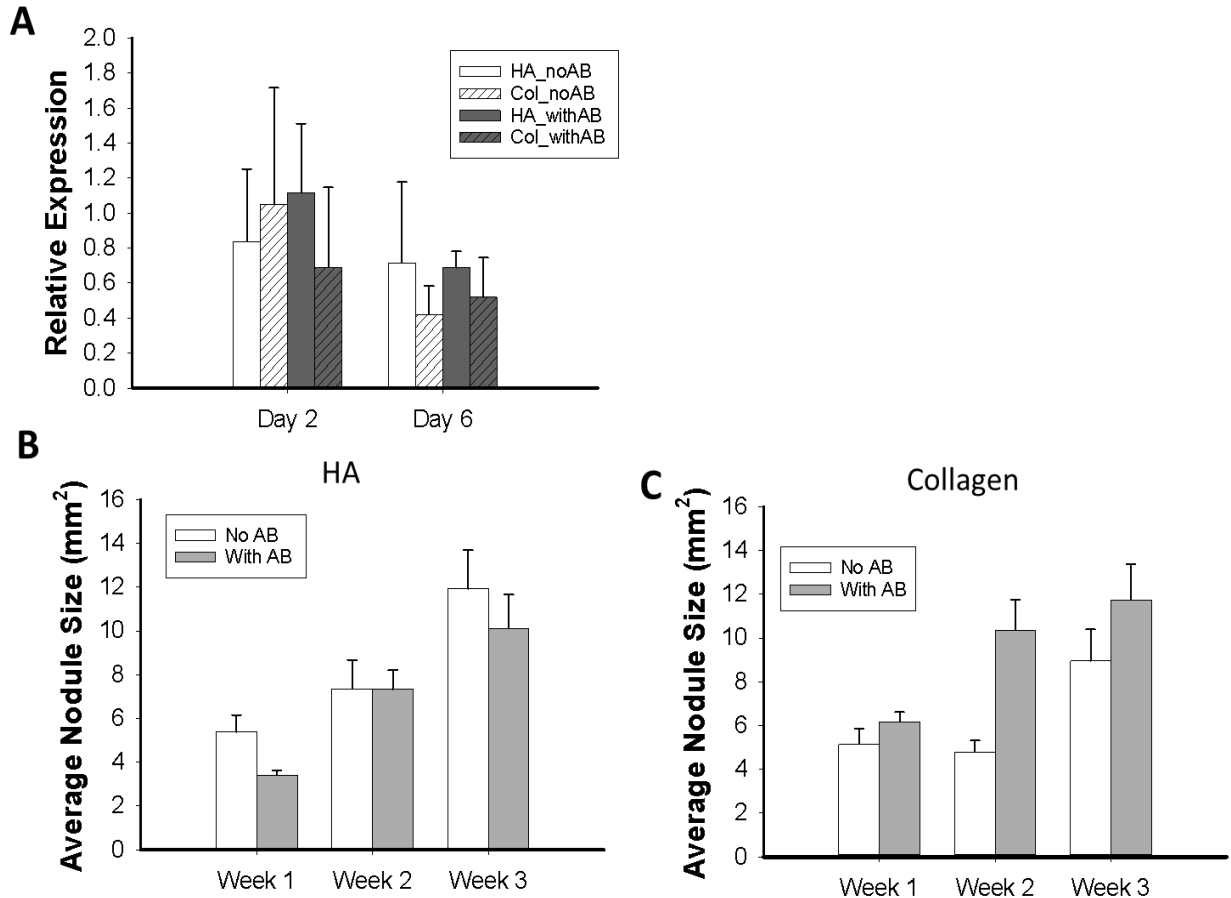


Figure 2.9: Knockdown of CD44 using a blocking antibody.

Knockdown of CD44 using a KM81 antibody showed some decreasing trends in expression via Western blot analysis (A), but not a significant decrease. The antibody also did not have an effect on nodule size over 3 weeks for either HA (B) or collagen (C).

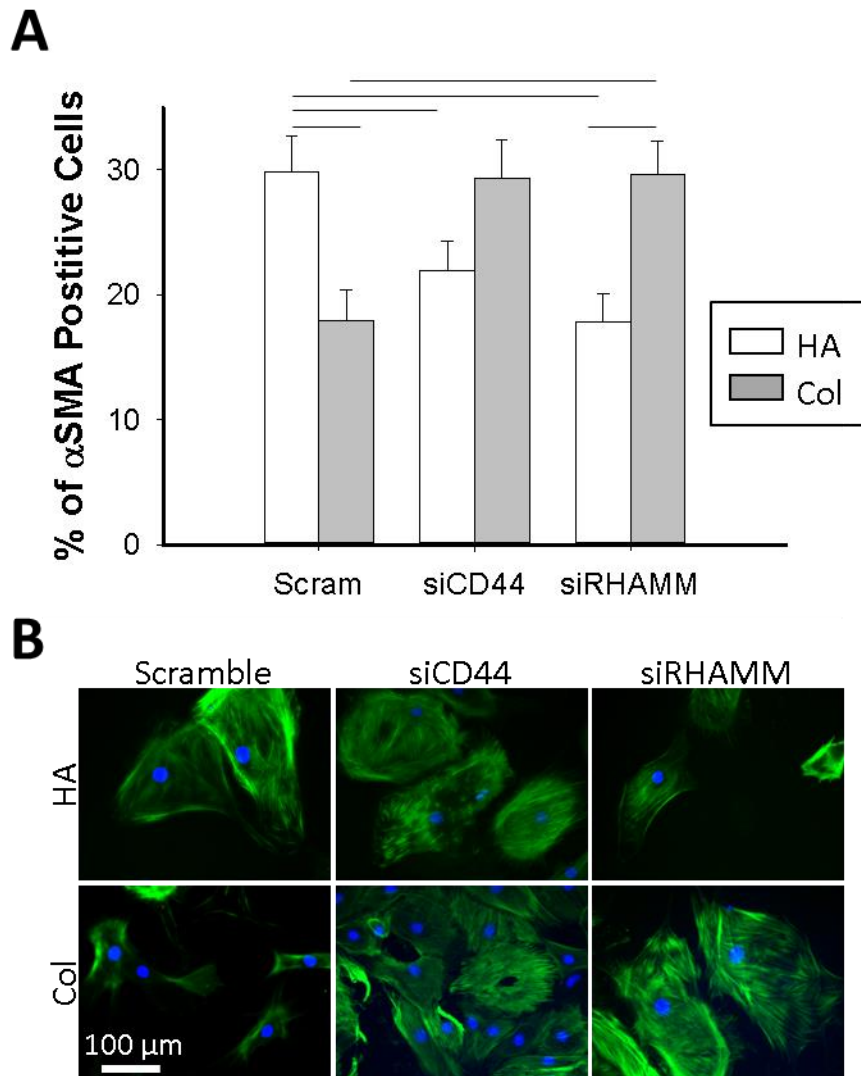


Figure 2.10: α SMA expression in CD44 and RHAMM knockdown VICs.

The average intensity of α SMA expression for cells with either a CD44 or RHAMM siRNA knockdown compared to the scramble controls after 48 hours in culture (A). The data set failed the Shapiro-Wilk normality test so an ANOVA on the ranks shows a similar trend in the scramble cases as seen in Figure 1 while the siRNA knockdown VICs show more α SMA on HA gels and less on the collagen gels. Representative images are shown in (B). $p < 0.05$

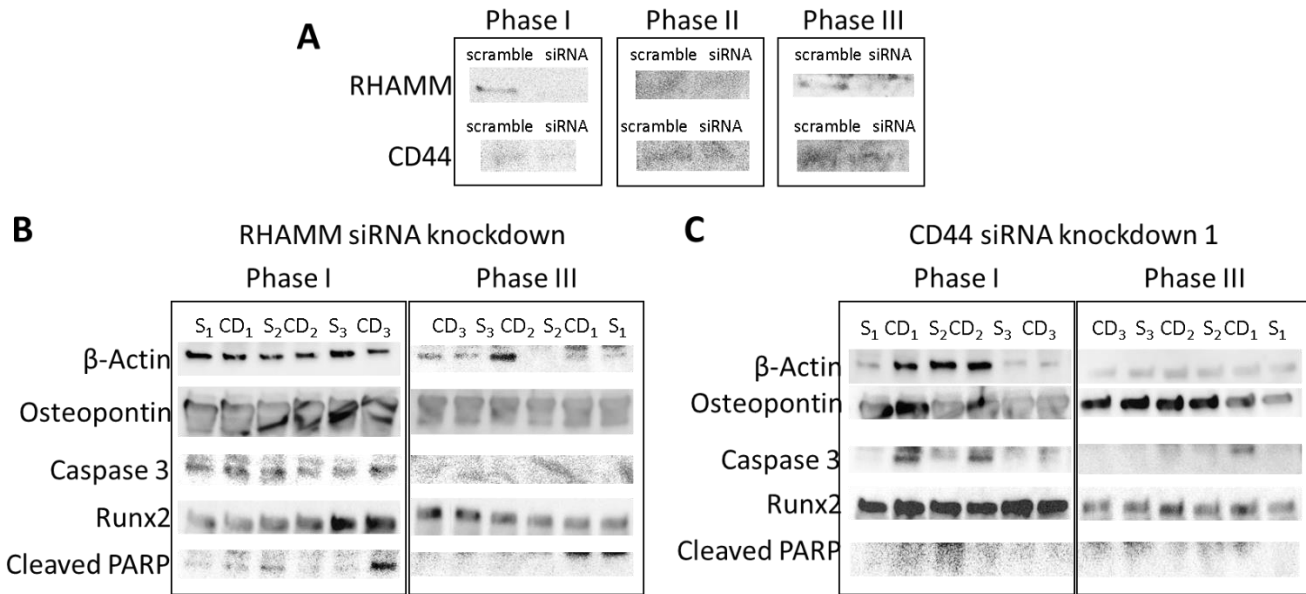


Figure 2.11: Images of western blots used for quantitative analysis of protein expression.

(A) The siRNA induced knockdown of RHAMM (top) and CD44 (bottom). Protein expression of several different markers as well as β-actin which was used as a control for the RHAMM siRNA knockdown experiments (B) and CD44 siRNA knockdown experiments (C).

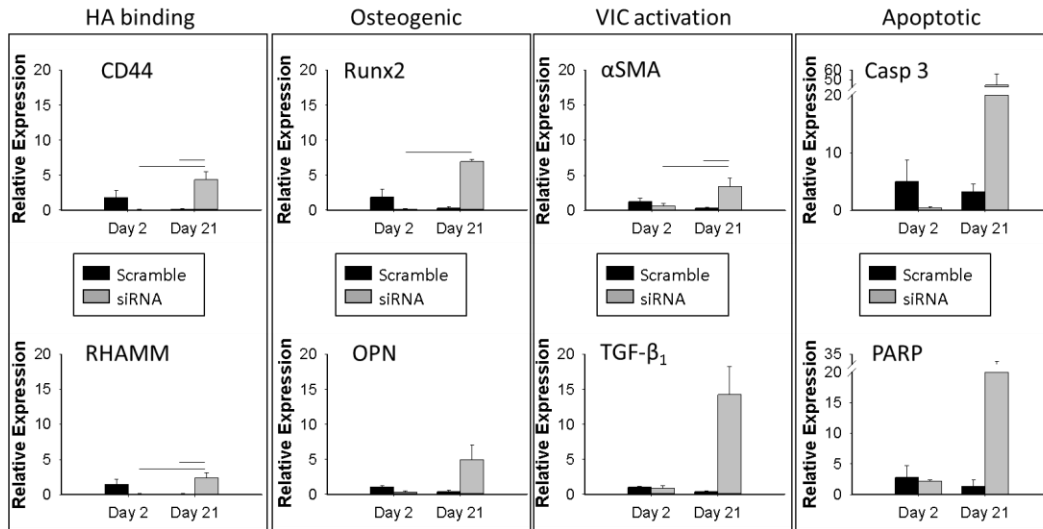


Figure 2.12: The relative RNA expression was measured for CD44 siRNA knockdown VICs grown on 35 kPa collagen PAAM gels.

The relative RNA expression is normalized to the scrambled siRNA samples at day 2. A two-way ANOVA showed there was a significant interaction ($p=0.015$) between time and knockdown with the siRNA on CD44 expression and a significant interaction ($p=0.021$) between time and the knockdown with RHAMM expression. The RNA expression of the osteogenic marker Runx2 did not have a normal distribution, but the ANOVA on the ranks shows an increase in Runx2 expression at day 21 in the CD44 knockdown VICs. The other osteogenic marker, OPN did not show a significant difference in expression. Of the activation markers, α SMA showed a significant interaction ($p=0.047$) between the two factors, while there was no statistical significance in the TGF- β_1 expression. Both apoptotic markers also did not have a normal distribution of expression and no significance was seen with the rank test. Tukey post-hoc testing results are shown with lines over the bar graph and have a $p<0.05$.

Chapter 3. Conditional deletion of RB1 in the Tie2 lineage leads to aortic valve regurgitation

This chapter is modified from a paper published in the Journal PlosOne entitled “Conditional deletion of RB1 in the Tie2 lineage leads to aortic valve regurgitation” in which I was a co-first author with Marina Freytsis.¹²⁷ From the published work, this chapter updates part of the text to include a figure that was not published, but is related to the project. To distinguish my data from Dr. Freytsis, I have noted in the figure legends data that she collected and analyzed. In general, Dr. Freytsis was responsible for working directly with the knockout mice, including taking echocardiogram data, isolating the mice hearts for my measurements, and the cell experiments involving cytokine analysis and the proliferation/apoptosis assays.

The other authors included in the publication and their contributions are described here. Drs. Liu and Georgakoudi advised on the multiphoton imaging and Dr. Liu helped develop the Matlab code used both to calculate the MAF and to create the representative MAF images. Dr. Black contributed to writing and approval of the final manuscript, the conception and design of the experiments, and data analysis and interpretation. In addition to contributing to the writing and approval of the final manuscript, the conception and design of the experiments, and data analysis and interpretation, Drs. Hinds and Huggins were directly involved in the creation for the pRb knockout and heterozygous pRb mice. Drs. Black, Hinds and Huggins also all contributed financially (NIH – NHLBI Award # R01HL114794).

Abstract

Calcific aortic valve disease (CAVD) a complex process involving changes to the extracellular matrix (ECM) and valve interstitial cell (VIC) activation. The role of the retinoblastoma protein (pRb) has not been explored in the context of CAVD, but its role in mesenchymal cell differentiation, including in bone development and mineralization, warrants further investigation. In this study, a mouse model of conditional pRb knockout (cKO) in the aortic valve regulated by Tie2-Cre-mediated excision of floxed *RB1* alleles was created. Significantly more aortic valve regurgitation, measured by echocardiography, was found in aged pRb cKO animals compared to pRb het control mice. The pRb cKO aortic valves had increased leaflet thickness without increased cellular proliferation and histologic studies demonstrated intense α -SMA expression in pRb cKO leaflets associated with disorganized extracellular matrix and increased leaflet stiffness. Increased calcification was measured in pRb cKO mice using an optical method to detect mineralized fluorescence. These studies demonstrate that pRb loss in both animal models and using *in vitro* model systems is sufficient to cause age-dependent aortic valve dysfunction and mineralization.

3.1 Introduction

Aortic valve disease is a complex disease process characterized by progressive thickening and fibrosis of the aortic valve leaflets leading to valve sclerosis, a precursor to valve mineralization and often frank bone formation that can cause restriction and/or regurgitation of blood flow from the heart. Statistics from 2017 indicate that more than 100,000 patients received an aortic valve replacement¹²⁸ and the prevalence of aortic valve disease increases markedly with age.¹²⁹ There is an important need to determine

the molecular mechanisms contributing to aortic valve disease because the only treatment for advanced disease is surgical replacement⁹¹ as medical therapy has not been found effective at slowing disease progression.^{130,131}

During embryonic heart development, cells derived from the endocardium,¹³² the secondary heart field, and the neural crest¹³³ can be found in the fibrosa, spongiosa, and ventricularis layers of the aortic valve.¹³⁴ Following valve development, the valve interstitial cells (VICs) predominantly have an endothelial origin,⁵⁵ likely the result of endothelial-to-mesenchymal transformation of endocardial cells. Further supporting an endothelial origin of VICs, Tie2 lineage tracing studies produce strong staining of the aortic valve leaflet¹³⁴⁻¹³⁶. With age, the adult aortic valve increasingly includes CD45-positive cells derived from the hematopoietic system¹³⁷ that would also be expected to be derived from the Tie2 lineage.¹³⁸ Though normally quiescent, VICs can become activated, and differentiate into myofibroblasts expressing alpha smooth muscle actin (α -SMA).¹³⁹

VICs produce an array of precisely oriented structural matrix proteins necessary for the leaflet to bear the load during diastole, while also sufficiently flexible to impart negligible outflow resistance during systole.^{140,141} In the diseased valve activated VICs deposit and reorganize the extracellular matrix (ECM)¹⁴²⁻¹⁴⁴ leading to rearrangement of collagen fibers in the fibrosa and proteoglycan changes in the spongiosa layers.^{19,145} ECM disarray precedes development of CAVD, particularly in the aorta-facing fibrosa where calcific nodule and bone formation first appear.^{61,129,146}

The retinoblastoma protein (pRb) regulates two key factors relevant to aortic valve disease: maintenance of mesenchymal cell differentiation as well as bone formation and

soft tissue calcification.¹⁴⁷⁻¹⁵⁰ Given the mesenchymal nature of VICs and the appearance of osteogenesis in diseased human valves, we hypothesized that VICs deficient in pRb would lose their quiescent phenotype (they would become activated), leading to aortic valve dysfunction possibly resulting in leaflet mineralization. To interrogate this hypothesis we created a mouse model of targeted pRb loss using Tie2 directed cre recombinase expression because many of the VICs in the aortic valve leaflets are derived from endothelial cells^{55,134} and Tie-2-cre effectively deletes genes in endothelial-cell-derived VICs resident in the aortic valve leaflets.^{134,135,151} Our results demonstrate that pRb in the Tie2 lineage is necessary to maintain aortic valve structure and function with age.

3.2 Methods

3.2.1 Animals

The flox19-RB1 (*RB1^{fl/fl}*) mice¹⁵² were maintained in a C57BL/6 background. *RB1^{fl/fl}* females were bred to Tie2-Cre males, purchased from Jackson laboratories (B6.Cg-Tg (Tek-cre)1Ywa/J). *RB1^{fl/fl};Tie2-Cre⁻* and *RB1^{fl/+};Tie2-Cre⁺* from the first cross were bred to generate *RB1^{fl/fl};Tie2-Cre⁺* (pRb cKO) and *RB1^{fl/+};Tie2-Cre⁺* (pRb het) mice for our experiments. The use of pRb het mice as controls is justified given the lack of observed phenotype. Genotype was determined by PCR analysis of genomic DNA from mouse tails. Genomic DNA was isolated and amplified by PCR using the following primers: *RB1*: 5'-GGC GTG TGC CAT CAA TG-3' (forward primer) and 5'-AAC TCA AGG GAG ACC TG-3' (reverse primer); Cre: 5'-GTG AAA CAG CAT TGC TGT CAC TT-3' (forward primer) and 5'-GTG AAA CAG CAT TGC TGT CAC TT-3' (reverse primer).

For further verification of Tie2 activity, Tie2-Cre mice were bred to B6 mice bearing the targeted insertion of a floxed(stop)CAG-TdTomato allele into the ROSA26 locus (strain Ai9, JAX#007909), such that a red fluorescent protein variant (tdTomato) is seen where Cre is expressed. Tissues from 2-4 month old Ai9;Tie2Cre mice were used for histological evaluation of recombination based on TdTomato fluorescence.

A total of 39 mice (15 experimental mice and 24 control mice) were used for these studies. 25 mice died for experimental endpoints and 9 mice died because in the opinion of the Division of Laboratory Animal Medicine and the investigators euthanasia was required for humane endpoints. 5 animals died without obvious cause or antecedent illness. Humane endpoints were defined as follows: Any animals displaying signs of distress including hunched posture, piloerection, labored breathing, tumors exceeding 5mm in any dimension, inability to eat or drink, or loss of 10% or more of body weight will be sacrificed within 24hrs. Aged mice with detectable valve dysfunction were watched closely and euthanized if they showed signs of edema or tachypnea with decreased cage movement that would be consistent with congestive heart failure. Animals were monitored 3 times per week and 24hours post echocardiograph procedures. Researchers handling mice went through mandatory animal handling training at Tufts University for proper evaluation of mouse health. Mice received water and food ad libitum, housed in cohorts of not more than 5 adults, and were otherwise maintained in accordance with a protocol approved by the Tufts University Institutional Animal Care and Use Committee (Protocol #: B2013-42 and B2016-11).

3.2.2 Echocardiography

In vivo valve structure and function were evaluated at 2 and up to 12 months of age for all animals, and a subset at 6 months, using an ultra-high frequency, high-resolution ultrasound (Vevo2100; VisualSonics, Inc., Toronto, ON, Canada). The chests of the mice were treated with a chemical hair remover to reduce ultrasound attenuation. Mice were anesthetized with 1-2% isoflurane inhalation, and placed on a heated platform to maintain temperature during the analysis. Two-dimensional imaging was recorded with a 40 MHz transducer to capture long-axis projections with guided B-Mode and color and pulsed-wave Doppler. Doppler interrogation was performed on the aortic valve outflow in the parasternal long-axis view to assess stenosis and regurgitation using a sample volume toggle to optimize the angle of interrogation. A modified right parasternal long-axis view was required in some cases to ensure ascertainment of the maximum velocity. Color flow Doppler echocardiography, in which flow movement toward the transducer is shown in red and that away from the transducer is shown in blue, was applied at sampling points indicated in the 2-dimensional images from a long-axis view. Measurements of ventricular function and peak gradient were calculated using the integrated software of the Vevo1200. Aortic regurgitation was defined by retrograde blood flow across the aortic valve into the left ventricular outflow tract for more than half of the diastolic period identified by Doppler echocardiography and by color-flow Doppler video. ImageJ was used to calculate aortic root diameter in diastole from B-mode stills, with 3 cycles averaged per animal.

3.2.3 Blood Pressure Measurement

Blood pressure was measured in normal diet fed mice aged 10-12 months by tail cuff plethysmography using the Kenda Coda System. Mice were acclimated and trained for 2-3 days by 20 tail cuff inflations. For the following 2 days, blood pressure measurements were recorded and averaged for each mouse. At least 3 mice from each sex and genotype were used for this analysis.

3.2.4 Histology

Hearts from 2-month-old and aged animals were harvested, rinsed well in cold PBS, and fixed for up to 24 hours in 10% neutral buffered formalin. Fixed hearts were submitted to the Jackson Laboratories Histology lab for processing, paraffin embedding, and sectioning. The tissues were processed overnight on a sakura tissue-tek VIP tissue processor. Blocks were grossly trimmed for correct orientation and embedded in paraffin. Blocks were faced to appropriate area (3 leaflets present) using 4x objective on microscope. 5um thick sections were taken of area 3-4 sections per slide. H&E stained slides were stained on Leica Autostainer XL and the Pentachromes were done using American Mastertech "Russel-Movat" Pentachrome kit. Images of the Movat stained valves were also taken with a Nikon 800E microscope using a 10x objective. Histological images from six Rb het and six cKO were analyzed to look at GAG composition as a percentage of total valve area. The images were first processed with Adobe Photoshop CC 2015 to isolate the valve, removing background blood and other debris from the images. Next, the RGB images were broken into the corresponding red, green, and blue images so that the Movat stain for GAGs (light blue) could be isolated. Using Cell Profiler

¹⁵³, the images were inverted and the red and green channels were combined (in a 1:1.1 ratio) and the blue channel (multiplied 1.4 times) was subtracted from the result. This resulted in an image that was used to isolate the GAG area using a manual threshold. The total area of the valve was found using a manual threshold of the green channel and was used to calculate the GAG percentage area for each sample image.

3.2.5 Mineralization Associated Fluorescence Intensity Imaging

Images of whole, isolated aortic valves were taken using a Leica TCS SP2 (Wetzlar, Germany) confocal microscope equipped with a Ti:sapphire laser (Spectra Physics, Mountain View, CA) and a dry Leica 20x/0.7 NA objective. Two z-stacks for three valves from each of the groups (pRb het and pRb cKO mice) were taken using an 800 nm excitation wavelength. Two emission spectral bands 460 nm \pm 20 nm and 525 nm \pm 25 nm were collected during each measurement. The mineralization associated fluorescence (MAF) was calculated for each sample using our previously developed method.¹⁵⁴ The MAF of each image in a stack was calculated and then averaged to give the MAF value for the zone on the sample. Zones were then averaged to give the MAF contribution for each valve leaflet sample.

3.2.6 Immunohistochemistry

Sections were deparaffinized and rehydrated in graded ethanol washes. After blocking in 5% normal serum or BSA, sections were incubated overnight at 4°C with the following antibodies: anti- α -SMA (Abcam ab5694, 1:1000) and anti-phospho-histone H3 (Cell Signaling #9701, 1:100). Alexfluor-conjugated anti-rabbit secondary antibodies were used to detect anti-pH3. Slides were mounted in Vectashield mounting media with DAPI (Vectorlabs H-1200) and visualized with fluorescence microscopy. HRP-conjugated anti-

rabbit secondary antibodies were used to detect anti- α -SMA, with subsequent DAB-based colorimetric detection. A no-primary antibody control was used for each antibody to detect false-positives and autofluorescence. TUNEL staining was performed using the ApopTag Fluorescein In Situ Apoptosis Detection Kit (EMD Millipore S7111), per manufacturer's instructions. Immunofluorescent stained sections were imaged on a Nikon 800E epifluorescent microscope with a Spot RT2 digital camera. Image analysis and quantification were performed in CellProfiler¹⁵³. The α -SMA stained images were taken using a Nikon 800E microscope using a 40x objective. Images were taken of the full valve (all three leaflets) and edited in Adobe Photoshop CC 2015 to remove any remnants of the aorta, starting at the root of each leaflet. CellProfiler was used to determine the area of the valve leaflets and the area of positive α -SMA staining in order to find the activated percentage area of each valve.

3.2.7 Atomic Force Microscopy

Valve tissue stiffness was measured using atomic force microscopy (AFM), with a Veeco Dimension 3100 AFM with Novascan borosilicate glass particle probes. We used probe tips (10 μ m diameter bead) with a rated spring constant value of 0.6 N/m and the Hertzian theory was used to calculate the Young's Modulus. The Young's Modulus was calculated using a MATLAB code for each indent curve over an entire 2D force volume and then averaging these values for each sample. From these measurements, we were able to calculate changes in valve tissue stiffness between groups.

3.2.8 Second Harmonic Generation Imaging

Second harmonic generation signal from collagen fibers was collected using a Leica TCS SP2 microscope equipped with a Ti:Sapphire laser which provided 800 nm excitation, dry Leica 20x/0.7 NA objective, and 400 nm \pm 10 nm (ET400/20X) filter. At least 2, 3D volumes of valve leaflet were analyzed for each sample valve (n=3 for both pRb het and cKO valves). Fiber orientation and variance were determined using a previously described method that relies on a weighted vector summation approach. The two-dimensional variance is a metric of the collagen fiber alignment that has a value of one for completely disorganized fibers and zero for all fibers within a field exactly aligned in the same direction ¹⁵⁵.

The SHG images were also used as a metric of fibrosis. After masking images for SHG signal only, image stacks were analyzed to find the average pixel intensity, as a measure of collagen fibrosis ¹⁵⁶, per image. The stack of images was averaged to find a single value for each location. The data was then normalized to one.

3.2.9 LC-MS/MS Proteomics

Individual aortic valve leaflets were excised from flash frozen hearts; the three aortic leaflets from a single animal were collected and pooled to generate one sample; three aortic samples per genotype (for a total of six animals; three of each type) were analyzed and weighed (all measured at 0.01mg of tissue for each sample). Valve leaflets were lyophilized for six hours before undergoing a urea digested at 4°C using a stir bar to agitate the sample. Sample protein was then collected with an acetone precipitation ¹⁵⁷. Samples were then frozen before being sent to Beth Israel Deaconess Medical Center Mass

Spectroscopy Core Facility for liquid chromatography–tandem mass spectroscopy (LC-MS/MS) analysis. Trypsin was used to digest the protein prior to analysis. Spectra with a 95% confidence were kept for analysis; there was an average spectral count of 690 for each sample and a total of 395 identified proteins. Resulting spectral counts were used to quantify abundance of cellular proteins and ECM proteins then individual counts were normalized by total spectral counts of cellular and ECM proteins collected per sample. ECM and cellular proteins with fold changes of either greater than 1.5 times or less than 0.6 times for the pRb het samples compared to the pRb cKO were included in a principle component analysis (PCA) with functional data (stiffness measurements and variance quantification) collected previously on the leaflets. PCA was done in SigmaPlot (Systat Software, San Jose, CA) using a correlation matrix and average eigenvalues for the components. The component scores and component loadings were plotted using MATLAB. The component scores were grouped using the *k*-means cluster algorithm (*k*=2), as previously described^{158,159}, in MATLAB; the loading scores were also grouped using *k*-means clustering (*k*=4). Both algorithms were iterated 100 times to help assure convergence of the cluster centroids. ECM proteins were classified using the MatrixDB¹⁶⁰.

3.2.10 Serum collection and analysis

Blood was collected after an overnight fast by cardiac puncture immediately after euthanasia. Serum was collected after clotting and centrifugation, the stored at -80°C. Cytokines were analyzed by a multiplexed ELISA array (Aushon BioSystems, Inc; Mouse Cytokine 1 CiraPlex™ Array) on Cirascan™ immunoassay system (Aushon BioSystems, Inc.)

3.2.11 Statistical analysis

Aortic regurgitation incidence was evaluated with a two-tailed Fisher's exact test. Other metrics were tested with an unpaired, two tailed Student's T-test. Differences were considered significant at P-value <0.05.

3.3 Results

3.3.1 Deletion of pRb in murine aortic valve leaflets produces aortic valve regurgitation

Because whole-body RB1 knockout mice die in utero ¹⁶¹, we utilized a conditional knockout model strategy whereby mice with loxP-flanked exon 19 of RB1 (RB1^{fl/fl}) were crossed with Tie2-Cre mice to delete pRb from the aortic VICs, as well as other endothelial-derived tissues ¹³⁶. Tie2 activity in the majority of VICs throughout the aortic leaflets was confirmed by TdTomato expression in Tie2-Cre; Ai9 mice (**Figure 3.1 A**). Mice homozygous for RB1^{fl/fl} and heterozygous for the Tie2-Cre transgene are designated conditional pRb knockout (pRb cKO) mice while littermate RB1^{+/fl};Tie2-Cre⁺ mice were used as heterozygous (pRb het) controls. pRb cKO mice were viable and demonstrated a Mendelian ratio at weaning (χ^2 P value = 0.86). Our experimental protocol designated echocardiographic and histologic analysis at one year of age, though more pRb cKO than het mice died or were sacrificed for humane reasons before that time (2 pRb het vs. 7 pRb cKO mice; **Figure 3.8**). The reason for premature death in pRb cKO mice is not precisely known; however, Tie2-Cre also drives recombination in hematopoietic stem cells ¹³⁸, and pRb-deficiency in hematopoietic cells can cause myeloproliferative disease ^{162,163}.

We aged 24 pRb het animals and 15 pRb cKO animals; at two and six months the aortic valve function was normal in pRb cKO and het animals by echocardiography. At 10-12 months of age (referred to as “aged” mice throughout the manuscript), 5 of 11 living pRb cKO mice were found to have severe aortic valve regurgitation (AR) identifiable by color flow Doppler (**Figure 3.1 B and D**), while AR was not observed in 20 aged pRb het mice (**Figure 3.1 C; Table 3.1**). Three additional pRb cKO mice had mild or trace AR. The mean \pm SD peak velocity of the regurgitant jet was -2113 ± 1967 mm/s in pRb cKO mice. The aortic root diameters measured by B-mode echocardiography during systole in pRb cKO and het animals were similar (**Table 3.1**), consistent with AR not being secondary to dilation of the aortic root. Functional aortic valve stenosis was not found in any animal during our study. pRb cKO heart weights normalized to tibia length were significantly heavier than pRb het hearts, suggesting mild left ventricular hypertrophy with preserved contractile function (**Table 3.2**). We considered whether increased afterload might explain the AR; however, tail cuff blood pressures in pRb cKO and het mice were similar (**Table 3.2**).

Table 3.1: Hemodynamic evaluation and aortic root diameter of aged mice

	pRb Het		pRb cKO	
	Female (n)	Male (n)	Female (n)	Male (n)
Peak velocity (mm/s)	1205 \pm 86 (6)	1426 \pm 158 (6)	1206 \pm 38 (4)	1482 \pm 94 (8)
Peak gradient (mmHg)	5.96 \pm 0.83 (6)	8.64 \pm 1.63 (6)	5.83 \pm 0.36 (4)	8.99 \pm 1.17 (8)
Aortic Valve Root Diameter (mm)	1.17 \pm 0.03 (11)	1.22 \pm 0.03 (10)	1.22 \pm 0.05 (5)	1.28 \pm 0.05 (7)

Table 3.2: Evaluation of heart function, weight, and systemic blood pressure in aged mice

	pRb Het		pRb cKO	
	Female (n)	Male (n)	Female (n)	Male (n)
Heart Rate (beats/min)	702 ± 52 (3)	595 ± 20 (5)	615 ± 55 (4)	609 ± 72 (4)
EF (%)	66.38 ± 5.39 (3)	60.28 ± 3.88 (5)	68.16 ± 7.74 (4)	59.38 ± 3.66 (4)
FS (%)	36.25 ± 3.89 (3)	32.14 ± 2.73 (5)	38.62 ± 5.61 (4)	31.46 ± 2.43 (4)
Systolic BP	112.73 ± 7.06 (3)	134.83 ± 6.74 (5)	115.23 ± 4.81 (4)	122.21 ± 2.85 (4)
Diastolic BP	78.05 ± 4.43 (3)	95.60 ± 3.19 (5)	80.96 ± 2.95 (4)	84.20 ± 3.54 (4)
Normalized Heart Weight (mg/mm)	87.11 ± 3.5 (8)	119.2 ± 5.2 (7)	112.8 ± 10.8 * (4)	147.3 ± 5.8 ** (7)

EF, ejection fraction; FS, fractional shortening; BP, blood pressure. Heart weight normalized to tibia length. Values shown are mean ± SD. T-test: *P-value = 0.016, **P-value = 0.0036; sex-matched cKO compared to Het.

3.3.2 Loss of pRb causes ECM remodeling and VIC activation

We next analyzed fixed heart sections using histological stains to determine if morphological changes are present in the pRb cKO aortic valves. Masson's Trichrome staining showed a more diffuse or weak collagen staining pattern in pRb cKO valves with AR (**Figure 3.2 A**). Additionally, Movat pentachrome stain showed changes within the collagenous fibrosa layer of pRb cKO valve leaflets; cKO valves had a significantly higher GAG content (**Figure 3.2 B and D**). In every pRb cKO valve, from mice with or without aortic valve regurgitation, intense α -SMA staining was observed throughout the leaflets compared with pRb het leaflets (n= 7 het, 3 cKO with AR, 4 cKO without AR; **Figure 3.2 C**). By comparison, aortic valve leaflets from 2-month-old pRb cKO mice showed a pattern of histological and α -SMA staining similar to het mice, consistent with the changes in valve architecture at 10-12 months being associated with aging (**Figure 3.10**). Aortic root and valve leaflet calcification were not observed by Alizarin Red and Von Kossa staining (**Figure 3.9**). However, using a more sensitive method developed in our lab using two-photon

excited fluorescence to calculate the mineralization associated fluorescence (MAF) showed a significant increase in calcification in the pRb cKO mice (**Figure 3.3**).

3.3.3 pRb cKO aortic valve leaflets show similar proliferation and apoptosis

Given the well-established role for pRb in cell cycle regulation ¹⁶⁴ and because VIC proliferation and apoptosis have been observed in diseased human aortic valves ¹⁶⁵, we asked whether differences in proliferation and cell death were found in the pRb cKO aortic valves. Cellular proliferation, measured by phospho-histone H3 expression (p-H3; **Figure 3.4 A and B**), and apoptosis, measured by TdT-mediated dUTP-biotin nick end labeling (TUNEL; **Figure 3.4 A and C**) were infrequently and similarly observed in both groups. Thus, differences in cell cycle regulation do not explain valve dysfunction in the pRb cKO mice. Furthermore, there was no significant difference in the number of DAPI-positive nuclei within the valve leaflets (**Figure 3.4 D**). Interestingly, the nuclear density, assessed by the number of DAPI-positive nuclei normalized to cross-sectional leaflet area, was significantly lower in pRb cKO aortic valve leaflets than controls (**Figure 3.4 E**). These results are consistent with expansion and remodeling of the extracellular matrix rather than cellular proliferation being responsible for pRb cKO aortic valve thickening.

3.3.4 pRb cKO valve leaflets have disordered matrix and increased stiffness

We next asked whether the increased leaflet thickening observed in pRb cKO mice was associated with structural changes in the ECM using two non-destructive microscopy techniques. Second harmonic generation (SHG) analysis of collagen fiber orientation demonstrated more variable collagen structural organization in leaflets from pRb cKO mice compared with control animals (**Figure 3.5 A**). Collagen disorganization in experimental animals was further demonstrated by quantitative analysis of pixel-wise

fiber orientation (**Figure 3.5 B**), which revealed a bimodal distribution in the pRb cKO aortic valve leaflets compared with a unimodal distribution of the pRb het leaflets. The 2D variance, a metric of the overall collagen fiber alignment, was significantly increased in pRb cKO valves, corresponding to increased fiber disorganization (**Figure 3.5 C**). Next, using atomic force microscopy (AFM) we found that pRb cKO valves have a higher Young's Modulus than controls consistent with increased leaflet stiffness (pRb het valves 17.44 ± 3.8 kPa versus cKO valves 23.18 ± 3.1 kPa (**Figure 3.5 D**)). Greater SHG intensity further indicated that the Rb cKO valves are more fibrotic than Rb het valves (**Figure 3.5 E**). Taken together, these results demonstrate that the aortic valve thickening observed in pRb cKO aortic valves is associated with a loss of the normally ordered array of valve collagen and ECM resulting in a stiffer valve leaflet.

3.3.5 Loss of pRb in VICs results in structural changes in the ECM of aortic valve leaflets

To better characterize ECM changes in cKO valves we performed proteomic analysis on pRb het and cKO aortic valve leaflets. Proteomic analysis of the leaflets revealed a diverse group of proteins present in both the het controls and pRb cKO valves. Using principle component analysis (PCA) we created component scores for each valve sample based on proteins that were found in pRb cKO and het control valves. The PCA scores show distinct clustering of the pRb het valves and more varied distribution of the pRb cKO valves (**Figure 3.6 A**), consistent with heterogeneous changes in the proteome caused by the loss of pRb. Additionally, sorting by ECM class shows minor variation in protein composition (**Figure 3.6 B**). Individual normalized protein spectral counts from collected LC MS/MS data and statistical comparisons of the data can be found in **Figure 3.11**. Lastly, to correlate the direct effect of structural ECM components with the measured leaflet functional data, we

performed a second PCA and plotted loading scores of the structural ECM components with the stiffness and variance functional data derived from the SHG and AFM analysis, respectively (**Figure 3.6 C**). These findings demonstrate that the functional measurements of stiffness and ECM variance clustered with ECM components important for tissue mechanics or matrix remodeling, respectively.

3.3.6 Increased cytokine levels in aged pRb cKO mice

Because inflammation is a key driver of the early stages of aortic valve ¹⁴⁶ disease we asked whether systemic inflammation was increased in pRb cKO mice. Tie2-cre drives recombination in hematopoietic stem cells ¹³⁸, and conditional knockout of pRb in hematopoietic cells causes myeloproliferative disease ¹⁶³. pRb cKO mice were found to have splenomegaly, bone marrow cellular expansion, and a relative increase in the bone marrow monocyte population (**Figure 3.12**). Since monocytes have been described in early CAVD lesions and secrete pro-inflammatory cytokines ¹⁴⁶, we asked if markers of systemic inflammation were increased in pRb cKO mice using a cytokine ELISA array. TNF α , IL-10, and IL-17 were elevated in aged pRb cKO mice, compared to controls (**Figure 3.7**). Interestingly, IL-17 was only elevated in cKO mice with aortic regurgitation (black symbols). The presence of elevated circulating cytokines suggests that inflammation present in the cKO mice may be contributing to aortic valve pathology and valve dysfunction.

3.4 Discussion

In this report, we demonstrate that conditional pRb loss in the Tie2 lineage is sufficient to cause age-dependent aortic valve thickening, ECM disorganization and regurgitation reminiscent of human fibrotic valvular disease or aortic valve sclerosis, a stage that

precedes frank CAVD.⁹¹ Our model differs from several other mouse models of aortic valve disease, where dysfunction is caused by defective embryonic valve development or aortic valve regurgitation secondary to aortic root dilation and leaflet prolapse; however, it is similar to existing models in that the primary outcome is aortic insufficiency and limited calcification, likely due to the hemodynamic differences between mouse and man.^{166,167} pRb cKO pups were weaned at an expected Mendelian ratio and were found to have normal valve histology at 2 months of age and normal valve function at 6 months, arguing against a developmental effect. Instead, pRb cKO mice develop aortic valve pathology and dysregulation after 10-12 months of age without dilation of the aorta. Thus, our model recapitulates features of age-dependent aortic valve dysfunction including regurgitation commonly observed in humans. Intriguingly, two members of a human family carrying a retinoblastoma gene mutation have been found to have a bicuspid aortic valve potentially strengthening the importance of RB1 in aortic valve disease.¹⁶⁸

When healthy aortic valves transition to diseased valves, the resident VICs transition from a quiescent fibroblast phenotype to a state of activation resembling myofibroblast-like cells, which express mediators that can promote tissue remodeling. Similarly, the most striking molecular difference between pRb deficient and control valves was increased α -SMA expression throughout the leaflets of all aged pRb cKO valves, consistent with activation of pRb-deficient VICs into myofibroblasts. Because α -SMA expression was increased in all cKO valves, even when aortic valve regurgitation was not present, this finding is consistent with pRb being necessary to prevent the state of VIC activation that precedes ECM remodeling and valve dysfunction in our model.

A prevailing hypothesis in the field is that pathogenesis of aortic valve disease results from dysregulation of the regulatory pathways that control late embryonic valve development.^{169,170} Consistent with this theory, the reduced cellular density without changes in proliferation index within the aortic valve leaflets of pRb cKO mice is reminiscent of aortic valve remodeling during development.¹⁹ Given the role pRb plays in regulation of terminal differentiation of several mesenchymal lineages, our finding in aortic valve leaflets supports a role for pRb in promoting VIC differentiation and quiescence. This model suggests a cell autonomous role for pRb in regulation of VIC differentiation that is required to prevent age-dependent aortic valve dysfunction.

We speculate on two factors that we consider to be candidates for modulating the transition of VICs to myofibroblasts in a pRb-dependent manner: Runx family transcription factors and TGF- β . Both of these factors have been directly linked to development of the myofibroblast in disease states,¹⁷¹ as happens in aortic valve disease and in our model. Importantly, pRb and its regulators, the D-type cyclins and cyclin-dependent kinases (cdk), are well established to (a) directly influence Runx transcription factor function¹⁷² and (b) mediate the effects of TGF- β .¹⁷³ In the latter case, it is intriguing to speculate that TGF- β effects in cells in which pRb function is lost genetically as in our model or through physiological inactivation by cdk activity as may occur in diseased tissue may switch from proliferation-suppressive (mediated by functional pRb) to favor the transition to the myofibroblast.

In addition to a VIC cell-autonomous role for pRb in aortic valve disease our results cannot exclude a non-cell autonomous mechanism. We asked whether the loss of pRb in hematopoietic cells derived from the Tie2 lineage affected the immune system in pRb cKO

mice and whether there was increased inflammation, a known contributor to CAVD.¹⁷⁴ Several cytokines relevant to aortic valve disease were found to be increased in pRb cKO mice, including TNF α and IL-17. TNF α in particular is a pro-inflammatory cytokine that promotes CAVD progression.¹⁷⁵ The pro-inflammatory cytokine IL-17, which was specifically elevated in cKO mice with AR, is released from helper T-cells and functions to recruit monocytes into tissues.¹⁷⁶ While IL-17 has not been reported in association with CAVD, T-cell infiltration has been described in early lesions,¹⁷⁷ and a population of gamma/delta T-cells resident in the aortic valve and aortic root that secrete IL-17 has been reported.^{178,179} Although T-cell and monocyte infiltration in our model was not obvious by H&E staining of pRb cKO valves, additional studies are required to fully delineate the role of the immune system in pRb cKO mice with aortic valve disease. Nevertheless, increased circulating cytokine levels support the concept that inflammation may be a valve-extrinsic factor contributing to the aortic valve abnormalities in our model.

Histological sections showed ECM remodeling in aortic valve leaflets of pRb cKO animals with regurgitation, and more detailed, micron scale and protein level observations revealed substantial differences. Using SHG imaging, a sensitive technique for measuring differences in collagen architecture that does not require tissue destruction,¹⁸⁰ we observed increased collagen fiber variance and intensity in pRb cKO valve leaflets indicating a greater degree of ECM disorganization, which is characteristic of aortic valve disease.²² Additionally, pRb cKO valves had a higher measured Young's Modulus than controls, indicating further mechanical changes occurring in the diseased valve leaflets. A large body of literature has shown that increased substrate stiffness influences myofibroblast¹⁸¹ and osteoblast differentiation.¹⁸² Interestingly, pRb phosphorylation is inhibited at physiologic tissue stiffness and induced in pathological stiffness *in vitro*,

suggesting that pathologic matrix remodeling itself can regulate cell cycling and differentiation via the pRb pathway.¹⁸³

The loss of tight, parallel collagen fibers has been shown to contribute to aortic valve dysfunction and provide nucleation sites for calcification.^{146,184} We observed differences in protein composition between pRb cKO and control mice that clustered with leaflet stiffness and collagen variance. Collagen I, a major component of the overall matrix structure,¹⁸⁵ correlated with leaflet stiffness¹⁸⁶ and collagen fiber alignment was associated with fibrillins¹⁸⁷ and collagen XV,¹⁸⁸ a known regulator of ECM organization.¹⁸⁹ The compilation of individual spectral counts showed a statistical difference in collagen VI expression between the pRb cKO and control mice. Collagen VI plays an important role in valve morphogenesis and valve development so may contribute to valve pathology.¹⁹⁰ Evidence from the cancer field demonstrates that pRb negatively regulates MMP activity,¹⁹¹ suggesting a mechanistic link between pRb loss/inactivation and increases in ECM remodeling in the aortic valve. Taken together, these data suggest that the pathological remodeling observed in pRb cKO valves is consistent with early stages of human fibrocalcific aortic valve disease. We can only speculate whether frank valve calcification might have been present in even older pRb cKO mice.

3.4.1 Limitations to present study

In this report, we present a novel mouse model of aortic valve dysfunction; however, we acknowledge some limitations to this model. Because the Tie2-Cre driver is expected to cause recombination in cells other than VICs, we cannot exclude the possibility that our findings may be caused by the loss of pRb outside of the aortic valve. For example, using the Tie2-Cre driver does not allow us to rule out the unique contributions of circulating

endothelial and CD45+ cells, which are also in the Tie2 lineage^{54,138} and accumulate in the aortic valve in an age-dependent manner.^{137,192} Alternative Cre drivers, such as Periostin¹⁹³ or Nfatc1¹⁹⁴, that target VICs at different developmental time points, including cells not derived from the Tie2 lineage, may further clarify the contributions of *RB1* to aortic valve disease.

3.5 Conclusion

Here we present a model of CAVD, using Tie2 lineage pRb KO mice, which accurately mimics many of the disease characteristics in humans. While additional studies need to be done with pRb cKO mice to fully understand the contributions of the Tie2-cre system and the development of stenosis in the valves, these mice are potentially useful in the study of leaflet ECM changes and inflammation. The slow development of stenosis with minimal calcification, measure by MAF, suggests that pRb cKO mice may more accurately recapitulate CAVD in humans. Taken together, the pRb cKO mouse represents a model of age-dependent aortic valve regurgitation characterized by leaflet pathology, namely sclerosis, and circulating biomarkers of inflammation.

3.6 Figures

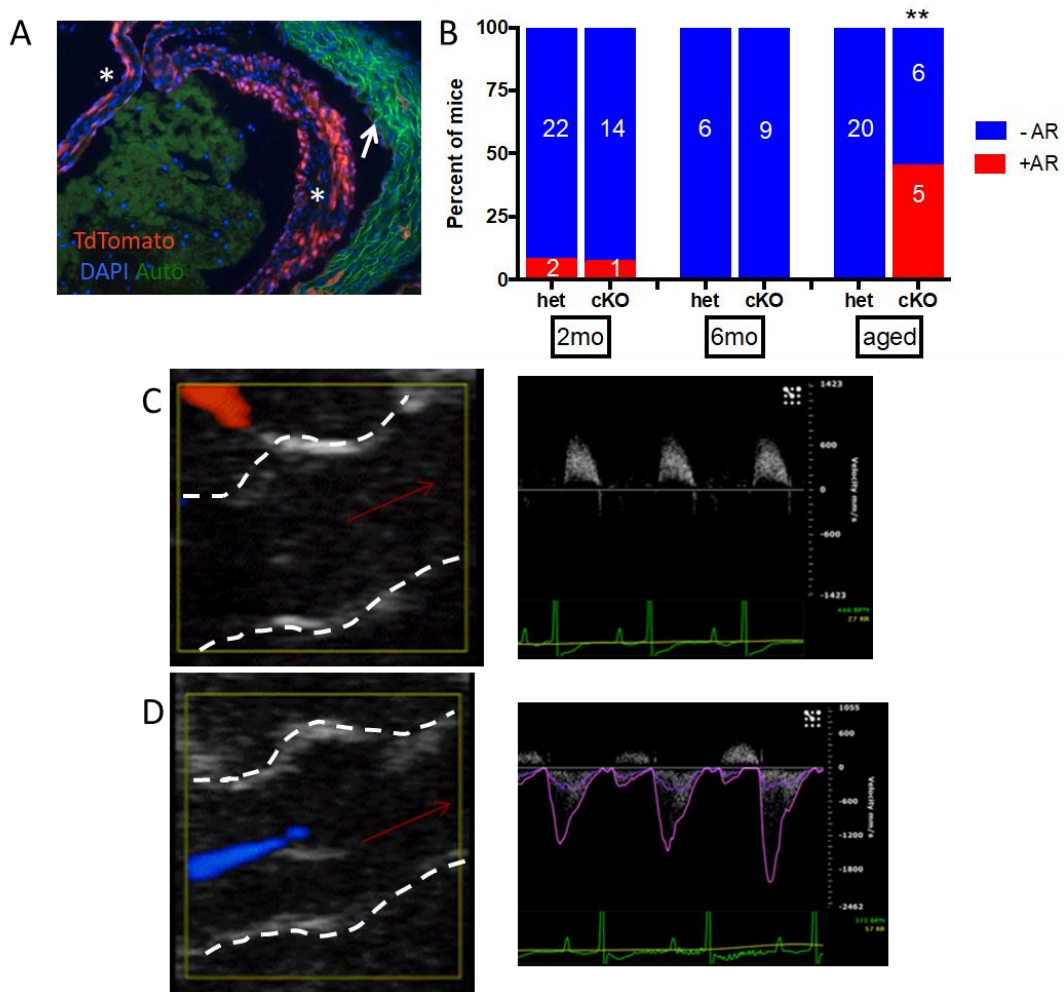


Figure 3.1: Tie2-driven loss of pRb causes aortic regurgitation (AR) with age.

(A) Confirmation of Tie2Cre-activity within leaflet of Ai9 mouse, where recombination throughout the leaflets (indicated by *) indicated by TdTomato fluorescence. Autofluorescence is seen in the aortic wall (indicated by arrow) (B) Incidence of AR, as evaluated with Doppler by a blinded analyst, with age (**, Fischer's exact test $p=0.0027$). "Aged" indicates 10-12 month old animal. Sex did not have an effect on regurgitation incidence within the pRb cKO group ($p=0.55$). (C-D) Representative images are presented of color Doppler during diastole (left panel, left ventricular and aortic root structures indicated by dashed white line and direction of blood flow indicated by red arrow) and Doppler flow velocity tracing recorded from the left ventricular outflow tract (right panel). (C) 2-month old animal. (D) Aged pRb cKO with regurgitation: regurgitant flow at the aortic valve was recorded as a blue flow in the left ventricle during diastole in addition to retrograde diastolic Doppler flow recorded from the ventricular outflow tract. This data was collected by Marina Freytsis.

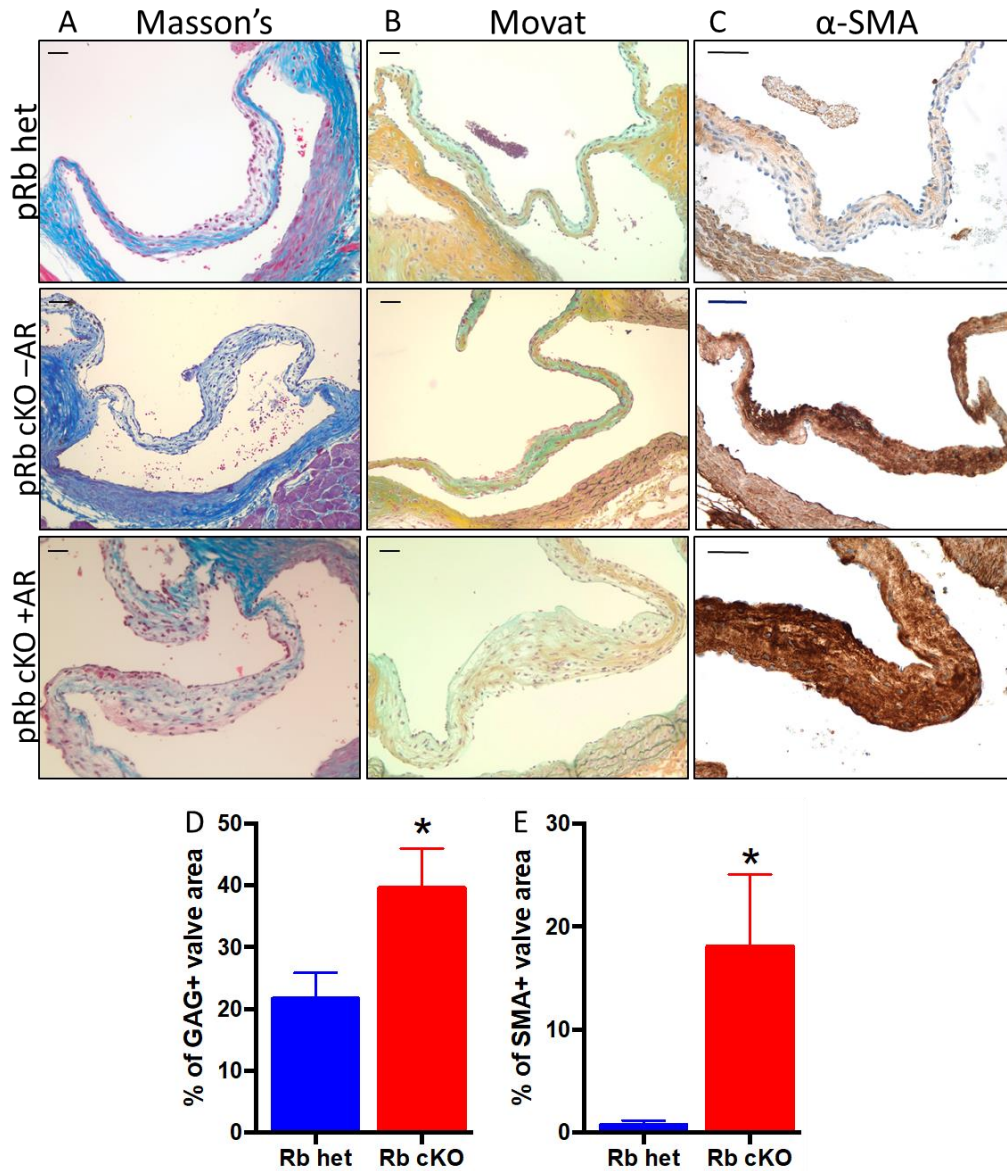


Figure 3.2: Representative histology of aortic valve leaflets from aged mice demonstrates changes in pRb cKO aortic valve.

(A) Masson's trichrome showing reduced collagen staining (blue) in leaflet from pRb cKO mouse with aortic regurgitation (AR). (B) Movat pentachrome showing more diffuse collagen staining (yellow) in fibrosa, but normal proteoglycan staining (blue) in the spongiosa layer of the leaflet from pRb cKO with AR. (C) Immunohistochemistry for α -SMA, demonstrating presence of activated myofibroblasts throughout leaflets of pRb cKO mouse with and without AR. Scale bar is 50 μ m. (D) Quantification of the percent area of the valve expressing GAGs using a Movat stain. Mean \pm SEM; Student T-test P-value = 0.04. (E) Quantification of α -SMA, represented as percent of valve area with positive staining. Mean \pm SEM; Student T-test P-value = 0.02. Figures A, B, and C were collected by Marina Freytsis.

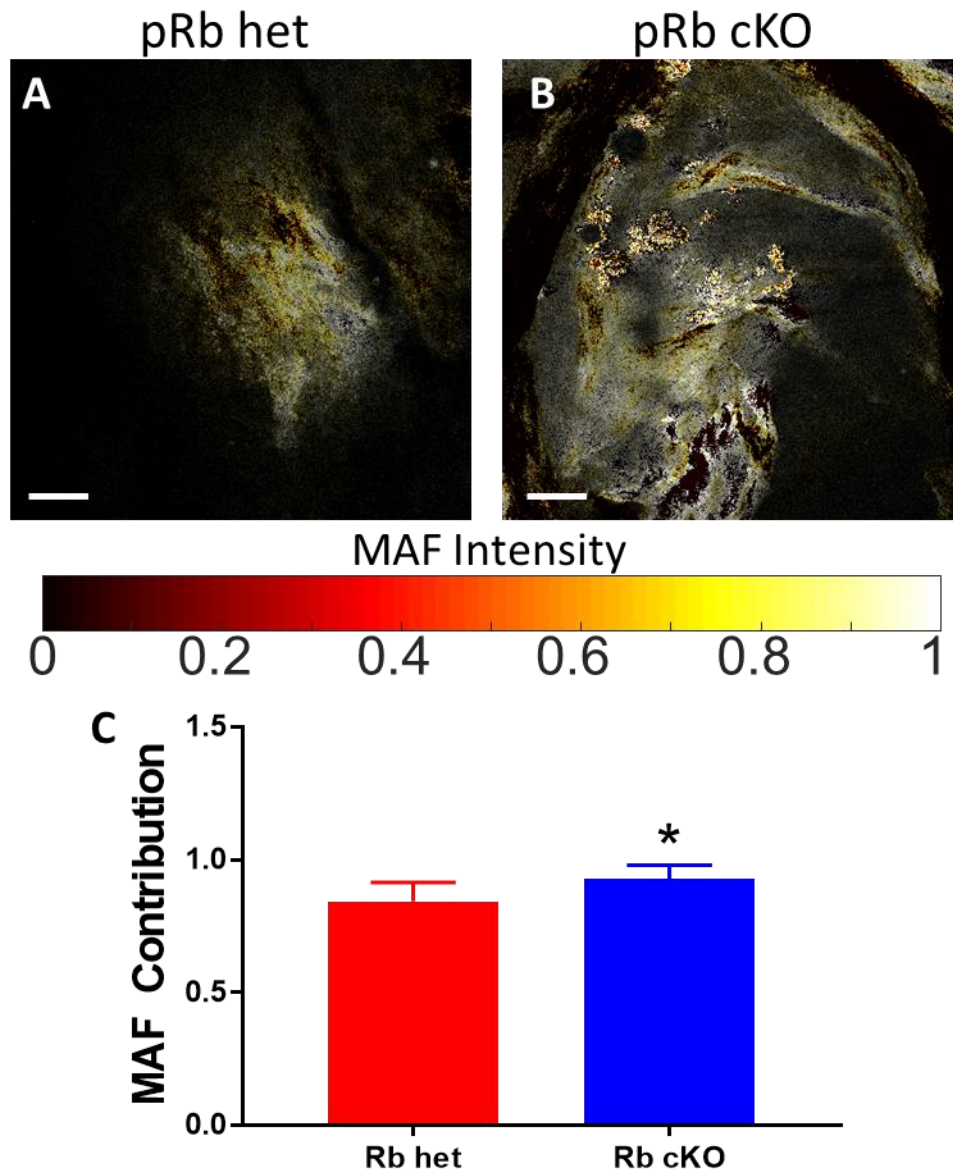


Figure 3.3: The calculated MAF of Rb het verse Rb cKO mice and representative images of each type of valve leaflet.

Representative image of the Rb het (A) and Rb cKO (B) showing the 525nm/460nm ratio with an excitation of 800nm. (C) From the 525nm/460nm ratio, the MAF contribution was calculated for each case and shows an increase in the amount of mineralized fluorescence present in the Rb cKO mice valve. Mean \pm SEM; Student T-test P-value = 0.0531; scale bar is 100 μ m

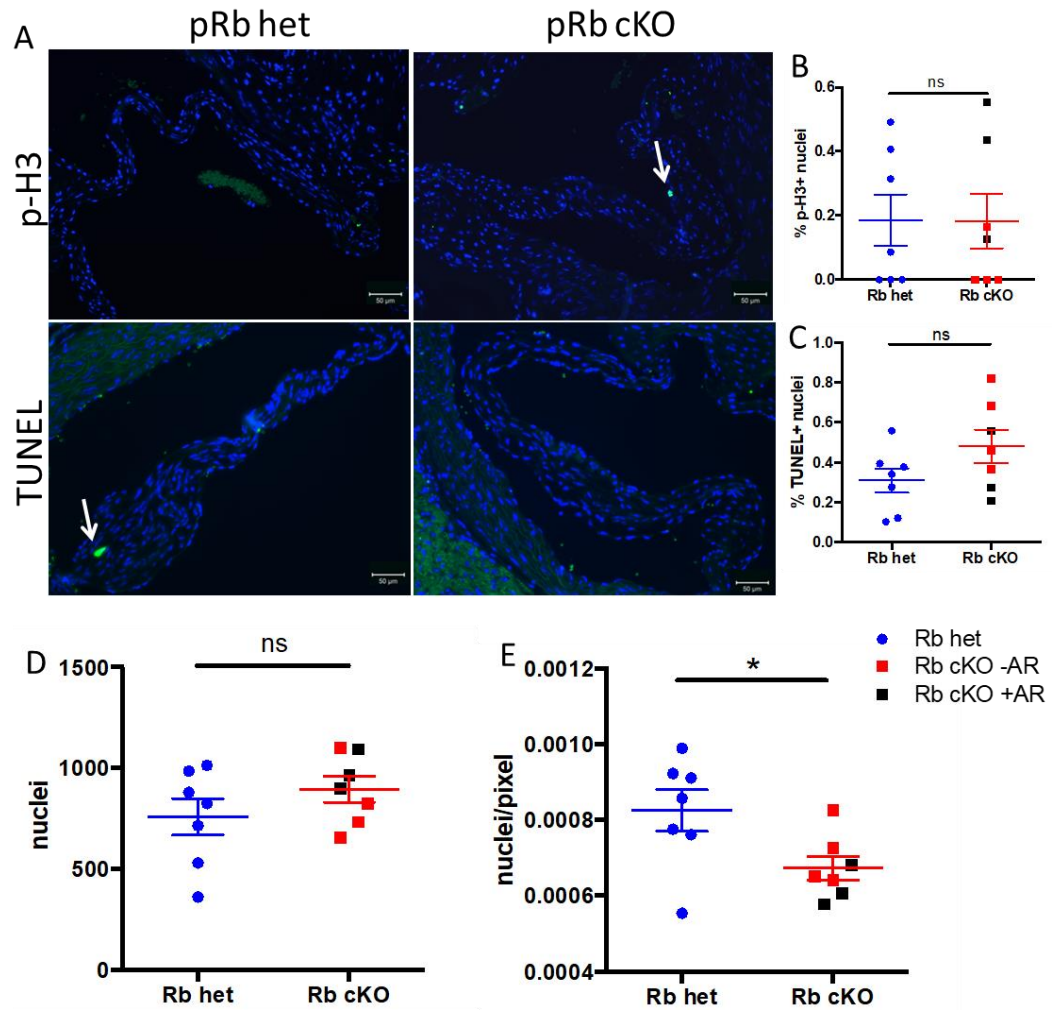


Figure 3.4: Aged pRb cKO aortic valves do not have increased proliferation or apoptosis.

(A) Representative staining for phospho histone H3 (p-H3; top panels, green) and TUNEL (bottom panels, green). Nuclei are stained blue with DAPI. (B) Proliferation, shown as p-H3 expression, was not significantly different between genotypes. (C) Apoptosis, as measure by TUNEL staining, was not significantly different between genotypes. (D) Absolute number of nuclei per valve were not significantly different, but cellular density (E), expressed as DAPI+ nuclei per pixel of aortic valve leaflet, was significantly lower in pRb cKO valves (Student's T-Test $P=0.03$). $n=7$ per genotype, mean \pm -SEM. This data was collected by Marina Freytsis.

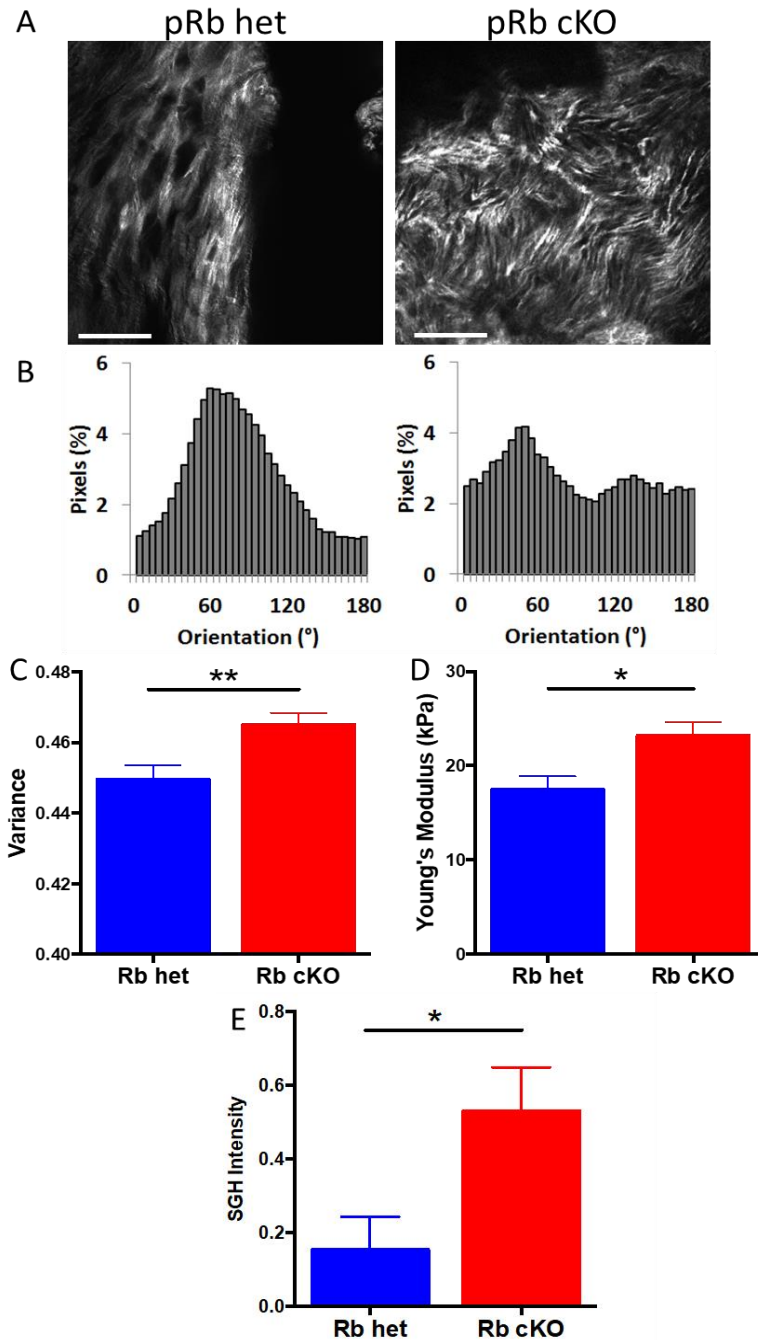


Figure 3.5: Structural analysis of aortic valve leaflets reveals differences in stiffness and collagen organization between pRb het and cKO mice.

(A) Representative second harmonic generation (SHG) images of mouse aortic valve leaflets. These images were used to calculate the variance of collagen fiber angle with representative fiber orientation data shown in (B) and total variance data shown in (C) (n=3; Student's T-test P=0.003). (D) Atomic force microscopy (AFM) was used to determine the Young's modulus of the aortic valve leaflets (n=4) pRb het and 6 pRb cKO; Student's T-test P=0.02). (E) Quantification of valve tissue fibrosis using SHG pixel intensity. Mean \pm SEM; Student T-test P-value = 0.03. Scale bar is 50 μ m.

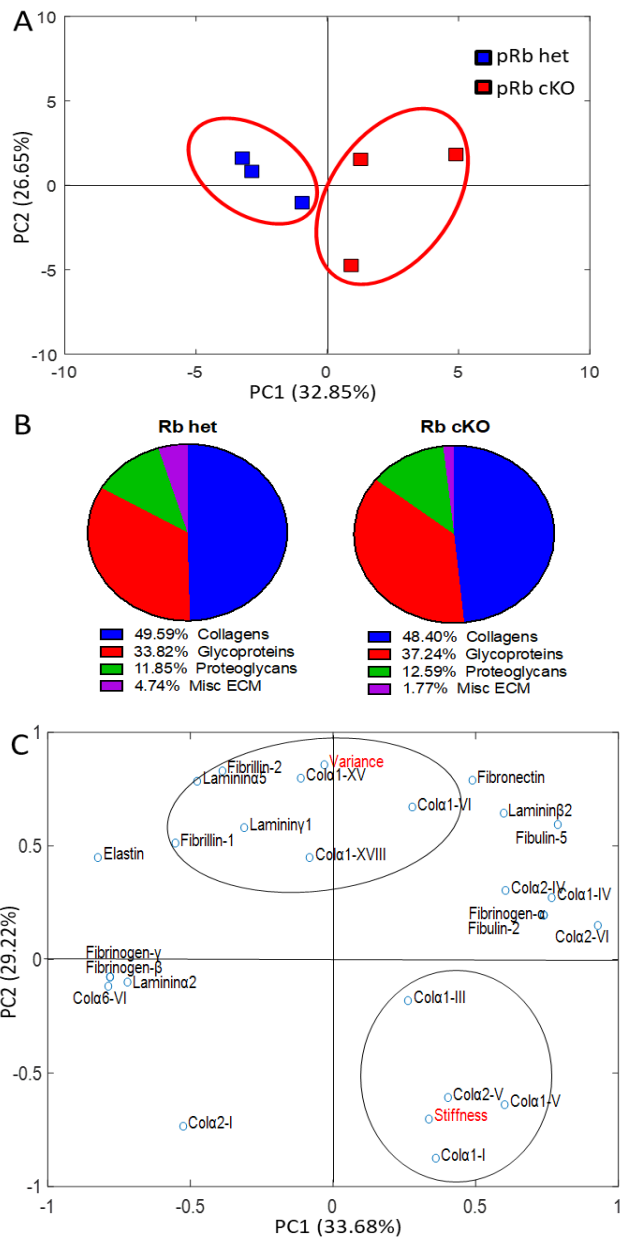


Figure 3.6: Analysis of the aortic valve proteome.

Data represented as protein spectral counts normalized to total ECM and cellular protein spectral counts in samples from LC/MS/MS analysis of trypsin-digested valve leaflet tissue. pRb het were compared to pRb cKO mice with AR and grouped using k-means clustering. (A) Principal Component Analysis (PCA) of all ECM and cellular protein counts that show substantial up (greater than 1.5 times) or down (less than 0.6) regulation of pRb cKO leaflets as compared to het controls, demonstrating clustering of both sample types. (B) ECM composition breakdown of aortic valve leaflets describes the relative percentages of the matrix proteins in pRb cKO leaflets compared to the pRb het mice. (C) Loading scores plotted for a PCA combining measured functional data (in red) with structural ECM proteins. Assuming 4 groups, k-means clustering was used to assess the relationships between the functional data and the proteomics output to look for ECM components that varied with the functional data outcomes. N=3 per genotype.

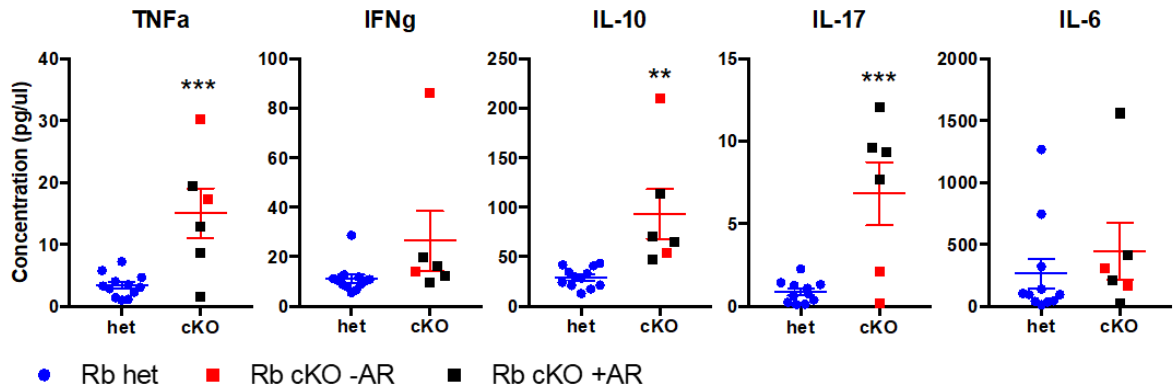


Figure 3.7: pRb loss in Tie2 lineage increases circulating cytokines in aged mice.

ELISA array was used to measure circulating cytokines in serum of pRb het and cKO mice. Serum was isolated following overnight fast by cardiac puncture immediately after sacrifice. Mean \pm SEM. P-value from Student's T-Test, corrected for multiple measures by Holm-Sidak method (** < 0.005; *** < 0.0005. N= 12 (het), 6 (cKO). This data was collected by Marina Freytsis.

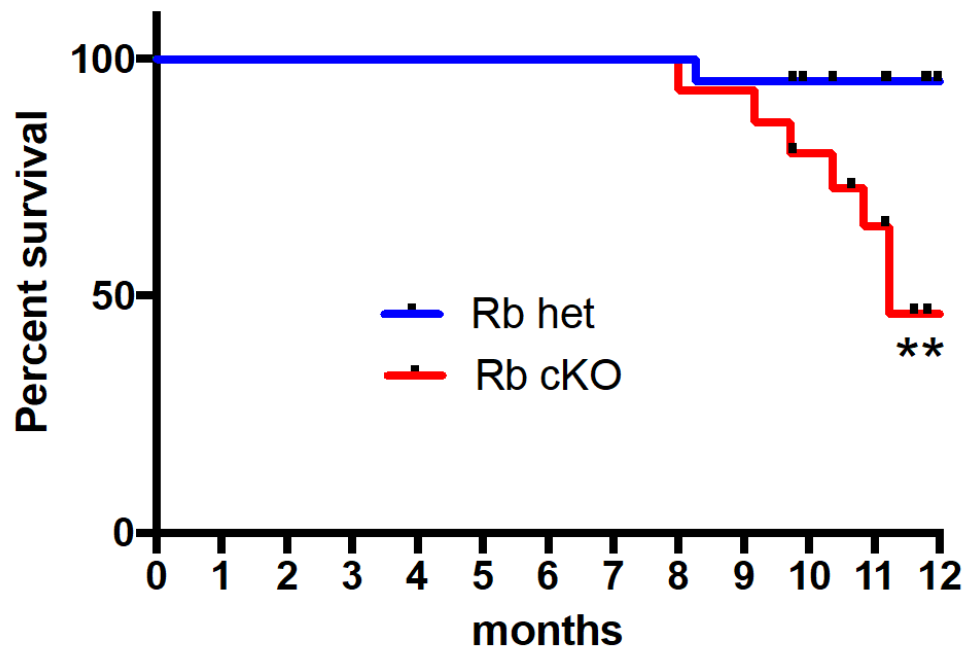


Figure 3.8: Survival of pRb het and cKO mice.

n= 21 (het) and 15 (cKO). ** Mantel-Cox P-value= 0.004. This data was collected by Marina Freytsis.

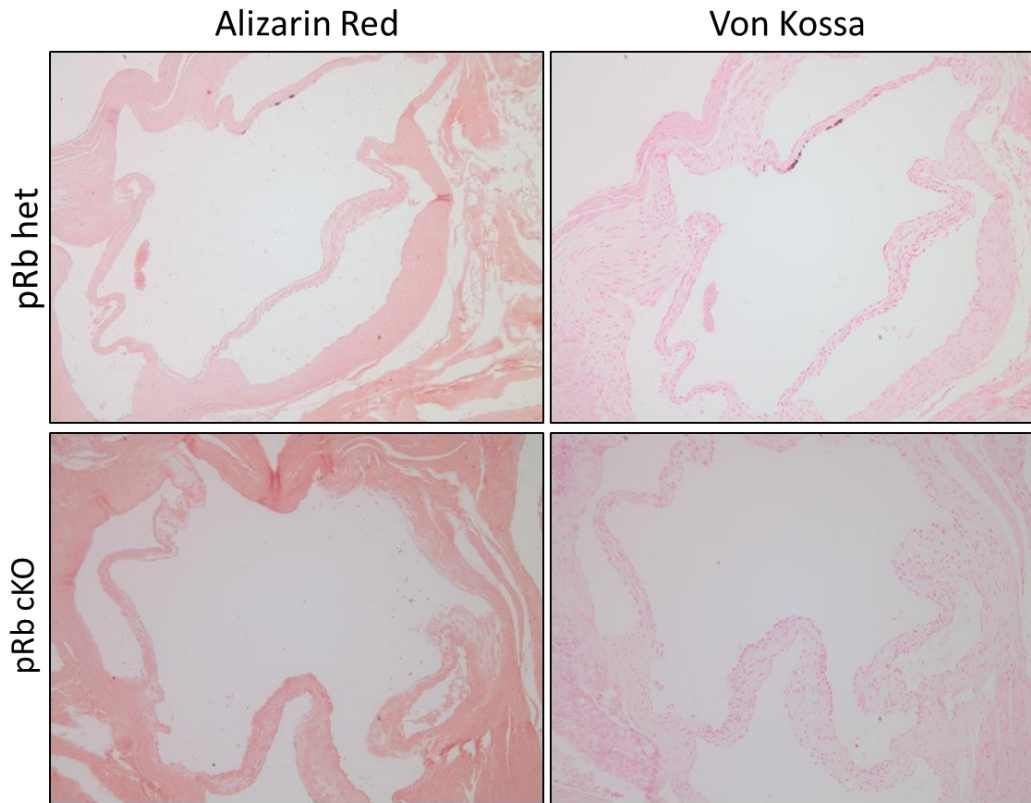


Figure 3.9: Histological analysis of aortic valve leaflet calcification in aged mice.

Representative images of (A) Alizarin Red and (B) Von Kossa stains demonstrate the lack of calcification in pRb het or cKO animals. This data was collected by Marina Freytsis.

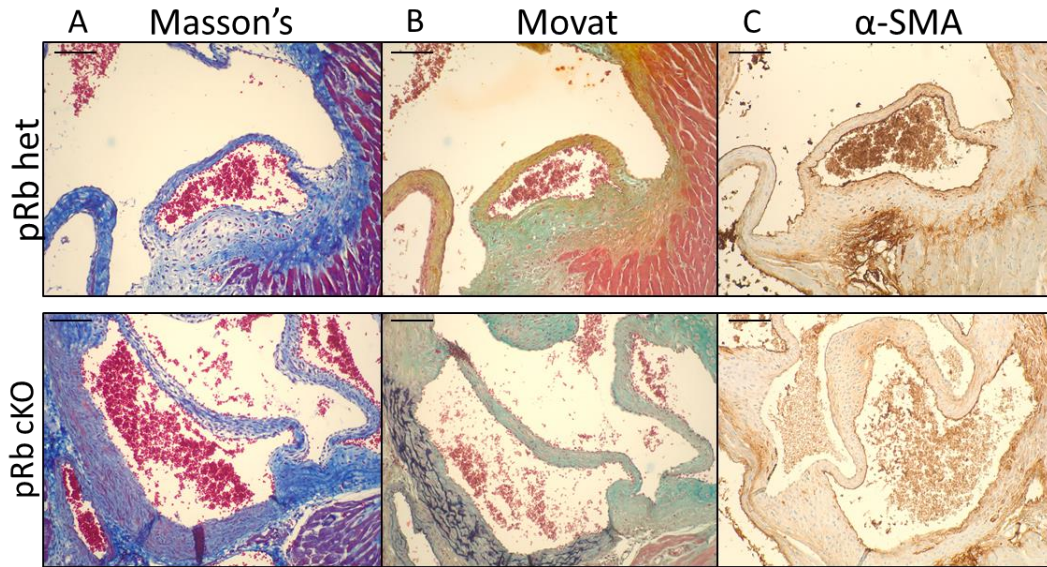


Figure 3.10: Histological analysis of aortic valve leaflets from 2-month-old mice.

(A) Masson's Trichrome, (B) Movat pentachrome, and (C) α -SMA Immunohistochemistry demonstrating the lack of distinct alteration in leaflets of 2 month old mice without pRb. Scale bar is 50 μ m. This data was collected by Marina Freytsis.

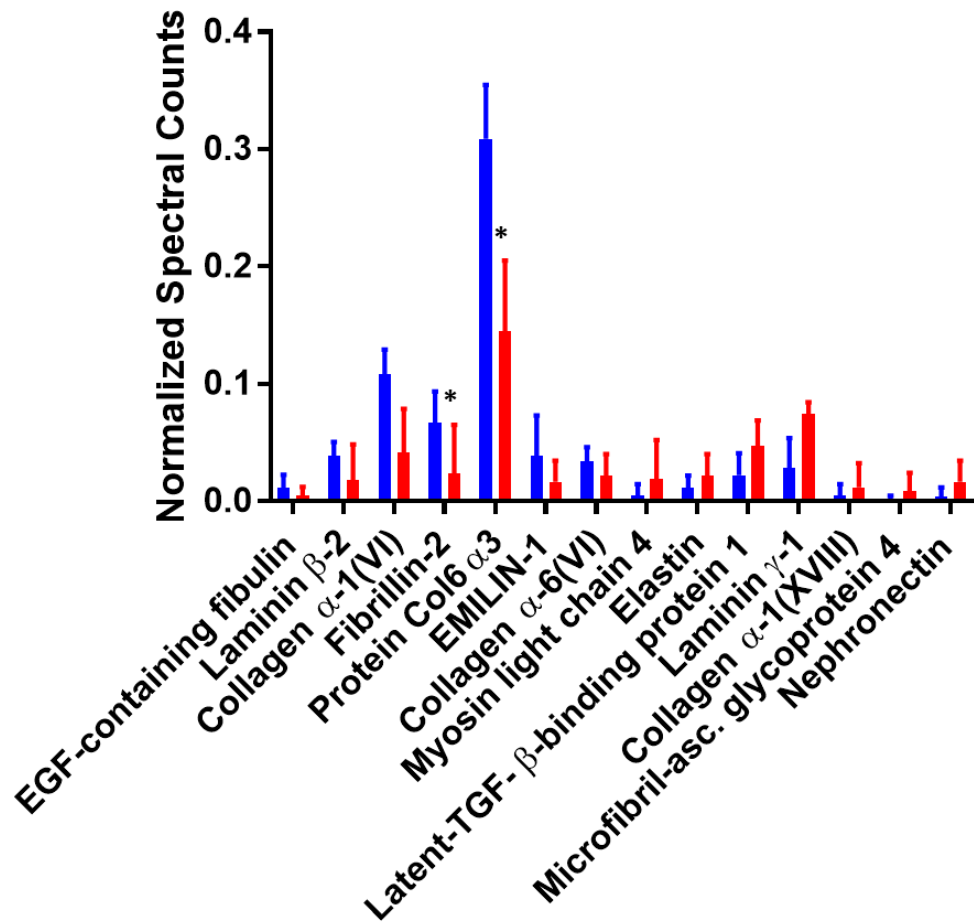


Figure 3.11: Differences in ECM protein components between pRb het and pRb cKO mice from proteomics analysis.

Normalized spectral counts of structural ECM proteins collected through LC-MS/MS analysis of pRb het (blue) and pRb cKO (red) aortic valve leaflets (n=3 for both conditions). Mean \pm Std Dev; P-value (*p<0.05) from student's t-test, corrected for multiple measures by Holm-Sidak method.

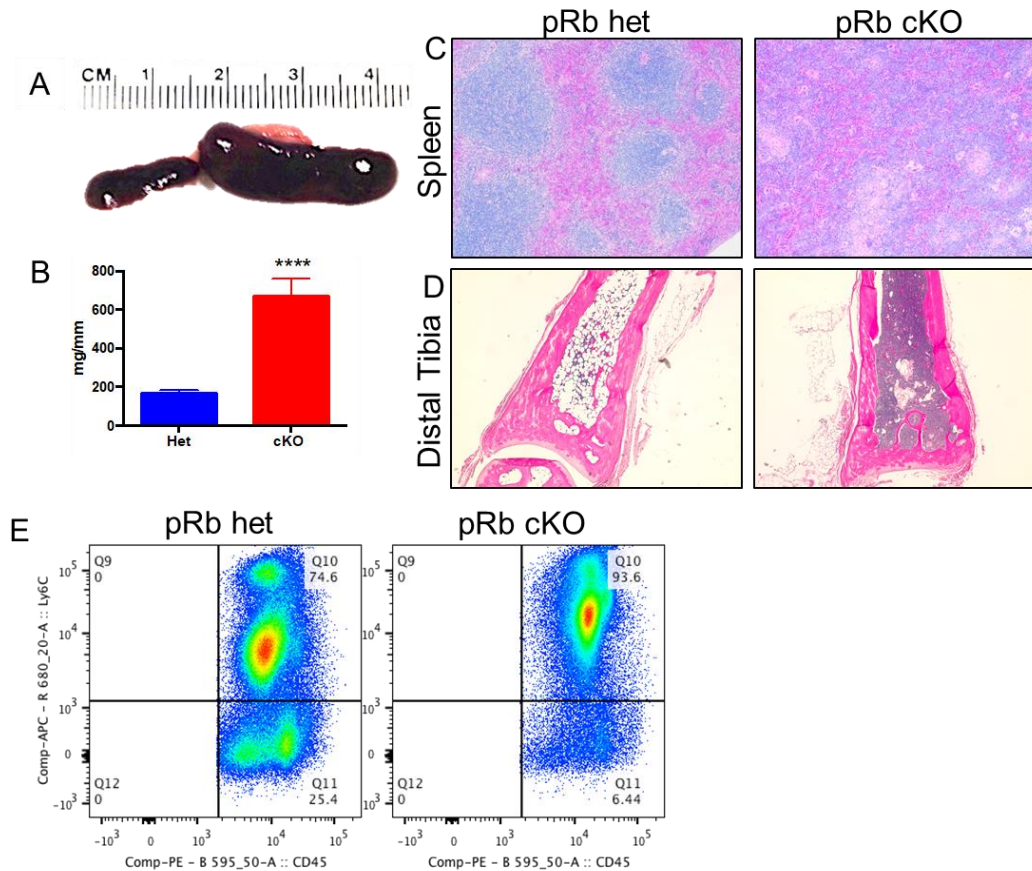


Figure 3.12: Splenomegaly and bone marrow alterations in pRb cKO mice.

(A) Representative photo of spleens harvested from aged pRb het and cKO mice. (B) Spleen weight normalized to tibia length, showing significantly splenomegaly in cKO mice (n=15 het, 11 cKO; Student's t-test $p < 0.0001$). (C) H&E staining of spleens from aged mice, showing increased white pulp in cKO samples as well as loss of typical nodular tissue structure, as in het spleens. (D) H&E staining of the distal end of the tibia of aged mice, showing increased BM cells and reduced adipocytes in cKO animals. (E) Representative FACS analysis of bone marrow, demonstrating increase of monocytes in cKO mice, as determined by cell surface expression Ly6C. This data was collected by Marina Freytsis.

Chapter 4. Non-destructive two-photon excited fluorescence imaging identifies early nodules in calcific aortic-valve disease

This chapter is taken directly from the article published in Nature Biomedical Engineering entitled “Non-destructive two-photon excited fluorescence imaging identifies early nodules in calcific aortic-valve disease”.¹⁵⁴ While I was directly involved in all experiments and data analysis, there were other authors involved in this published work. Their contributions are listed here.

Dr. Quinn performed data analysis and data interpretation, contributed to manuscript writing and final approval, and provided financial support (NIH-NIBIB Award # K99EB017723 and R00EB017723). Dr. Liu developed the computational model to extract quantitatively the component contributions from the images acquired at two emission bands and performed the corresponding calculations for both the human CAVD valves and the mouse model valves. Drs. Huggins and Hinds contributed to the data interpretation and final approval of the manuscript and, along with Dr. Black, contributed financially (NIH – NHLBI Award # R01HL114794). Dr. Evans and Mr. Osseiran performed CARS and TPEF imaging as well as data interpretation of human CAVD and rat bone samples. Dr. Huggins also provided the human CAVD valve samples. Dr. Georgakoudi directed the image acquisition and image analysis aspects of the study. Dr. Black and Dr. Georgakoudi contributed to the project conception and design, manuscript writing, data interpretation, and final approval of manuscript. Dr. Georgakoudi also contributed financially via a NIH-NIBIB award (Award # R01EB007542) and the American Cancer Society Research Scholar Grant RSG-09- 174-01-CCE.

Abstract

Calcifications occur during the development of healthy bone, and at the onset of calcific aortic-valve disease (CAVD) and many other pathologies. Although the mechanisms regulating early calcium deposition are not fully understood, they may provide targets for new treatments and for early interventions. Here, we show that two-photon excited fluorescence (TPEF) can provide quantitative and sensitive readouts of calcific nodule formation, in particular in the context of CAVD. Specifically, by means of the decomposition of TPEF spectral images from excised human CAVD valves and from rat bone prior to and following demineralization, as well as from calcific nodules formed within engineered gels, we identified an endogenous fluorophore that correlates with the level of mineralization in the samples. We then developed a ratiometric imaging approach that provides a quantitative readout of the presence of mineral deposits in early calcifications. TPEF should enable non-destructive, high-resolution imaging of three-dimensional tissue specimens for the assessment of the presence of calcification.

4.1 Introduction

Calcific aortic valve disease (CAVD) is characterized by a progressive thickening of the aortic valve leaflets and subsequent calcific nodule growth.² Currently, over 450,000 people in the United States, ages 65-74, have CAVD with aortic stenosis (AS);¹⁹⁵ many will require valve replacement surgery to prevent heart failure. Unfortunately, the primary method of diagnosis by echocardiography is only effective when AS is present in the valve,⁹¹ which is frequently at advanced stages of the disease.¹⁵ Given the significant mortality and morbidity associated with cardiovascular procedures in the elderly, the

development of new non-surgical treatment methods (e.g. pharmaceuticals) for CAVD is of critical importance; however a more thorough understanding of the mechanisms associated with CAVD development is required. Current studies on CAVD mechanisms are limited to observations of either end-stage diseased valves, genetic mouse models that may not accurately describe human disease pathology, or *in vitro* model systems that induce calcification in conditions that attempt to mimic the *in vivo* disease.^{15,196} Even in the latter two cases, where nodule formation and growth can be observed experimentally, quantification of calcification relies on destructive assays with finite spatial resolution that do not permit serial imaging of the same sample. The ability to study early calcifications with a non-destructive, high (micron-level) resolution method may help elucidate key mechanisms in the beginning stages of the disease, and factors influencing the propensity for disease progression. Such knowledge could have a significant impact on the development and assessment of critically needed interventions.

Current imaging methods used to study and diagnose CAVD include computed tomography (CT),⁷⁴ ultrasound,⁷⁵ magnetic resonance imaging (MRI),⁷⁶ molecular imaging with fluorochromes,⁷⁷ and second harmonic generation (SHG) imaging.⁷⁸⁻⁸⁰ The use of positron-emission tomography can provide information on relevant biological processes *in vivo*, such as measuring both inflammation and active calcification in CAVD patients as a predictor of disease progression,¹⁹⁷ through the use of radioisotopes. Recent studies have highlighted the use of ¹⁸F sodium fluoride (NaF)⁸⁵ as a means to quantify calcifications in the valves and predict areas of calcification that could later be identified with CT.⁸⁶ Despite such promising results, the resolution of this imaging approach is approximately 4-5 mm,¹⁹⁸ which limits its ability to detect the presence of micron scale nodules. Further, the uptake of the ¹⁸F NaF is reliant on actively calcifying cells, decreasing

its ability to assess less dynamic calcifications in the valve.⁸⁵ Additionally, while electron beam CT imaging can provide high resolution images (0.24-0.33 mm for bone in humans⁸²) with dual-scan contrast agents,⁸⁴ this modality still carries the risk of radiation exposure.⁸⁷ Molecular imaging in the near-infrared region (700 nm to 1000 nm) has also been utilized in *in vivo* models to measure inflammation and bone mineralization,⁸⁹ but always with the use of exogenous chromophores,^{77,88} adding complication and expense to the procedure. Non-destructive echocardiograms and MRI are limited by their spatial resolution (about 0.5 mm).^{77,81,82} SHG imaging, which collects signals emitted from non-centrosymmetric structures, such as collagen fibers, has been a powerful tool for characterizing collagen fiber alignment and structure in tissue engineered viable heart valves,⁷⁸ and *ex vivo* animal or human heart valve tissue.^{79,80} A recent study reported that CAVD was associated with layer-specific alterations in collagen architecture.⁶⁰ They used SHG imaging to quantify organizational changes of collagen fibers in human CAVD valves versus healthy ones, and found that the majority of changes in CAVD, including the fiber number, width, density and alignment, occurred in the layer of spongiosa, in contrast to relatively few changes in the layer of fibrosa.⁶⁰ However, using SHG imaging solely was not sufficient to provide a thorough understanding of mineralization, an important hallmark of CAVD. While many advances in imaging have been developed, all of these fail to fully describe microscopic morphological and functional changes within the valve tissue during CAVD development or to detect the early presence of calcification in a non-destructive manner. Interestingly, a recent study of human valve tissue found that many individuals classified as “healthy” can have microcalcifications (about 100nm to 5 μ m in size) present on their aortic valve leaflets; it was hypothesized that these tiny calcifications could develop into full aortic stenosis from CAVD and that understanding growth of these nodules may lead

to clearer understanding of CAVD progression.⁸³ The study, which relied on *ex vivo* scanning electron microscopy (SEM) and transmission electron microscopy (TEM) to gain the resolution necessary for imaging the microcalcifications, highlights the need for an imaging modality that does not damage the sample so that these nodules can be observed within the context of living tissues and intact extracellular matrix to elucidate potential mechanistic pathways of CAVD progression.

In contrast to the above-mentioned imaging modalities, nonlinear, multiphoton optical microscopy is a non-destructive, micron-scale resolution imaging approach with intrinsic depth sectioning that has been used extensively to image a variety of tissues.^{199,200} Specifically, two-photon excited fluorescence (TPEF) utilizes near-infrared light (NIR) to excite endogenous tissue fluorophores with emission in the visible range.²⁰⁰⁻²⁰² For example, TPEF has been used to quantify elastin and collagen in mouse valve tissue²⁰³ and used to assess the state of tissue engineered heart valves.²⁰⁴ Other studies have indicated the presence of single-photon excited autofluorescence from calcified tissue in the 515 nm emission regime, although this signal was never fully quantified.²⁰⁵ This suggests that TPEF could be used to image calcifications in a non-destructive manner within the context of fresh tissue samples. While this endogenous signal could also be exploited using standard fluorescence confocal imaging to acquire high 3D resolution assessments of calcifications, nonlinear microscopy enables such measurements over more extended depths and is less susceptible to photo-bleaching.^{206,207} However, further characterization of this signal is necessary since other molecules, such as collagen, also autofluoresce in this wavelength range.²⁰⁸ The distinction of mineralization associated fluorescence (MAF) from that of collagen is potentially easier using non-linear instead of linear interactions in two respects: a) for reasons that are not clearly understood the TPEF cross-section of

collagen is relatively low compared to its single-photon excited fluorescence cross-section,²⁰⁹ and b) SHG signal of collagen fibers can be easily collected at the same time as TPEF to identify their location with high specificity.²¹⁰ In fact, the acquisition of co-registered TPEF and SHG images for the study of calcifications in the context of extracellular matrix remodeling is one of the leading advantages of non-linear microscopic imaging compared to more established modalities such as CT and PET. In this study, we acquired TPEF spectral images from a range of calcified samples, including excised valves from human CAVD patients, rat bone fragments, and calcific nodules generated *in vitro* using polyacrylamide (PAAM) gels to identify endogenous TPEF readouts of calcification. Examination of spectral differences enabled us to identify two components, one attributed to collagen, the second to mineralization associated fluorescence (MAF). Further analysis, led to a simple, yet quantitative imaging scheme optimized to highlight regions rich in calcified deposits. Thus, our results indicate that TPEF imaging may provide a new tool to non-destructively quantify mineralization with high sensitivity and spatial resolution during CAVD progression.

4.2 Methods

All animal experiments were approved by the Institutional Animal Care and Use Committee at Tufts University and performed in agreement with Tufts University guidelines and the US Animal Welfare Act. Human samples of valves taken from patients undergoing replacement surgery for advanced CAVD were acquired under a protocol approved by the Tufts University School of Medicine Institutional Review Board (IRB number 10273). The tissues were considered discarded tissues (not removed for research purposes) and obtained only with patient consent.

4.2.1 Human CAVD Valve Samples

All male patients were used; ages ranged from 56-72 years. Within 24 hours of extraction, samples were frozen to -80°C until imaging. Four samples were acquired for this study.

4.2.2 Rat Valve Interstitial Cell (VIC) and Bone Isolation and Culture

Aortic valve leaflets were surgically removed from Sprague Dawley rats within 30 minutes of euthanasia and used to isolate VICs for the formation of calcified nodules *in vitro*. The valve leaflets were placed in a 12 well plate with standard culture media [Dublecco's Modified Eagle's Medium (DMEM; ThermoFisher Scientific, Waltham, MA [10566016]), 1% Fungizone (ThermoFisher Scientific, Waltham, MA, Antibiotic-Antimycotic [15240062]), and 10% fetal bovine serum (FBS, ThermoFisher Scientific, Waltham, MA [16000-044])]. Tissue samples were placed in an incubator at 37°C with 5% CO₂ for 10 days, with media changed every 2-3 days. Cells were allowed to migrate out of the tissue and adhere to the plate. VICs isolated in this manner were passaged and expanded in traditional culture flasks in standard culture medium. VICs that had been passaged 2-6 times were used for experimentation.

Male Sprague Dawley rat tibia bones were also isolated from sacrificed animals. Skin and muscle tissue were removed from the hind leg of three rats with a scalpel and 5 x 5 mm bone sections were removed from the tibia. Samples were washed and stored in 1X PBS for less than a week before imaging or fixation.

4.2.3 Polyacrylamide (PAAM) Gel Preparation

Before the creation of PAMM gels, 22 mm x 22 mm glass cover slips were activated to create binding sites as previously described.¹⁰¹ To increase hydrophilicity, cover slips were passed through an open flame and then covered with 0.1M NaOH (Millipore, Billerica, MA [SX0607H-3]). After the slips dried, 3-aminopropyltrimethoxy was smeared onto the cover slips and allowed to dry. Slips were then placed into 6-well plates and washed three times in diH₂O using an orbital shaker before being smeared with 0.5% glutaraldehyde (Sigma-Aldrich, St. Louis, MO [E6758]) and allowed to set for 30 minutes. After aspirating off the glutaraldehyde, the slips were again washed in diH₂O three times for five minutes. Activated cover slips were stored in diH₂O at 4°C until use.

To create the PAAM gels, acrylamide and bis- acrylamide were combined with 400 µg of rat tail collagen (ThermoFisher Scientific, Waltham, MA [A1048301]) and acrylic-acid-N-hydroxysuccinimide (NHS; Sigma-Aldrich, St. Louis, MO [A8060-1G]) ester (used to create covalent linkages between amine groups on the collagen and the PAAM gel). 1 N HCl was added to the solution to lower the pH to 6.8-6.9 before acrylamide to bis-acrylamide cross-linking was initiated using tetramethylethylenediamine (TEMED; Sigma-Aldrich, St. Louis, MO [411019]) and 10% ammonium persulfate (APS; Sigma-Aldrich, St. Louis, MO [A3678]).²¹¹ By altering the ratio of acrylamide to bis acrylamide, the PAAM gels were created to have a stiffness of 35 kPa to mimic CAVD mechanical physiology.⁴⁷ To create a stiffness of 35 kPa a solution containing 10% w/w acrylamide and 0.1% w/w bis acrylamide was used.

Activated cover slips were dried in a sterile cell culture hood and 80 μL of each gel solution was placed onto the cover slips. A non-activated cover slip was then placed directly onto the gel solution to reduce airflow and promote polymerization while creating an even gel surface. After 30-45 minutes, the top cover slip was removed from the polymerized gels using a razor blade. The gels were moved to sterile 6-well plates and washed three times for 5 minutes each with sterile 1X PBS (ThermoFisher Scientific, Waltham, MA [BP3994]).

Following creation of the PAAM gels, isolated VICs, were seeded at a density of 50,000 cells/gel and allowed to adhere to the gels for 24 hours before being moved to separate culture plates to avoid potential paracrine signaling from cells adhering to the tissue culture plastic during seeding. PAAM gels were dosed with 1.25 ng/mL TGF- β_1 (Peprotech, Rocky Hill, NJ [100-21]) for 24 hours in an incubator at 37°C with 5% CO₂. After 24 hours, media was replaced with the standard culture media described above and the PAAM gels were allowed to develop nodules for 14 days; media was changed every 2-3 days.

4.2.4 Demineralization with EDTA

Following TPEF imaging, samples fixed with 4% paraformaldehyde (in order to maintain collagen structure) and placed in 0.02% w/v ethylene-diamine-tetra-acetic acid (EDTA; Sigma-Aldrich, St. Louis, MO [E6758]) on an orbital shaker at room temperature for three weeks for demineralization, as previously described.²¹² The samples (4 human CAVD and 3 rat bone) were then washed with 1X PBS and imaged using both the Leica TCS SP2 and our custom laser scanning microscopes. Every attempt was made to acquire images from similar locations within the same samples before and after EDTA treatment.

4.2.5 Alizarin Red Staining

A 0.02% wt/v Alizarin Red (Sigma-Aldrich, St. Louis, MO [A5533]) solution (pH 4.2 with NaOH) was used to stain the PAAM gel nodules and human CAVD valve after TPEF imaging. After fixation with 4% w/v paraformaldehyde (Sigma-Aldrich, St. Louis, MO [158127]) for 10 minutes and washing with 1X PBS, the PAAM gels were placed in to the Alizarin Red solutions for 45 minutes. The same procedure was followed for the human sample, but with longer fixation (20 minutes) and staining (1.5 hours) times. All samples were then washed with diH₂O several times (until the wash water was clear at the end of the rinse; about 8-10x) before imaging using an Olympus FSX100 (Tokyo, Japan).

For comparison imaging of the same fields, small portions of each sample were fixed to a glass slide with a clear adhesive. The samples were first imaged using the Leica TCS SP2 microscope and the image locations were carefully noted. The slides were then stained with Alizarin Red as described above, and imaged a second time with the Olympus FSX100 with the same fields of view that were taken with the Leica microscope described below.

4.2.6 Intensity correlation analysis between TPEF and Alizarin Red staining images

In order to quantitatively compare the TPEF and Alizarin Red stained images, we assessed the correlation in the intensity of corresponding fields imaged by the two approaches. First, five-level Otsu intensity thresholding²¹³ was applied to both TPEF and Alizarin Red stained images corresponding to similar fields. The lowest level was designated as low intensity background noise, while regions assigned to the upper four quantized levels in TPEF or Alizarin stained images were used to define the tissue areas from which the mean

intensities were calculated. Four CAVD samples, four bone samples and five PAAM samples were used for this intensity correlation analysis, which was carried out in Excel.

4.2.7 Scanning Electron Microscope Imaging

Samples were prepared by gold sputter coating and imaged using a Carl Zeiss (Jena, Germany) EVO MA10 scanning electron microscope.

4.2.8 Micro-Structure Correlation Analysis between TPEF and SEM images

In order to assess if TPEF images enable characterization of similar micro-structure features as SEM images, we used a Fourier-based analysis approach we developed previously.²¹⁴⁻²¹⁷ Briefly, the image intensity patterns within the tissue regions, as determined by the Otsu intensity thresholding method described in the previous section, were cloned and randomly positioned in the image background to create a new image without distinct borders and only tissue patterns covering the entire field. Then, we acquired the power spectral density (PSD) of the two-dimensional Fourier transform of this image, which represents the level of autocorrelation of the intensity fluctuations within the image over a range of relevant spatial frequencies. This curve exhibited an inverse power law behavior, which was fit using an equation of the form $R(k) \sim k^{-\beta}$, where k is spatial frequency. The value of β depends on the texture features of the images and was determined for both TPEF and SEM images corresponding to the similar field of the same specimen from 4 CAVD samples and 4 bone samples. To image in the same region of each sample with both imaging modalities, small pieces of samples were glued to a glass slide so that each image location could be mapped during the TPEF imaging process and then found during SEM imaging. It was not possible to analyze PAAM gel samples in

the same way because the dehydration prior to SEM imaging significantly alters the PAAM gel nodule structures. The correlation analysis was done in Excel.

4.2.9 Fourier Transform Infrared (FT-IR) Spectroscopy

Three rat tibia bones and four CAVD valves were split into two pieces of roughly the same size. The two groups of samples were placed on an orbital shaker, at 4°C, either in the 0.02% EDTA solution used to reduce mineralization or in standard 1X PBS. After 3 weeks on the shaker, the samples were dried for 4 hours in a VirTis Genesis 25L Super XL Freeze-Dryer (SP Scientific, Stone Ridge, NY) and measured using FT-IR [JASCO FTIR 6200 spectrometer (JASCO, Tokyo, Japan) equipped with a MIRacle™ attenuated total reflection (ATR) Ge crystal cell in reflection mode]. Spectra were taken between 600 cm^{-1} and 3400 cm^{-1} with 1 cm^{-1} increments. A linear baseline was fit to the regions of the FTIR spectra devoid of significant absorbance peaks (1800 cm^{-1} to 2500 cm^{-1}) and subtracted from the spectra. The spectra were then normalized using the total area under the curve. The CAVD and EDTA CAVD spectra were then shifted up the y axis to more clearly show the two sample types. The standard error of the mean was also calculated and plotted for each group.

4.2.10 Two-Photon Excited Fluorescence Imaging

TPEF spectral images were taken on a Leica TCS SP2 (Wetzlar, Germany) confocal microscope equipped with a Ti:sapphire laser (Spectra Physics, Mountain View, CA) and a dry Leica 20x/0.7 NA objective. To obtain spectral emission data, the laser was tuned to either 800 nm or 860 nm and images were collected between 400 nm and 700 nm in 40 equal increments (7.2 nm steps), each with a bandwidth of 20 nm. Using the Rayleigh

criterion, the computed lateral resolution for this objective is 0.697 μm and the axial resolution is 3.265 μm . 3D image renderings were created using ImageJ (NIH, Bethesda, MA).

Fluorescence spectra from all tissues were decomposed in two components using a blind spectral unmixing algorithm. This data set included 6 spectra from human CAVD valves, 8 spectra from EDTA treated human CAVD valves, 7 spectra from rat bone, 5 spectra from EDTA treated rat bone, and 3 spectra from nodules grown on 35 kPa PAAM gels. Specifically, non-negative matrix factorization was performed through an alternating least squares algorithm using a modification of the `nnmf.m` function in MATLAB. A two component model was used with random initial guesses for component concentrations. To avoid convergence to a local minimum, factorization of the component spectra and their relative concentrations in each tissue was performed 1000 times and the solution providing the smallest norm of the residual was selected. A two component model was selected based on its ability to describe 99.46% of the variance in emission spectra data. The relative contribution of component 2 was calculated for each spectrum and the calculated average for each sample specimen was used for statistical analysis (4 CAVD valves, 3 rat bones, and 3 PAAM gel nodules).

The rat bone and the human CAVD valve samples were further imaged using a custom-built laser scanning multiphoton microscope, which enabled simultaneous image acquisition by three non-descanned detectors equipped with filters at 400 nm \pm 10 nm (ET400/20X), 460 \pm 20 nm (HQ460/40m-2p), and 525 \pm 25 nm (ET525/50M-2P). TPEF and SHG images were acquired at 800nm excitation. A Leica 20x/0.7 NA objective was used for image acquisition of four human CAVD samples and three rat bone samples. For each

sample, both before and after treatment with EDTA, 3 images were taken from three distinct regions on the sample. The calculated MAF values were averaged to give a single measurement for each biological replicate (4 for the human CAVD valve and 3 for the rat bone samples) for statistical analysis.

4.2.11 Image-Based Quantitative Assessment of Mineralization Associated Fluorescence (MAF)

Based on the spectra of the collagen and the MAF components extracted from the spectral decomposition described above, we developed a simple method to enable us to quantitatively extract the relative MAF contribution based on image acquisition at two distinct spectral bands: 460 nm \pm 20 nm and 525 nm \pm 25 nm. The TPEF image intensity at these two bandwidths can be expressed as:

$$I_{460} = \xi_{460} (\alpha_{460} C_1 + \chi \beta_{460} C_2) \quad (1)$$

$$I_{525} = \xi_{525} (\alpha_{525} C_1 + \chi \beta_{525} C_2) \quad (2)$$

where ξ_{460} and ξ_{525} are the quantum efficiencies of the detectors at 460 nm and 525 nm, and C_1 and C_2 are the concentration of component 1 and 2, respectively. α_{460} and α_{525} are the fluorescence yields of component 1 at 460 nm and 525 nm respectively, and β_{460} and β_{525} are those corresponding to component 2. χ is a factor accounting for the difference of fluorescence efficiency of the two components. According to equations (1) and (2), the formalism for the concentration ratio of these two components is as follows:

$$C = \frac{\xi\alpha_{460} - I\alpha_{525}}{\chi(I\beta_{525} - \xi\beta_{460})} \quad (3)$$

where $C = C_2 / C_1$, $\xi = \xi_{460} / \xi_{525}$, and $I = I_{460} / I_{525}$. We obtain the α_{460} , α_{525} , β_{460} and β_{525} from the spectra of component 1 and 2, which are 0.3394, 0.3590, 0.0812 and 0.3614 respectively. The ξ value of 0.8573 is acquired based on TPEF images acquired from extracted pure rat tail collagen fibers using the same excitation/emission data acquisition settings, and the χ value of 0.1520 is acquired by the raw intensity images of the experimental samples. Since the I values corresponding to each sample are readily accessible, we obtain the C values specific to each sample, and, finally, the relative contribution of the MAF component, C_2 as $C_2 / (C_1 + C_2)$, which in this form is a value that always varies between 0 and 1.

4.2.12 MAF TPEF Intensity Analysis

To assess the TPEF MAF intensity (800 nm excitation) relative to that of collagen, we extracted the TPEF intensity ratio within the mineralization-rich and collagen-rich regions from each field of all the CAVD and bone samples we examined. To identify the collagen-rich regions, we manually selected regions with strong SHG signal, such as the blue areas within the RGB images shown in **Figure 4.5** A, C). We then calculated the mean TPEF intensity within this region, which we attributed to collagen. To identify the mineralization-rich regions, we first acquired the MAF ratio map for each field, identified pixels with the top 10% MAF ratio values, and calculated the mean MAF TPEF intensity within each such region. Given the spectral characteristics of collagen and MAF TPEF relative to the bandpass or our 525 nm emission filter, we estimated the expected

collagen and MAF TPEF intensity based on the full spectral emission of each component. In this manner, we acquired for each field an intensity ratio representing the MAF TPEF intensity relative to that of collagen. As we can't really measure the concentration of the molecule that leads to MAF, we cannot really acquire a more quantitative metric of MAF TPEF efficiency. Four fields from each of the four CAVD and three bone samples were imaged before and after EDTA treatment.

4.2.13 Imaging of Genetic Mouse Model

Three male apolipoprotein E knockout mouse hearts (ApoE^{-/-}, age 10 months, on a C57BL/6 background, Jackson Laboratory, Bar Harbor, ME) and three, 2 month old female wild type (WT) mouse hearts (C57BL/6 mice, Jackson Laboratory, Bar Harbor, ME) were donated by the Jaffe Lab at Tufts Medical Center. The hearts were stored in 1X PBS during transport, valve isolation and imaging, which occurred within 24 hours from mouse sacrifice. The ApoE^{-/-} mice were fed a high fat diet for 9 weeks before being sacrificed. This model has been previously shown to induce heart valve calcification as measured by von Kossa²¹⁸ and alkaline phosphatase-positive staining.²¹⁹ TPEF image stacks were acquired at 460 ± 20 nm and 525 ± 25 nm from two distinct regions of the aortic valve of each mouse using the Leica TCS SP2 microscope at an excitation of 800 nm. Each image stack consisted of 5 to 34 optical sections acquired with a step size of 5 μ m. The relative MAF contribution for each section was calculated and then averaged from all sections of a given image stack. MAF values for each of the six valves (three ApoE^{-/-} and three WT valves) were calculated by averaging measurements from both Z stacks.

4.2.14 Coherent Anti-Stokes Raman Scattering (CARS) Microscopy with TPEF Imaging

CARS microscopy was performed using a dual output femtosecond pulsed laser system (Spectra-Physics Insight DeepSee, Santa Clara, CA, USA) and a customized confocal microscope (Olympus FV1000, Center Valley, PA, USA) using a 1.20 NA 60X water immersion objective (Olympus UPLSAPO 60XW, Center Valley, PA, USA). The fixed 1040 nm laser output was used as the Stokes beam while the widely tuneable output was set to 758 nm and used as the pump beam in order to probe the 3570 cm^{-1} vibrational band of OH⁻ in hydroxyapatite. A coherent anti-Stokes signal was thus generated at 596 nm, detected in the epi-direction using a photomultiplier tube (Hamamatsu H7422P-50, Hamamatsu City, Japan). A 750 nm shortpass filter was used to remove any residual excitation light (Chroma ET750SP-2P8, Bellows Falls, VT, USA), followed by a bandpass filter from 590 to 650 nm (Chroma HQ620/60M, Bellows Falls, VT, USA) To control laser power, a half-wave plate and a Glan-Laser polarizer were placed in front of each laser output port, and total incident power at the sample was maintained below 50 mW for all experimental conditions.

TPEF microscopy was performed using the same system as described above for CARS imaging. In this scenario however, the TPEF signal was generated by setting the tuneable output to 800 nm, where the fluorescence signals were collected in the epi-direction using a pair of thermoelectrically cooled photomultiplier tubes (Hamamatsu H7422P-40 and H7422P-50, Hamamatsu City, Japan). The fluorescence signal was first filtered using a 750 nm shortpass filter to remove any residual excitation light (Chroma ET750sp-2p8, Bellows Falls, VT, USA). The signal was then incident on a 480 nm dichroic mirror, where reflected shorter wavelengths were filtered once more through a bandpass filter (Chroma HQ475/60M, Bellows Falls, VT, USA) such that the effective fluorescence detection

ranged from 445 to 480 nm; transmitted longer wavelengths were filtered through a separate bandpass filter (Chroma HQ525/50M, Bellows Falls, VT, USA) for detection ranging from 500 to 550 nm.

4.2.15 Time Lapse Imaging and MAF Quantification

PAAM gels were created, as described above on the activated glass of a 35 mm MatTek glass bottom dish (Ashland, MA). VICs were seeded at 100,000 cells/mm² and dosed with 1.25 ng/mL TGF- β_1 for 24 hours in an incubator at 37°C with 5% CO₂ before being cultured for 4 additional days in normal culture medium. The dish was then moved to the Leica TCS SP2 microscope and incubated using similar culture conditions for the duration of the experiment. TPEF images were acquired at 460 \pm 20 nm and 525 \pm 25 nm emission channels using 800 nm excitation and a 20x/0.7 NA air objective. A Z stack of 19 images, using the same imaging parameters for the duration of the experiment, was taken for a single field of view every 8 hours for 120 hours.

Following acquisition, images from each channel were processed to extract the related MAF contribution images. For each time point, the MAF image stacks were integrated along the Z direction to create a 2D projection. The Template Matching and Slice Alignment ImageJ plugin was then used to align the 2D projections so that individual nodules could be tracked over time. For each time point, the 2D projection was then analyzed to examine individual nodules. Regions of interest (ROIs) were selected around mineralized nodules and a second integration along the x direction was performed for each time point. This led to a 1D intensity plot for each nodule that was used to calculate the full width at half maximum (FWHM), which related to the size of the nodules, and the

integral, which represented the volumetric MAF nodule intensity. Four nodules, or ROIs, were analyzed for this study.

4.2.16 Statistical Analysis

One-way ANOVA with post hoc Tukey HSD tests were used to evaluate the differences between the human CAVD valves and rat bone before and after EDTA treatment using either the ratio of component 1 to component 2 (**Figure 4.4**) or the calculated MAF (**Figure 4.5**). Normality of the sample set was confirmed using the Shapiro-Wilk test, and equal variance was confirmed using the Brown-Forsythe test. A two-tailed, paired student T-test, confirmed with the same normality and variance testing, was used to determine significant differences between the ApoE^{-/-} and wild type mice. No animal randomization was used for this study and the study was not blinded. As this type of optical characterization has not been done before, we could not perform rigorous a-priori calculations to estimate the sample size needed to detect significant differences. A two-tailed, paired student T-test was used to compare the mean MAF to collagen TPEF intensity ratio for CAVD and bone samples before and after EDTA treatment. Normality (Shapiro-Wilk) and equal variance (Brown-Forsythe) were also confirmed prior to implementing the statistical analysis. EDTA treatment experiments were done one time with replicates of four and three for the human CAVD valves and rat bones, respectively. The time lapse experiment was performed on one PAAM gel.

4.2.17 Data Availability

The authors declare that all data supporting the findings of this study are available within the paper and its supplementary information, source data for the figures in this study are available from the authors upon request.

4.2.18 Code Availability

Custom Matlab code used to calculate the relative MAF contributions is available for download through the following link: github.com/liuzhiyi16/MAF-code.

4.3 Results

4.3.1 Comparison of Imaging Techniques for Calcification

To assess the potential of detecting mineralized deposits using TPEF, we compared multiphoton images with histological images of the commonly utilized calcification stain Alizarin Red. Representative endogenous TPEF images acquired with 800nm excitation and at 525 ± 25 nm emission from human CAVD patient valves, from rat tibia bone samples, and from calcified nodules grown *in vitro* using PAAM-collagen gels were compared with corresponding images acquired from the same samples after Alizarin Red staining (**Figure 4.1**). The endogenous TPEF signal patterns are generally consistent with those of the stain, suggesting that mineralized deposits exhibit enhanced TPEF in this spectral region. The similarities observed are remarkable given that the Alizarin Red stained images are transmission images, relying on absorption contrast from the entire tissue sample, while the TPEF images represent either single optical sections or 3D projections of a 315 μm thick TPEF stack for the human CAVD nodule, a 110 μm thick TPEF

stack of rat bone, or a 265 μm thick TPEF stack of the PAAM gel nodule. The intensities of TPEF and Alizarin Red images of CAVD, bone, and PAAM gel nodules are significantly correlated, further supporting that the enhanced TPEF signal in these images is associated with the levels of mineralization (**Figure 4.9 A**, $R^2=0.7334$, $p=0.0002$).

To illustrate the capability of TPEF imaging capability to highlight fine structural mineralization features, such as ridge edges and surface roughness, CAVD valves, rat bone tibia, and PAAM gel nodules were imaged using SEM and TPEF. Structural similarities are observed between representative SEM images and TPEF optical sections and 3D projections. The human CAVD nodule, rat bone, and PAAM gel nodule 3D reconstructions are composed of images from a 160 μm thick, a 115 μm thick, and a 147 μm thick TPEF stack, respectively (**Figure 4.2**). The sections demonstrate that the TPEF signal is not limited to superficial features. Thus, unlike SEM imaging, TPEF images provide structural details of the mineralized deposits throughout their imaged volume. Further, texture analysis of the SEM and TPEF images taken from CAVD valves and bone reveals that the organization features of the two types of images are strongly correlated (**Figure 4.9 B**; $R^2=0.8157$, $p=0.002$). Thus, these comparisons indicate that endogenous TPEF images provide useful information regarding mineralization content and organization that are typically acquired using invasive microscopic imaging procedures.

4.3.2 Spectral Analysis of Mineralized Tissue

Collagen is abundant in valve tissue and is the primary component of the fibrosa layer of the aortic valve, the region of the leaflet where the majority of calcifications begin.² Collagen fibers are strong sources of a nonlinear (two-photon) scattering process,

referred to as second harmonic generation (SHG), because of their non-centrosymmetric structure²²⁰. SHG has been used extensively to assess collagen fiber organization and structure.²²¹⁻²²⁴ Additionally, TPEF and SHG imaging can be performed simultaneously, and their combined use could enable assessment of calcific nodule formation in the context of collagen organization and remodeling. However, collagen fibers are also natural TPEF emitters, with the signal emanating primarily from collagen crosslinks.^{225,226} Thus, in order to exploit TPEF as a sensitive biomarker of calcification, it is important to identify differences in its TPEF emission from that of collagen.

To gather further evidence that the TPEF signal detected in the 500-550 nm region originates primarily from calcified deposits within the samples, we acquired and compared images from CAVD and rat tibia bone tissue samples prior to and following treatment with EDTA, a known Ca^{2+} chelator.²¹² Overlaid with the TPEF images (red) are corresponding SHG images (blue) acquired from the same field of view to demonstrate that the TPEF signal is not simply collagen autofluorescence (**Figure 4.3**). Specifically, we observe that the pattern of the bright TPEF signal is quite distinct from the SHG producing collagen fibers, and the prevalence of the TPEF signal decreases upon EDTA treatment for both the CAVD and bone samples. We do not detect any SHG signal in the PAAM gels, since they consist of disorganized, solubilized collagen.

FT-IR spectra of bone and CAVD samples confirm the reduction of mineralization with EDTA treatment (**Figure 4.3 F**). Specifically, a decrease in the phosphate peak (1000 cm^{-1} – 1200 cm^{-1}), which is an important hydroxyapatite component,²²⁷ is seen with EDTA treatment in both sample types.

Previously, endogenous autofluorescence in the 450-700 nm range has been described as deriving from lipids,^{205,228} elastin,^{205,228} collagen,²²⁸ and ceroid deposits²²⁹ found in atherosclerotic plaques. In fact, single photon autofluorescence of calcifications has been reported in plaques collected using 515 nm and 610 nm barrier filters,²⁰⁵ which is consistent with our mineralization associated TPEF signal. However, endogenous TPEF emission excited at 800 nm and detected at 520 ± 40 nm from calcified plaques has been attributed, at least partly, to lipids whose presence was confirmed by Coherent Anti-Stokes Raman Scattering (CARS) imaging.²³⁰ Careful inspection of the images of that study indicates that there was additional autofluorescence signal surrounding the CARS-identified lipid, which could have been originating from within the mineralized deposit, but this possibility was not explored.

To better understand and characterize the origins of the observed TPEF signal in our samples, we collected full spectral images; i.e. we gathered forty TPEF images, each representing the signal over a 20 nm bandwidth in the 400 to 700 nm range and centered approximately 7 nm apart from each other (**Figure 4.10**). Thus, each pixel contained a full TPEF emission spectrum. The mean spectra collected from each sample type are shown in **Figure 4.4 A-C**, along with the corresponding fits to these spectra resulting from non-negative linear factorization analysis, which revealed major contributions from two components (**Figure 4.4 D**). The two-component model provided a good fit to the spectra of each sample group (human CAVD valves: $R^2=0.997 \pm 0.006$, rat bone specimens: $R^2=0.973 \pm 0.034$, and PAAM gel specimens: $R^2=0.990 \pm 0.005$). The first component has an emission peak at approximately 480 nm, which is consistent with collagen TPEF excited at 800 nm.²²⁵ The second component is associated with the mineralized deposits, as indicated by: a) the significant decrease in the relative contribution of this component

upon EDTA treatment with the CAVD and tibia bone specimens ($p=0.088$ for CAVD and $p<0.001$ for tibia bone samples; **Figure 4.4 E**), and b) its almost exclusive ($93 \pm 6\%$) contribution to the TPEF emission collected from the nodules grown on PAAM gels, which aren't expected to have any collagen-associated TPEF.¹⁰¹ Similar spectral components were produced at 860 nm excitation (**Figure 4.11**). Notably, the spectra for the MAF component are nearly identical for both excitation wavelengths, with a peak at approximately 530 nm. On the other hand, the peak for the collagen-associated TPEF component had a slight red shift, which has been reported previously for collagen emission.²²⁵ Additionally, the detected 525 nm signal attributed to mineral deposits is highly unlikely to emanate from lipids. End-stage human CAVD and tibia bone samples are heavily calcified and are expected to have minimal lipid content.²³¹ While the identity of the MAF component is not clearly recognized, the fact that its emission spectrum does not shift as a function of excitation wavelength, suggests that it is a single biochemical moiety. Since, we do not have a means of establishing the concentration of the MAF component, it is not possible to quantify its TPEF cross-section. However, we have made quantitative comparisons between the collagen and mineralization rich regions and have found the mean MAF TPEF intensity per pixel to be 2.5 ± 0.6 times higher the mean collagen TPEF intensity at 800 nm excitation. While the relative MAF TPEF intensity tended to be lower for the EDTA treated samples, there were no statistically significant differences in the mean MAF to collagen TPEF intensity ratio for any of the sample groups examined.

4.3.3 Using a Ratiometric Approach to Enable Rapid MAF Imaging

While performing a full spectral analysis on a range of samples that are expected to have varying contributions from a set of fluorophores is an important first step in determining the spectral emission properties of these components, it is extremely time-consuming; this would be especially challenging in an *in vivo* setting and would require specialized instrumentation that could hinder the usability of this technique. However, quantifying the emission spectra of the two components and exploiting their differences, enabled us to develop a simple yet quantitative approach for extracting the relative contribution of the MAF component, relying on only two images (see Methods). These TPEF images are acquired at two distinct emission bands centered at 460 and 525 nm (shown as a highlighted regions on top of the two component spectra of **Figure 4.4 D**). Representative overlays from TPEF images in these two ranges along with the SHG image from the same field of view are shown in **Figure 4.5 A** and **C** from CAVD samples prior to and following EDTA treatment. Images from the individual channels can be found in **Figure 4.12**. Corresponding processed images highlighting the extracted relative contribution of the MAF component (**Figure 4.5 B** and **D**) demonstrate the ability of this approach to enhance visualization of mineral deposits. In addition to such qualitative visual assessments, we can extract quantitative, significant differences in the levels of the MAF upon EDTA treatment for both CAVD ($p=0.002$) and bone tissue samples ($p=0.045$; **Figure 4.5 E**).

4.3.4 CARS Imaging Confirms Hydroxyapatite Origins of MAF Signal

As a further confirmation that the observed fluorescence is associated with mineralization, CARS imaging was performed on both CAVD valves and rat bone to look

for evidence of hydroxyapatite formation. CARS is a parametric nonlinear optical imaging technique where the contrast arises from the intrinsic vibrational modes of a given chemical group.²³² The 3570 cm⁻¹ vibrational band of OH⁻ in hydroxyapatite was imaged using CARS microscopy and overlaid with the calculated MAF images for both the valve and bone samples (**Figure 4.6**), showing a strong correlation between MAF and CARS samples. The strong overlap between the CARS and MAF signals indicates the MAF signal is likely emanating from hydroxyapatite in the valve.

4.3.5 Applying the Ratiometric Method to ApoE^{-/-} Mouse Model

To demonstrate that the optical imaging approach we developed to detect and monitor valve mineralization in a quantitative and sensitive manner is applicable to a wide range of samples that are relevant to tissue calcification, we used the same image acquisition and analysis protocol to assess the relative MAF contributions within freshly excised valves acquired either from WT or ApoE^{-/-} mice, which were fed a high fat diet to increase valve mineralization. This mouse model is the most frequently used animal model of CAVD disease and has played an important role in identifying mechanisms relevant to CAVD development and treatment.^{68,218} While there are limitations to using a genetic mouse model to study CAVD, several studies have shown that they are an adequate platform for studying the underlying osteogenic pathways associated with CAVD, even if they have fallen short in the transition to clinical trials.⁹ In particular, ApoE^{-/-} mice exhibit upregulation of many osteogenic markers and form lesions that express bone makers such as ALP, Runx2, and osteocalcin.³⁶ In our study, we simply exploit the previously documented formation of mineral deposits in the valves of these mice as an example of preclinical studies in which our approach can be used to detect the level of mineralization.

Spectral image analysis confirmed that the collagen and MAF components described the TPEF emission recorded from these samples well ($R^2=0.976 \pm 0.005$ for the ApoE^{-/-} mouse valves and $R^2=0.981 \pm 0.010$ for WT mouse valves). Another fluorescent component may be present in these tissues in the 650-700 nm region, but that is clearly distinct from the signals we detect in the 460 and 525 nm regions of the spectrum which are fit with high accuracy by the two-component model (**Figure 4.11**). Thus, TPEF images were taken using the same protocol as the one used for our previous samples. Overlays of the collected images are shown with the corresponding processed images that highlight the relative prevalence of the MAF component in the different tissue samples in **Figure 4.7**. Images used for the overlays are included in **Figure 4.13**. An increase in the MAF component is immediately evident within the ApoE^{-/-} mouse valves upon visual inspection of the images (Figure 7 B, D). Quantitative evaluation of these images reveals indeed a significant increase in the relative MAF contribution from the WT to the ApoE^{-/-} mice ($p=0.0525$; **Figure 4.7 E**).

4.3.6 Time Lapse Imaging Tracks Nodule Growth

To demonstrate the sensitivity and potential of the described MAF-based method to track mineral deposition from its onset, we monitored the growth of calcific nodules in a PAAM gel system seeded with valve interstitial cells (VICs) over 5 days. The PAAM gel was imaged every 8 hours for 120 hours and the growth of individual nodules was assessed. For each time point, the 460 and 525 nm TPEF images were processed to generate a stack of images of the relative MAF contribution. This stack was then integrated in the Z direction to yield a 2D projection at each time point (**Figure 4.8A** shows the projection at the start of the experiment). Images from each time point are stacked and regions of interest (ROIs) are

cropped from the entire image stack. Four ROIs from this projected image were analyzed for nodule growth as shown in **Figure 4.8** A and B and representative images of a single ROI in **Figure 4.14** A (see **Figure 4.14** B for additional detail of the method). A representative image of the summed slices of one ROI is shown in **Figure 4.8** C, while **Figure 4.8** D shows the respective line plots of the intensities of **Figure 4.8** C. The line plots were generated by integrating each ROI along the x direction; we generated one dimensional plots characterizing the nodule MAF intensity at each time point. The FWHM of these plots are associated with the cross-sectional width of the nodules (**Figure 4.8** E) and their integral represents the nodule MAF volumetric intensity (**Figure 4.8** F), which is a measure of its overall mineral content. The calculated FWHM and the nodule volumetric intensity show nodule growth for all ROIs, except for ROI 3 which displays a decrease in volumetric intensity, though still an increase in nodule width.

Interestingly, nodule growth was not uniform with ROI 3 decreasing in size overall (based on the nodule volumetric intensity plot) even as it grew outwards along the PAAM gel (as shown by an increase in the FWHM). This exemplifies how nodule development may not be uniform within mineralized tissue and that active changes in calcification could add another layer of consideration to CAVD diagnosis. While the overall mineral content increased over the experimental time course, the MAF-based imaging method was able to detect small changes in the manner in which individual nodules grew. Understanding the dynamic changes that occur at calcification foci could be a key step in understanding the development of mineralization or their response to treatment.²³³

4.4 Discussion

The lack of clinical success in non-surgical treatment of CAVD highlights the need for improved understanding of the underlying disease mechanisms. Recent literature suggests that optical methods in particular could have a large impact on preclinical research.⁷⁷ Such methods offer the potential for imaging at high, micron-level resolution that may enable identification of CAVD lesions at the early stages of the disease, when therapy may be more effective. In this study, we show that calcified nodules exhibit endogenous fluorescence signatures that can be exploited by TPEF imaging to enable non-destructive visualization of calcifications with micron-level resolution. Specifically, we find that endogenous TPEF with a peak emission at 530 nm is detected from mineral-rich specimen regions when excited at 800 or 860 nm. This emission is distinct from that of collagen crosslink TPEF, which, as expected, has a peak that becomes red-shifted as the excitation wavelength increases.²³⁴

The characterization of the detailed spectral emission profile of the MAF and its comparison to the emission from collagen fibers, which are typically present in mineralized samples, enabled us to develop a simple, and fast, yet robust approach to quantify the relative MAF contributions within a specimen. This method relies on the collection of two images centered at 460 and 525 nm upon excitation at 800 nm, which can be combined to provide a quantitative readout of the relative prevalence of the MAF. We validate the sensitivity of this approach by demonstrating that we detect a decrease in the relative MAF levels upon EDTA treatment of both human CAVD and rat tibia bone samples. We further confirm the biochemical origins of MAF using FT-IR and co-registered CARS and TPEF measurements. To demonstrate that this simple imaging protocol is

relevant to the analysis of a broad range of specimens, we apply it to the characterization of valve samples from wild type and ApoE^{-/-} mice, a widely used animal model for CAVD studies.²³⁵ Analysis of these samples further validates the sensitivity of this optical imaging scheme to the enhanced levels of mineral deposits that are formed in the knockout mice valves.²³⁵ While there are clearly limitations in terms of the clinical relevance of the ApoE^{-/-} mouse model of CAVD, our approach should be applicable and potentially very useful in assessing CAVD progression in emerging pre-clinical disease models. These include *in vitro* models of calcification²³⁶ and new genetic mouse models of CAVD.²³⁷ In addition to potential *in vivo* imaging strategies in animal models, we showed that MAF quantification can be used to track nodule growth, non-invasively, over time in *in vitro* conditions. Nodules smaller than 10 microns in their cross-sectional width were imaged and showed growth overtime which we tracked in all three spatial dimensions over time.

Given the micron-level resolution of TPEF imaging, the approach we describe bears great promise as a tool that may be used to detect and monitor dynamically the development of mineralized deposits from a very early stage using pre-clinical CAVD models. Such advances are expected to have a significant impact on our understanding of the disease and the development of more effective treatments. While advances in micro-CT/PET imaging methods have led to better predictive capabilities of CAVD progression in patients, more could be learned with a better understanding of ECM changes and mineralization at a cellular level within the valve. NIR imaging techniques that use dyes to visualize the development of mineralization are able to detect small ossification before even high resolution micro-CT, which provides an even better understanding of calcification development.²³⁸ Direct clinical translation of TPEF imaging to monitor CAVD

may be initially complicated by the need to perform such measurements through millimeter sized endoscopes. Such multiphoton endoscopes are not immediately available for intravascular use, but we expect that continuous advances in probe development and human in vivo TPEF measurements will ultimately make such measurements a real possibility.^{239,240} Currently, the 2014 American Heart Association/American College of Cardiology guidelines recommend the use of cardiac catheterization to measure blood hemodynamics for patients that cannot be diagnosed through echocardiographic imaging²⁴¹; the use of an imaging probe either in place of or in conjunction with a catheter is therefore a reasonable goal. Additionally, because of the increased resolution capabilities of capturing MAF over current imaging modalities, high risk patients such as those with a bicuspid aortic valve,²⁴² could be imaged to look for potential CAVD mechanisms early in the disease process. MAF could also be used with CT/PET imaging methods on patients testing positive for CAVD to look for smaller nodules within the context of ECM changes. The development of single-photon excitation-based measurements of MAF are also possible, because in most cases the single and two-photon excited fluorescence emission spectra of molecules are highly overlapping. A number of optical probes have been used for intravascular imaging using different modalities, such as optical coherence tomography (OCT), photoacoustics, and fluorescence, alone or in combination.²⁴³⁻²⁴⁵ In addition, confocal microendoscopy probes as small as 0.6 mm in diameter have already been developed.²⁴⁶ Thus, an endogenous fluorescence-based high-resolution imaging system developed and optimized for mineral deposition detection in human valves is technologically highly feasible. Of course, thorough studies that establish the sensitivity and specificity of this approach will be needed. Finally, we should note that such a probe may also be more broadly applicable for the detection, characterization or

monitoring of other conditions affected by the presence of calcifications, including atherosclerotic plaques²⁴⁷ and breast cancer.²⁴⁸ While direct translation of this approach to the clinic will require addressing significant challenges associated with miniature probe development and minimizing the optical impact of blood, its relevance to more fundamental studies with *in vitro* and *ex vivo* tissues to improve our understanding of the disease is immediate.

4.5 Conclusion

The use of NIR light and non-linear microscopy has already proven to be useful as a non-destructive tool for biological imaging. Using the endogenous fluorescence of mineralization, we developed our MAF method for quantifying calcification *ex vivo* in both soft and hard tissues, as well as presenting it as a method for monitoring *in vitro* experiments over long time scales. On its own or combined with other optical methods, such as SHG, this new tool has the potential to shed light on understanding the changes that happen to cells and the ECM in soft tissue diseases like CAVD. Additionally, this imaging method is not limited to studying the aortic valve, and could readily be applied to any system, healthy or disease, that involves mineralization.

4.6 Figures

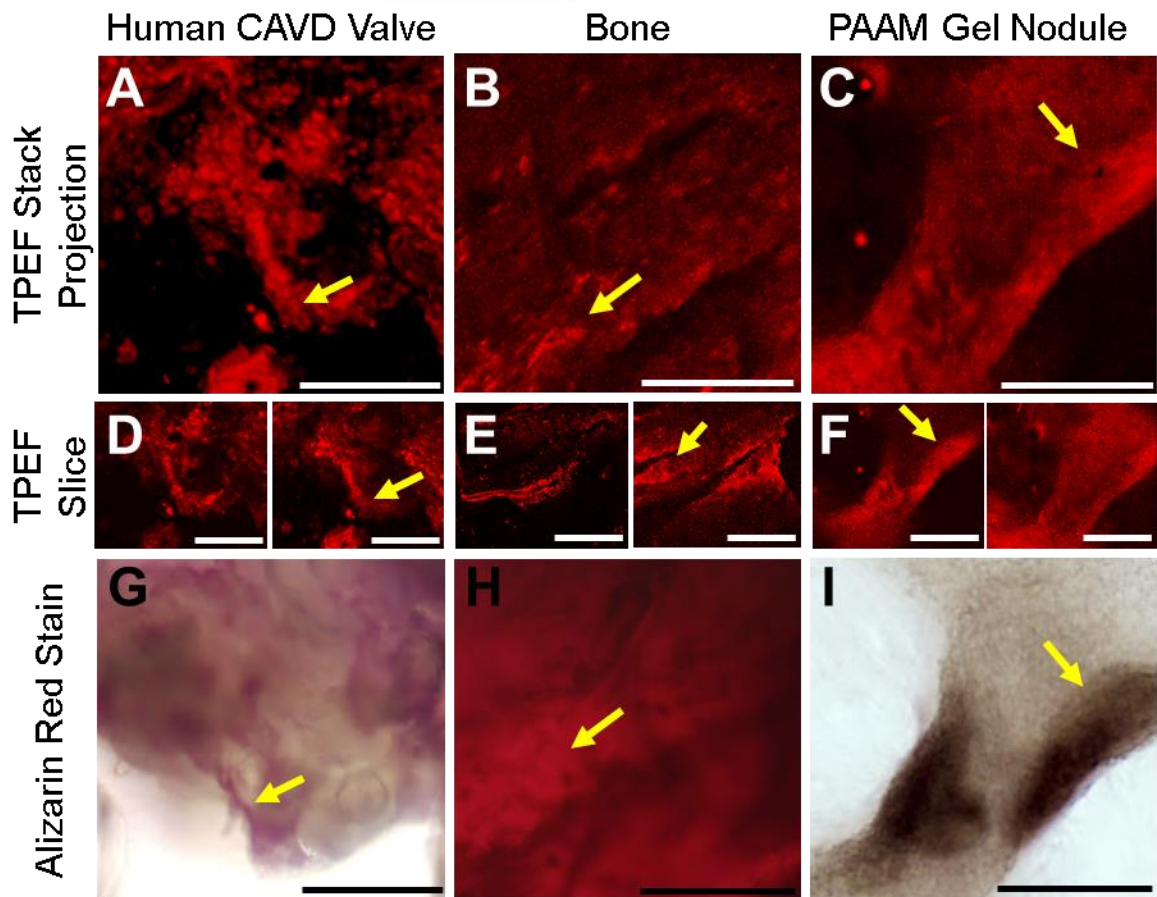


Figure 4.1: Visual analysis of TPEF images compared to Alizarin Red staining of a human CAVD nodule, a rat bone, and a PAAM gel grown nodule.

Two-photon excited autofluorescence and Alizarin Red staining for mineralization within CAVD human valves (A, D, G), rat bone (B, E, H) and nodules grown on PAAM gels seeded with rat VICs (C, F, I). Projections of TPEF image volumes (A, B, C) were created by averaging individual depth-resolved optical sections (D, E, F). The endogenous TPEF patterns are consistent with the spatial distribution of subsequent Alizarin Red staining of the same region (G, H, I). Yellow arrows show features similar between the TPEF and Alizarin Red images. Scale bars are 50 μm .

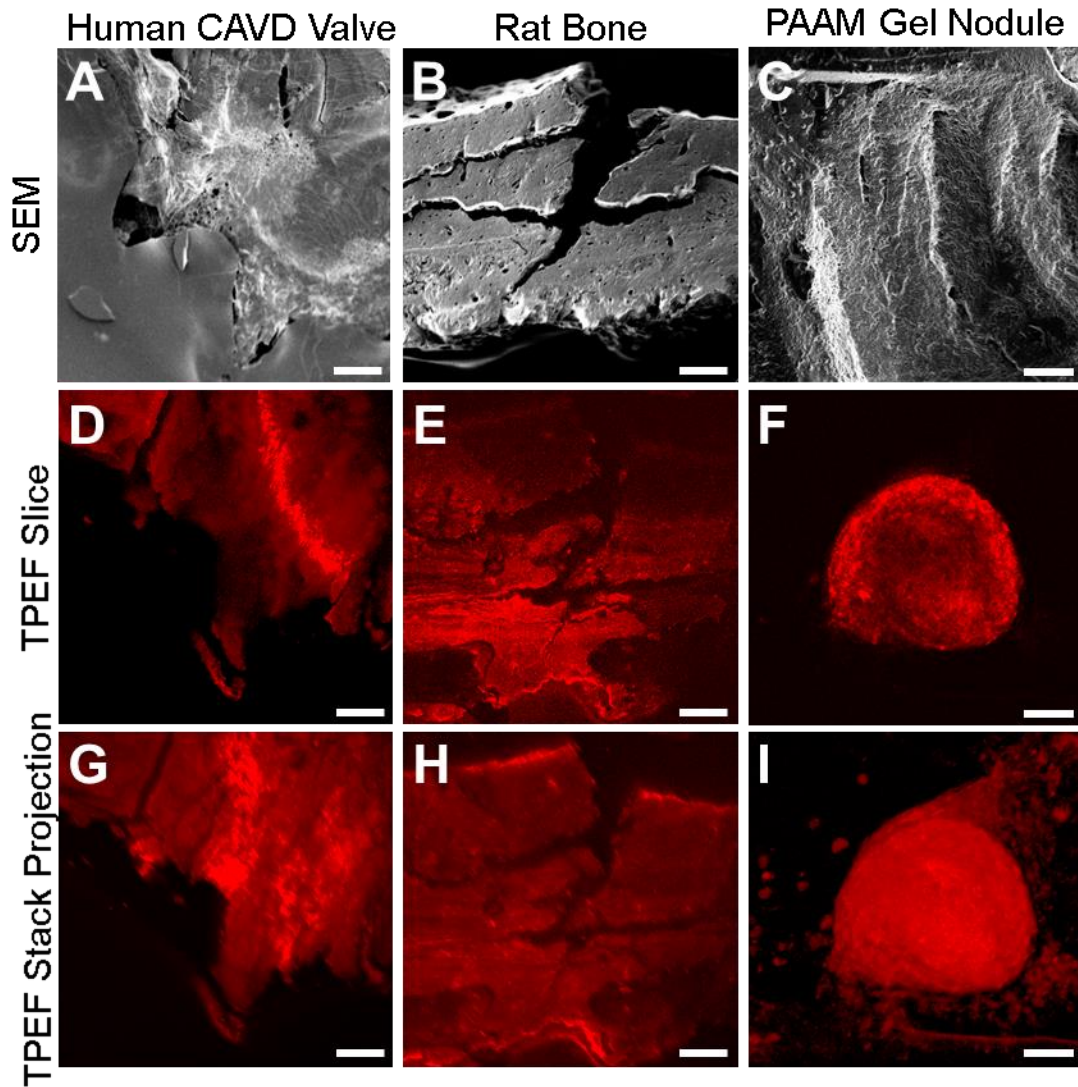


Figure 4.2: Representative images of human CAVD nodules, rat bone samples, and PAAM gel nodules taken using SEM and TPEF.

SEM images of nodules from a human CAVD valve (A), rat bone (B) and PAAM gels (C) show the topography of the different types of calcific nodules. Representative TPEF slices (D, E, F) and intensity projections of the image volumes (G, H, I) also demonstrate the ability to identify textural patterns between calcified samples. Scale bars are 100 μm .

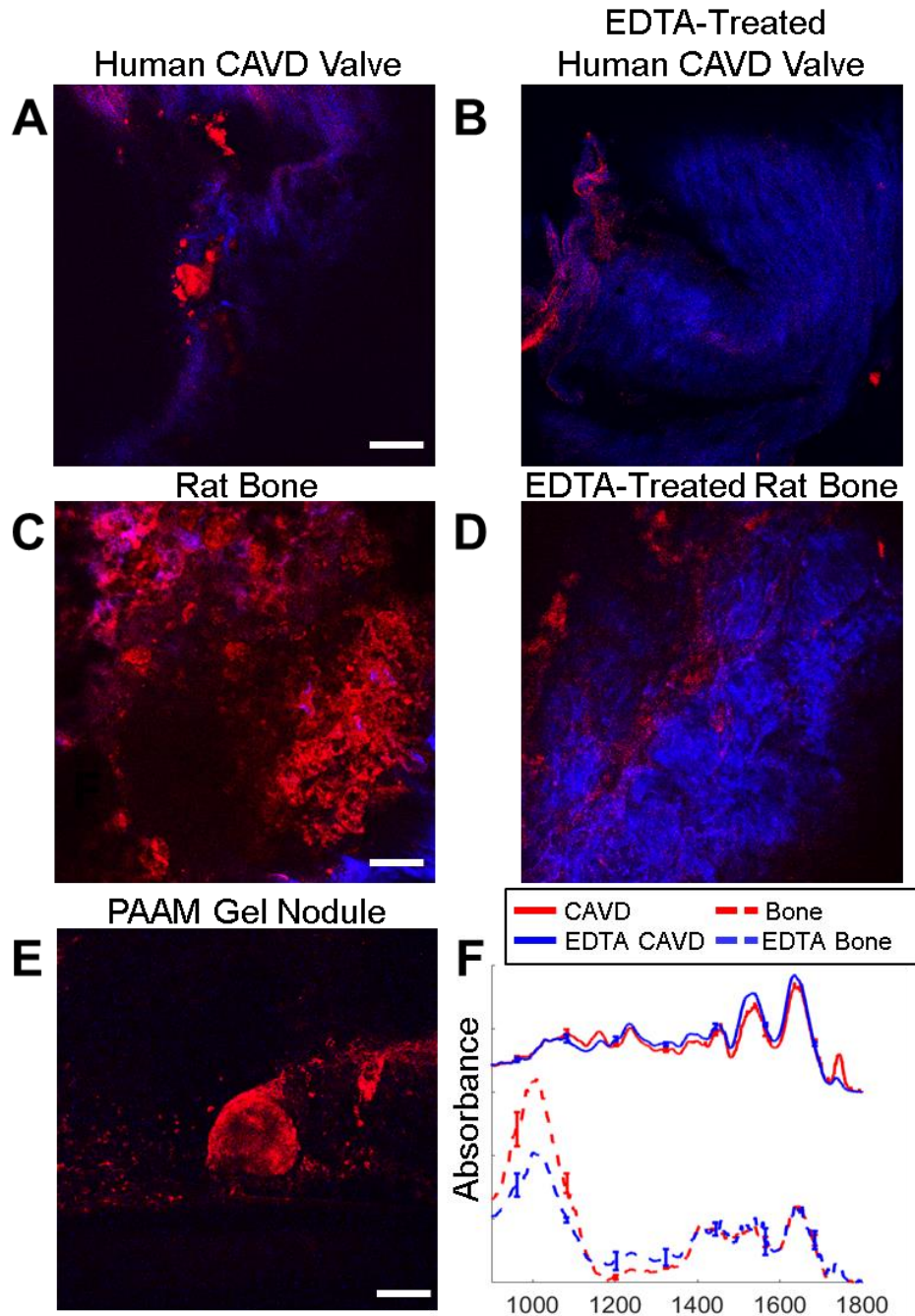


Figure 4.3: Effect of EDTA treatment on endogenous TPEF.

Representative optical sections of a human CAVD valve before (A) and after (B) EDTA treatment, as well as rat tibia bone before (C) and after (D) EDTA treatment suggest that 525nm TPEF emission (red) is associated with mineralization. Collagen SHG (blue) is not attenuated by EDTA treatment. No collagen SHG is observed in PAAM gels (E). FT-IR spectra taken before and after EDTA treatment for the CAVD (F) and bone (G) samples show changes in absorbance with loss of mineralization. Scale bars are 100 μm. Error bars show standard error of mean.

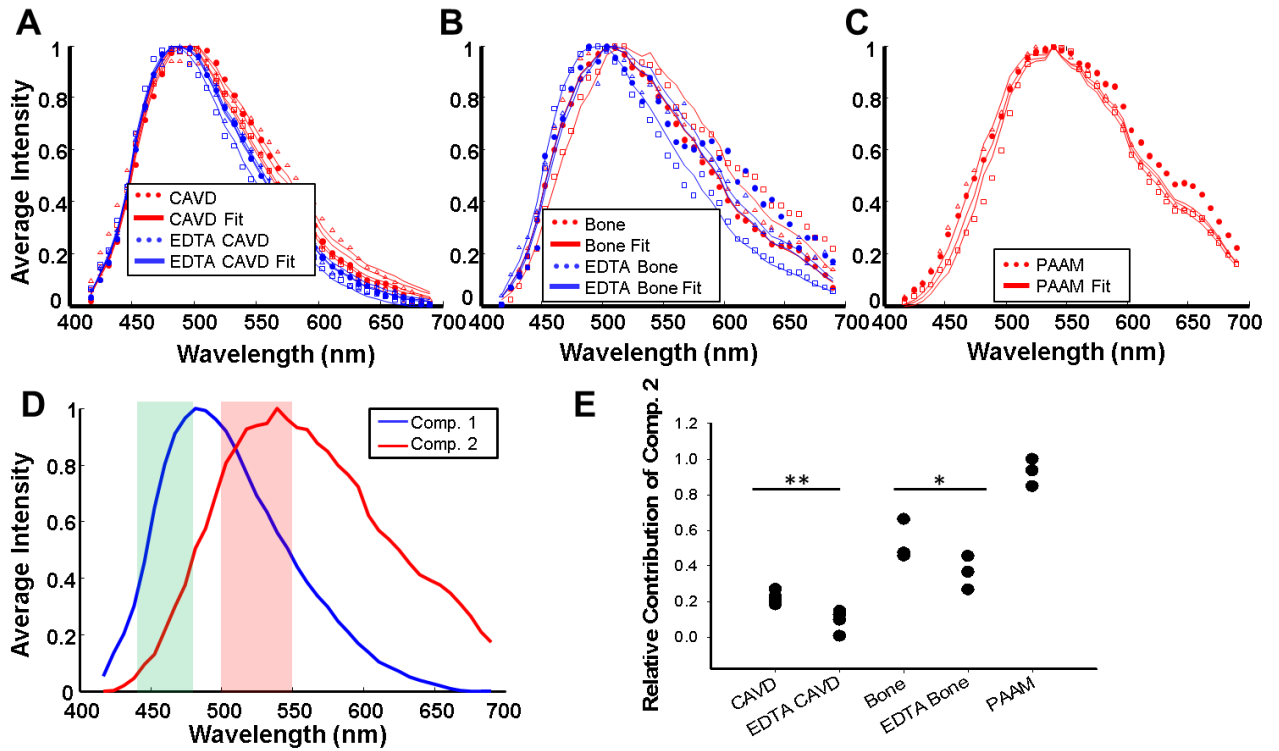


Figure 4.4: Analysis of TPEF emission spectra reveals emission spectrum of mineralization associated fluorescence.

Representative TPEF emission spectra of (A) human CAVD valves before and after EDTA treatment, (B) rat bone before and after EDTA treatment, and (C) nodules grown on PAAM gels indicate a blue shift with EDTA treatment. For A-C, representative data sets are delineated using either triangles, squares, or dots; representative fits are shown using a solid line. Spectral unmixing through non-negative matrix factorization indicated two spectral components (D), which provided a good fit to the data in A-C. Shaded regions in (D) represent the emission filter bands employed in TPEF imaging. (E) The relative contribution of component 2 derived from spectral unmixing and associated with mineralization is reduced upon EDTA treatment (* $P=0.088$, ** $P<0.001$ based on ANOVA and post-hoc Tukey test). Averaged spectra are shown from 4 CAVD valves, 4 CAVD EDTA valves, 3 bone samples, 3 EDTA bone samples, and 3 PAAM gel nodules.

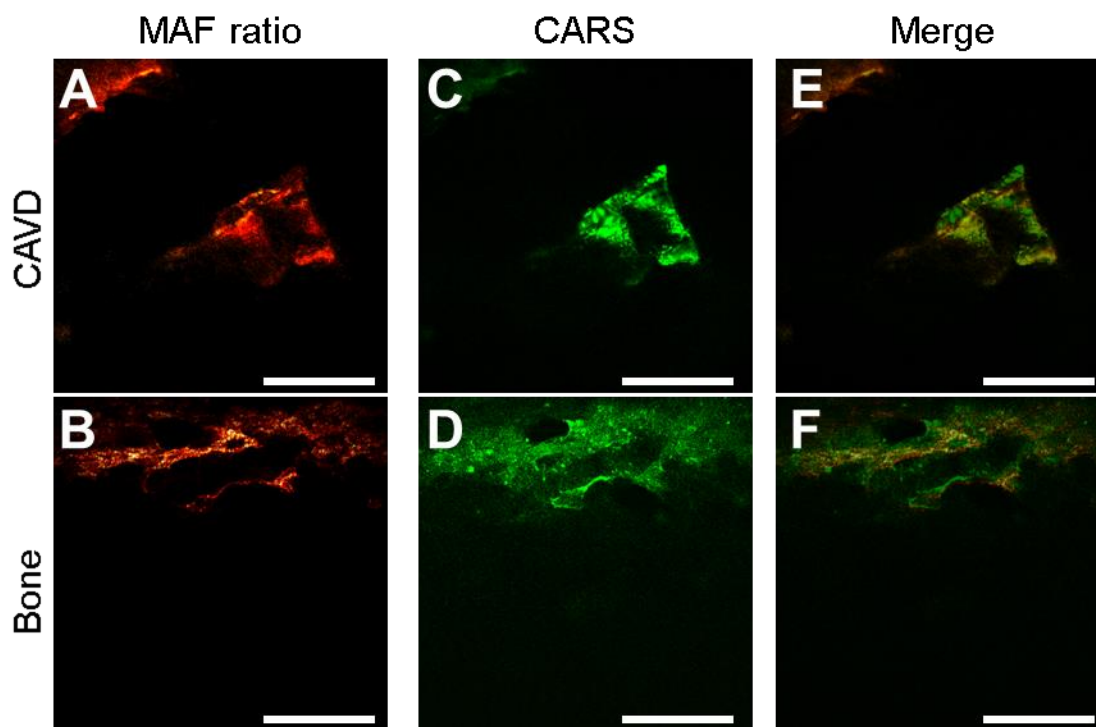


Figure 4.6: MAF signal overlaps with CARS images.

TPEF images taken on a an Olympus FX1000 with CARS imaging with CARS imaging capabilities were used to calculate the MAF for CAVD valves (A) and bone (B) samples. Corresponding CARS images of the same fields were taken (C,D) and merged (E,F). Scale bars are 100 μm .

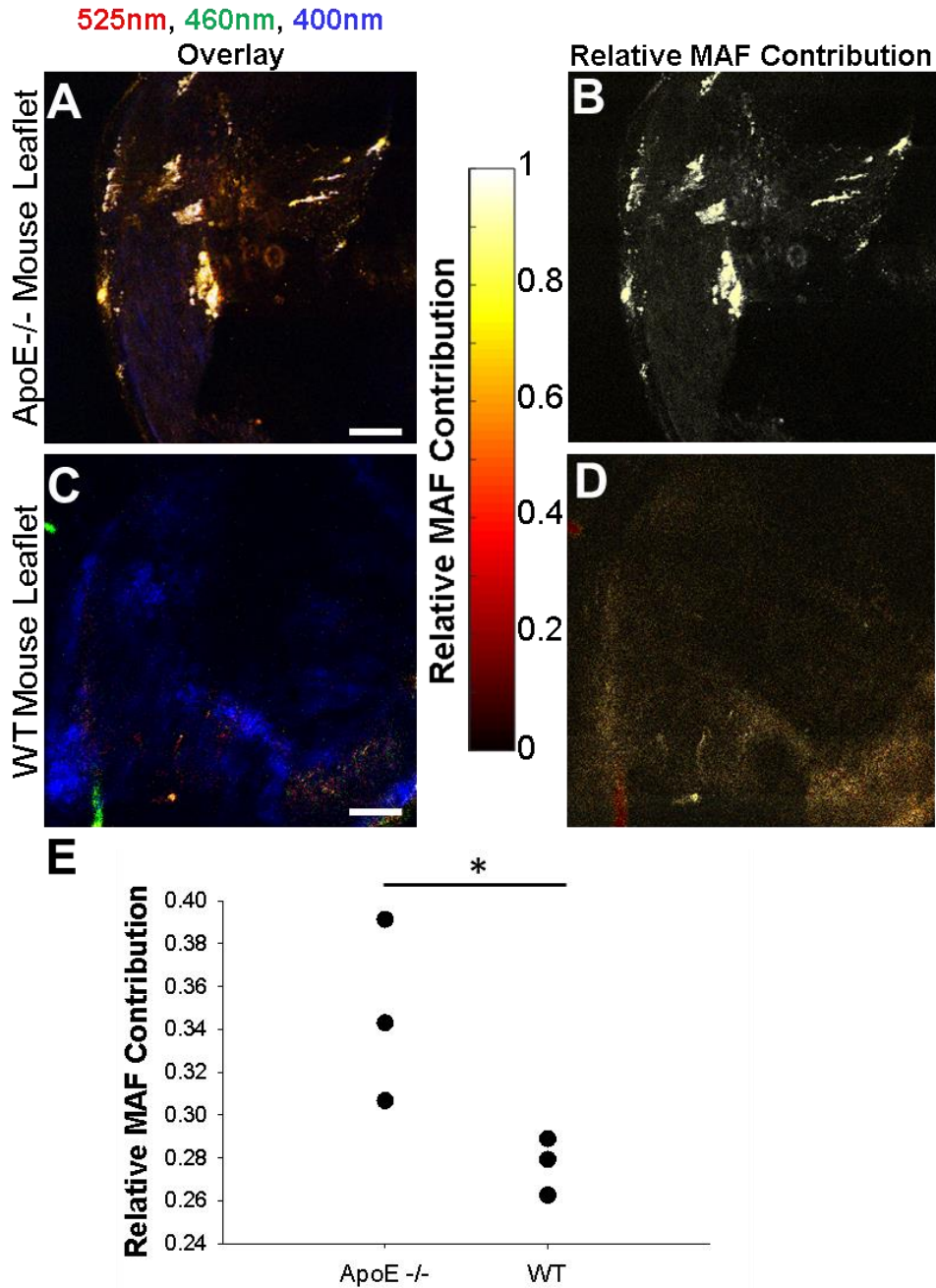


Figure 4.7: An ApoE^{-/-} mouse model confirms the use of the MAF as a quantifiable metric for calcification.

TPEF imaging of aortic valves from aged ApoE^{-/-} mice with an (A) intensity overlay of 525nm TPEF (red), 460nm TPEF (green), and SHG (blue), as well as (B) the calculated MAF concentration highlights distinct calcified nodules relative to wild type mice (C, D). The relative contribution of the MAF (E) is significantly increased in ApoE^{-/-} mouse valves (P=0.0525). Data is shown for 3 ApoE-

- valves and 3 WT valves. Scale bar is 100 μ m.

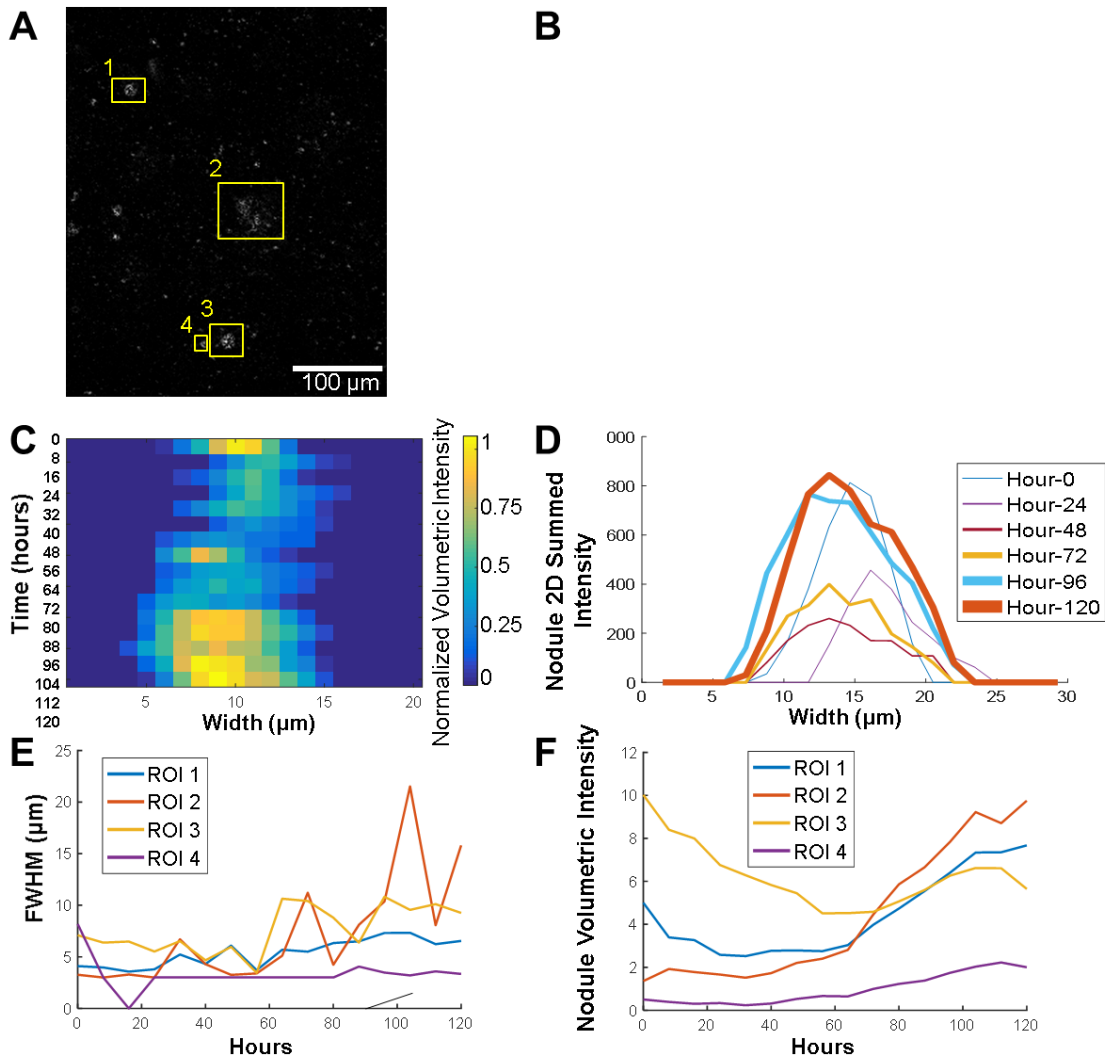


Figure 4.8: Time lapse experiment of calcification on PAAM gels shows measured change in nodule size.

(A) The 525nm/460nm image ratio at time zero of a 120 hour time lapse experiment showing 4 regions of interest (ROIs) used for analysis. (B) Representative time points of each ROI showing the regions that were analyzed. After taking the summed 3D projections and the 525nm/460nm ratio and calculating the MAF contribution, the sum along the image plane can be used to find the nodule volumetric intensity shown for the image stacks (B) and the individual line plots for the nodule volume over time (C). These images were then used to calculate the full width at half maximum (FWHM; E) and the area under the curve of the intensity profile of the 3D summed projections, or the volumetric intensity (F).

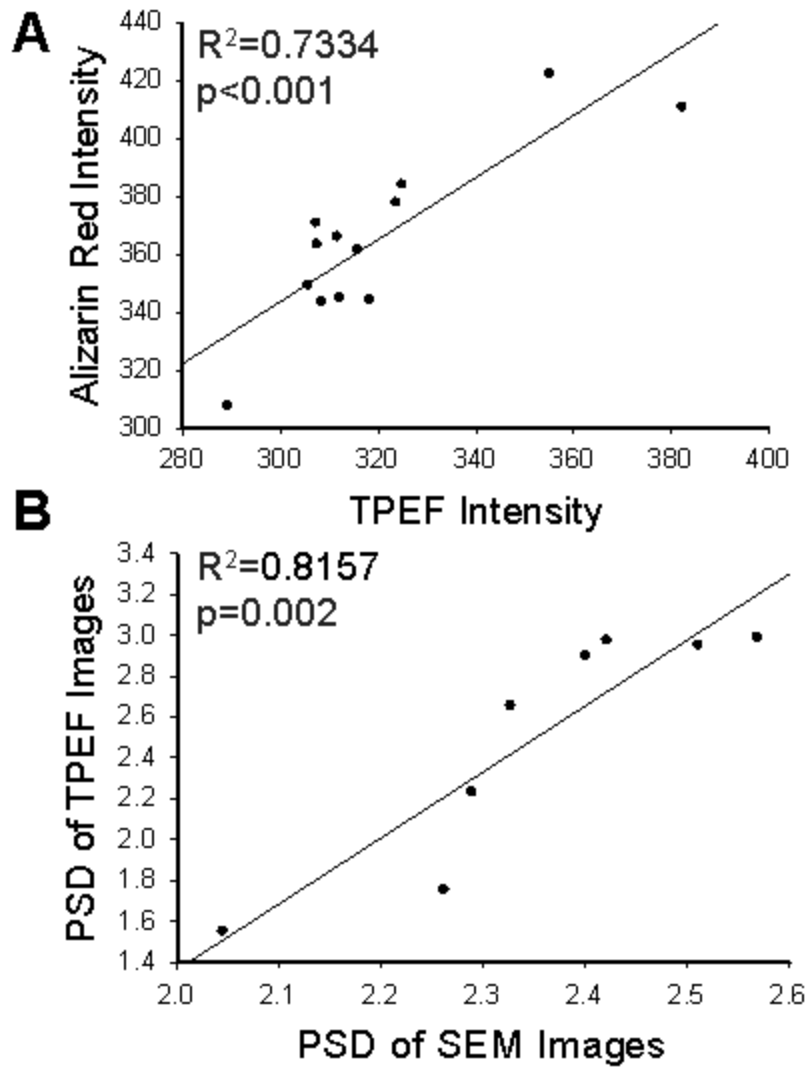


Figure 4.9: Correlating Alizarin Red images versus TPEF image and the PSD TPEF images versus the PSD of SEM images.

The intensity correlation of Alizarin Red images compared to the TPEF summed projection images of the same region give an R^2 value of 0.7334 (A). The power spectral densities of the SEM image and the TPEF images of the CAVD and bone samples showed a strong ($R^2=0.8157$) correlation (B).

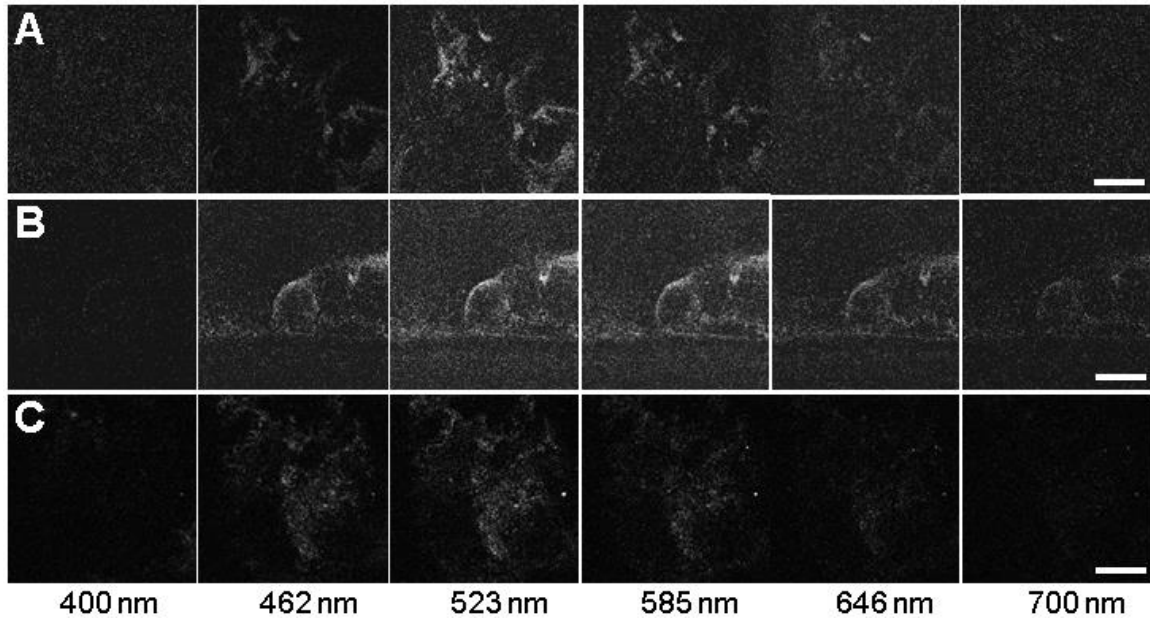


Figure 4.10: Representative series of images at different emission spectral bands using an 800 nm excitation.

Images are shown for (A) human CAVD valves, (B) nodules grown on PAAM gels, and (C) rat bone (800 nm excitation). Scale bars are 200 μm .

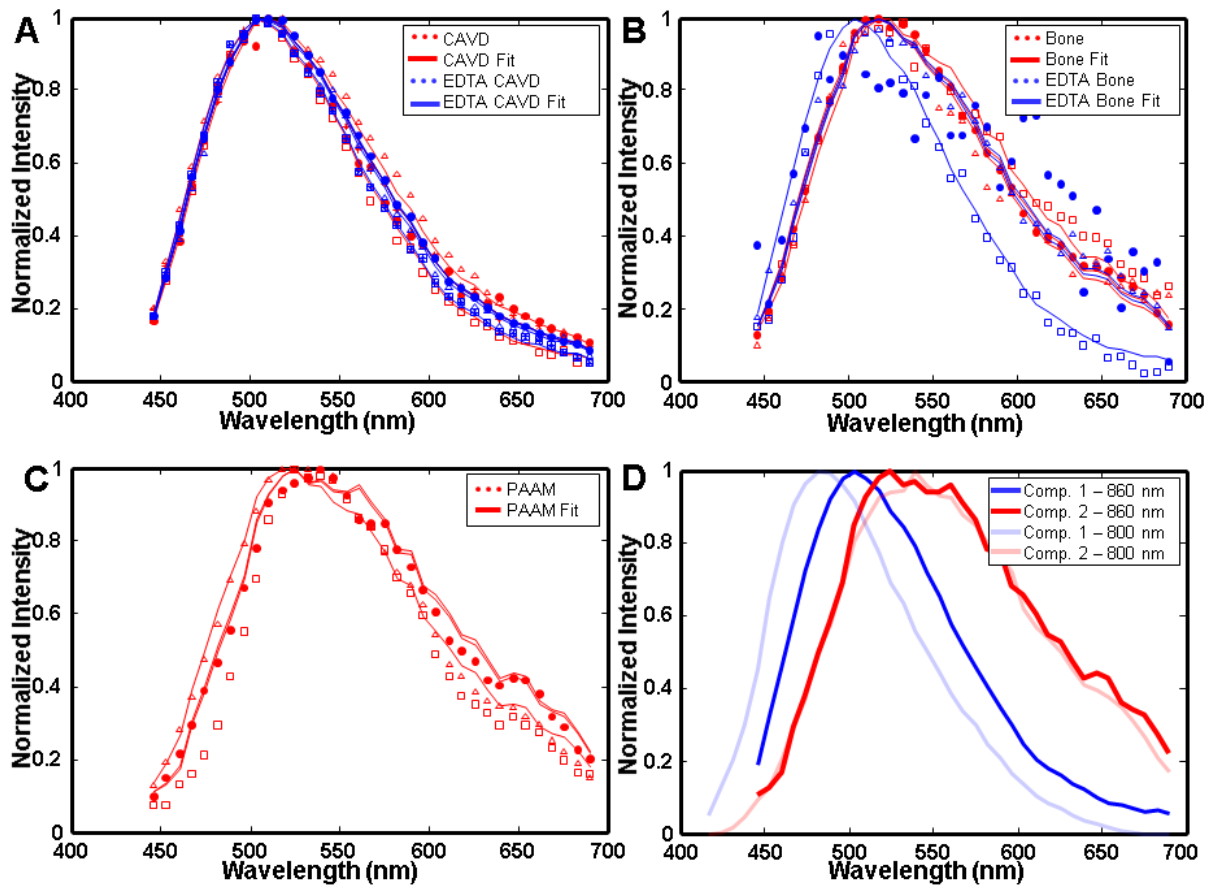


Figure 4.11: Emission spectra acquired using 860 nm excitation and component analysis.

Spectra are presented for human CAVD valves (A), rat bone (B), and (C) nodules grown on PAAM gels. Data sets are delineated using either triangles, squares, or dots; fits are shown using a solid line. Spectral decomposition demonstrated a two component model provided a good fit for human CAVD valves ($R^2=0.994\pm 0.011$), rat bone ($R^2=0.954\pm 0.071$), and nodules grown on PAAM gels ($R^2=0.982\pm 0.015$) specimens (A-C). The decomposed collagen (blue) and calcification (red) components at 860 nm excitation (D) were similar to those at 800 nm, with only a red shift in the collagen component evident at 860nm.

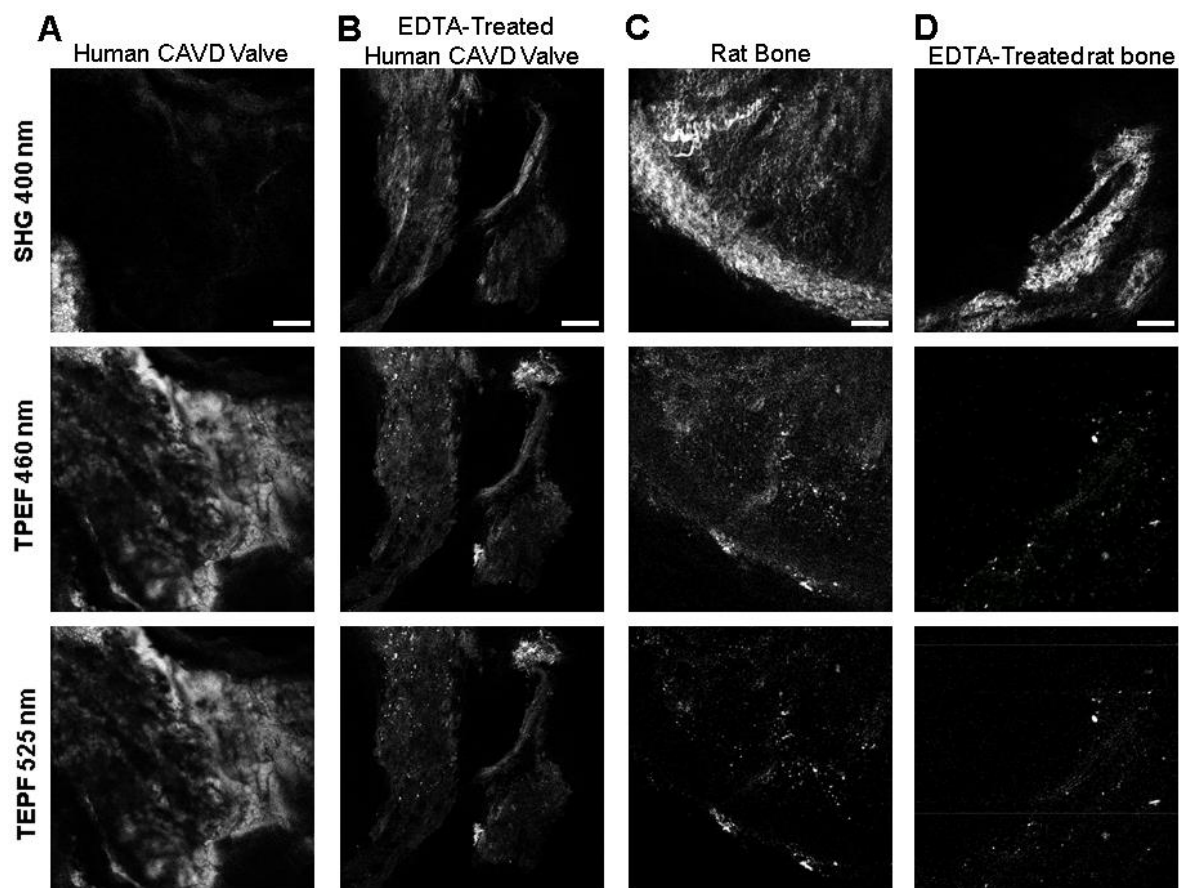


Figure 4.12: Representative TPEF and SHG images.

Images are depicted for human CAVD valves (A), EDTA treated, human CAVD valves (B), rat bone (C), and EDTA treated rat bone (D). Scale bars are 100 μm .

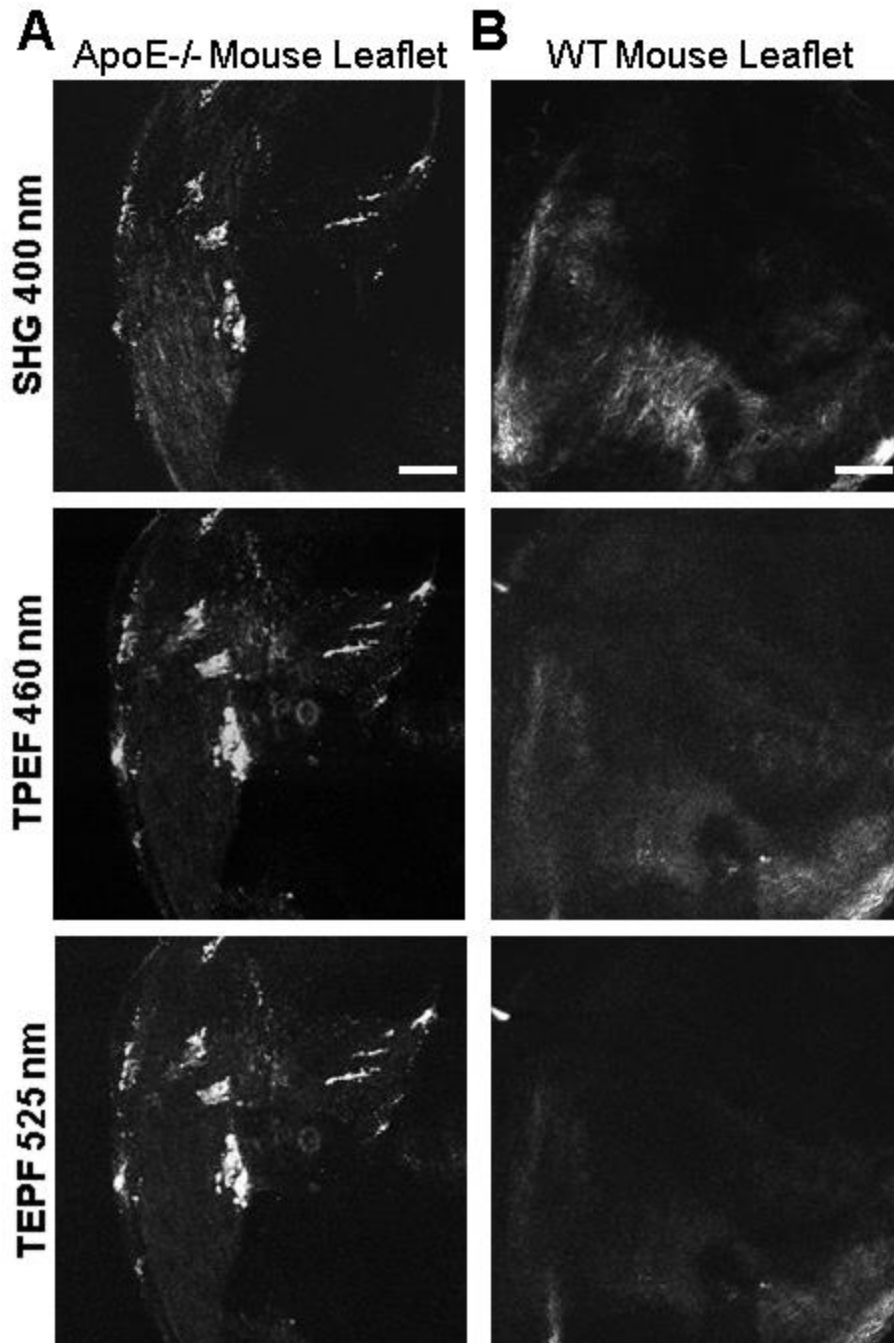


Figure 4.13: Additional, representative TPEF and SHG images.

Images are shown for ApoE^{-/-} mouse leaflets (A) and WT mouse leaflets (B). Scale bars are 100 μ m.

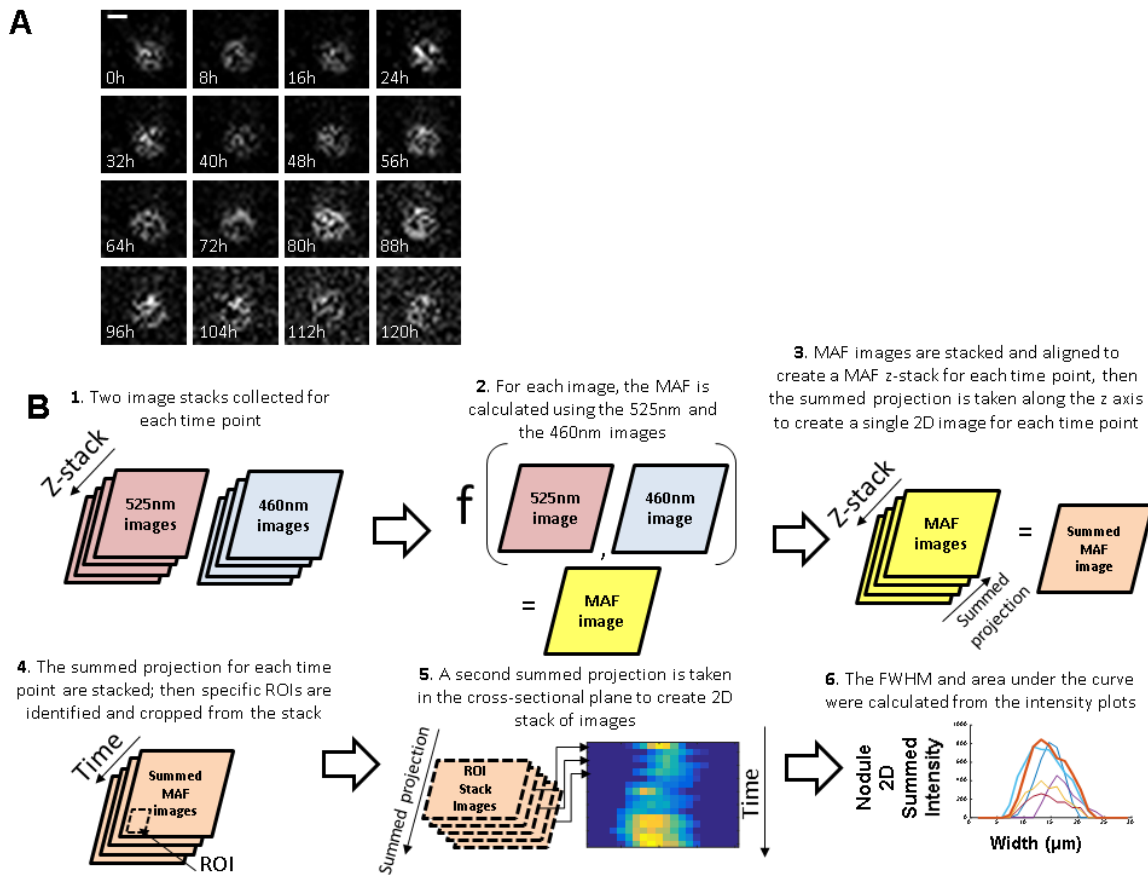


Figure 4.14: Summary of the PAAM gel time lapse experiment with representative images.

(A) Representative 525nm/460nm images of ROI 1 over the entire length of the 120 hour time lapse experiment. (B) Schematic of image processing to create MAF images and 3D image stacks used for calculations. Briefly, the 525nm and 460nm image stacks are used to calculate the MAF for each time point. The summed projection of each time point is then stacked and ROIs are selected for analysis. Scale bar is 10 μm .

Chapter 5. Using Large Scale Data Analytics to Direct *in vitro*

3D Model Experiments in CAVD

This work is based off of work currently being done in the Black Lab, but has not been published at the writing of this thesis. It leverages materials science, in making methacrylated hyaluronic acid, provided by Dr. Spencer Fenn as well as the imaging equipment available for use in the microscopy core at Tufts University under the supervision of Prof. Irene Georgakoudi. It also uses raw RNA-sequencing data that was previously published,²⁴⁹ but with our own analysis. I have done all of the analysis and data collection shown in the chapter, under the advisement of Prof. Lauren Black, along with the writing of the chapter.

Abstract

Calcific aortic valve disease (CAVD) is a degenerative disease of the aortic valve that has recently been the subject of large scale data investigations. Since full valve replacement surgery is the only treatment option available for patients with CAVD, there is a need to understand the disease mechanisms in order to find pharmaceutical targets. Here, we combine existing RNA-sequencing data from human aortic valve tissues with and without CAVD with our 3D, methacrylated hyaluronic (MeHA) system to probe the extracellular matrix (ECM) proteins that change with disease. The MeHA gels incorporated five identified ECM proteins - decorin, collagen IV, periostin, aggrecan, and fibrinogen – and assessed porcine valve interstitial cell (pVIC) response using non-destructive optical techniques. We then evaluated the development of calcification of pVICs in the MeHA system using our previously developed non-invasive, multiphoton-based imaging technique.

5.1 Introduction

Calcific aortic valve disease (CAVD) is an age-related disease characterized by fibrotic thickening of the aortic valve leaflets that can lead to calcification and bone formation. As much as 30% of the population over the age of 65 may be affected by CAVD,²⁵⁰ however, the only treatment option available is surgical replacement of the valve. To lower the medical burden of CAVD and lessen the need for these surgical procedures, the development of pharmaceutical treatment methods is imperative. To do this, a more thorough understanding of valve disease is required in order to find chemical therapies to target disease pathways involved in CAVD. Traditionally, the use of disease model systems has led to discoveries surrounding human maladies and could again help in finding treatments for CAVD.

Unfortunately, there is a lack of animal models for CAVD that accurately recapitulate the disease. Currently, the best model of CAVD uses swine that are fed a high fat diet.¹⁹⁶ While the porcine aortic valve is anatomically very similar to humans and the disease happens naturally on a high fat diet (no genetic modification needed), the model is slow and expensive, limiting its ability to provide high throughput data analysis and drug screening. Other animal models of CAVD, such as those using genetically modified mouse and rabbit, do not accurately describe the disease. Mouse valves, for example, do not have the same tri-layer structure found in humans²⁵¹ and both rabbit and mouse models must be either genetically modified or fed a high fat diet to induce calcification.²³⁵ Additionally, even in these smaller animal models, time to calcification and expense can be significant factors in limiting the usefulness of these models. Because of this, in recent years, *in vitro* models of CAVD have become more popular.²⁵²

High throughput screening has the obvious benefit of being able to test many variables in a system at once or in rapid succession. In combination with the rise of large scale data, such as transcriptomics, researchers now have the ability to look for and test exponentially more possible factors for different diseases. In CAVD, there are many changes that happen to both valve cells and the extracellular matrix (ECM). In fact, a hallmark of CAVD progression is characterized by marked changes to the ECM.²⁰ With advanced disease, there is a loss of the aligned collagen architecture seen in the aortic facing side of the valve leaflets, called the fibrosa. The leaflets also go through an overall thickening of the tissue caused by an increased in ECM in both the fibrosa and the middle layer of the valve, the spongiosa. While gross changes in the leaflet can be measured when human valves are removed during aortic valve replacement surgery, less is known about the subtle changes to the composition that happen during the disease progression.

Furthermore, specific ECM proteins have been shown to influence mineralization in CAVD²² and could be a target for non-surgical intervention strategies to CAVD treatment.

RNA sequencing (RNA-seq) can provide a snapshot of cells in diseased and healthy tissue. By leveraging existing RNA-seq data and a catalogue of mRNAs, non-coding RNAs and small RNAs, key differences in diseased cells, as compared to healthy cells, can be discovered. Quantitative measurements for every molecule in a cell population can be collected and used to see differences at various stages of the disease progression.²⁵³ In addition to being more accurate than microarrays at quantifying gene expression,²⁵⁴ RNA-seq can help identify novel transcript clusters that can help with the understanding of cardiac disease.²⁵⁵ Large volumes of transcriptomic data, such as with RNA-seq, can help parse out potential key players that have previously taken researchers years to fully understand through bench top methods; however, these potential factors still need to be assessed. High-throughput analysis methods and cell culture systems can help sort through the large volume of information to identify important pathways in disease progression.

In addition to analyzing large scale data sets that describe individual pieces of a system by taking them apart, non-linear imaging techniques can use near-infrared light to non-destructively image whole cells in a complete 3D environment. Second harmonic generation has been used to image collagen fibers²⁰² and non-linear imaging can also capture signal from elastin⁷⁹ *in vivo*, two of the major ECM components of the aortic valve,²⁵⁶ and can be used to assess ECM in *in vitro* models. Recently, we developed a method that can quantify mineralization found in valve tissue,¹⁵⁴ expanding the range of non-linear microscopy methods that can be used to study CAVD. All of these techniques

can be used to collect three dimensional scans of either a tissue or a model system and, because they are non-destructive, the samples can be imaged for multiple time points and/or analyzed using other techniques concurrently. Improvements in imaging technology has also decreased image acquisition time reducing the risk of adverse effects from imaging outside of a cell culture environment. Overall, leveraging these techniques and data, we are able to test the effects of multiple ECM proteins identified as possible exacerbators of valve tissue mineralization.

In this study, we combined our own analysis of existing RNA-seq data with our high-throughput, 3D system to study CAVD. The results from the RNA-seq analysis identified five initial proteins to test in our system - decorin, collagen IV, periostin, aggrecan, and fibrinogen - which can be bulk incorporated into our 3D, methacrylated hyaluronic acid (MeHA) based system.²⁵⁷ We used non-linear imaging approaches designed in our lab¹⁵⁴ to assess the system, non-destructively, over several time points to see how changes in ECM proteins can influence mineralization in porcine valve interstitial cells (pVICs).

5.2 Methods

5.2.1 RNA-Sequencing and Network Analysis of CAVD versus Normal Human Valves

RNA-sequence data was previously collected²⁴⁹ and used for analysis in this study. The GEO and GEO2R tool, run by the National Center for Biotechnology Information (NCBI), were used to assess the differences between human valve tissue from healthy individuals and patients suffering from CAVD. The identified genes were sorted based on their gene ontology description to only include those related to the extracellular matrix. These 410 unique, identified ECM related proteins were then run through the STRING database²⁵⁸ for network analysis. From this analysis, the ECM proteins that had the most connections

based on their interactions with other genes (assuming a 0.4 confidence interval) were cross-referenced to the statistically calculated p values from the GEO2R tool. This was done to find proteins that were both drastically altered in the disease state and have a large influence on all of the ECM proteins found in the RNA-seq analysis. From this ranking, and their availability to purchase, five proteins were chosen for initial testing.

5.2.2 Making Methacrylate Hyaluronic Acid

Research grade 700 kDa sodium hyaluronate (Lifecore Biomedical, Chaska, MN [HA700K]) was combined with methacrylic anhydride (Sigma-Aldrich, St. Louis, MO, [276685]) as previously described.²⁵⁹ Briefly, 1 g of 700mw sodium hyaluronate was added to 100 mL of sterile 1X PBS. This was dissolved in a beaker with a stir bar. Methacrylic anhydride was added in a 20 times excess concentration which was calculated to be 7.4 mL of methacrylic anhydride. The resulting solution was monitored overnight and periodically adjusted to a pH of 8 with 5N sodium hydroxide. The reacted solution was then hydrolyzed through extensive dialysis for 5 days with diH₂O changes at least once every 12 hours.

5.2.3 Porcine Cell Isolation and Culture

Porcine hearts were obtained from Tufts Medical Center on ice, within an hour of animal sacrifice. The aortic valve leaflets were isolated from the hearts and porcine valve interstitial cells (pVICs) were collected as previously described.²⁶⁰ Prior to receiving the hearts, 100 mL of collagenase solution was made by dissolving 1.33g of powdered DMEM (ThermoFisher Scientific, Waltham, MA, [90-013-PB]), 0.37g of sodium bicarbonate (Sigma-Aldrich, St. Louis, MO, [S5761]), and 600 U/mL collagenase type II (Worthington Biochemical Corp., Lakewood, NJ, [L5004177]) in 84 mL diH₂O with 1% (v/v) Fungizone

(ThermoFisher Scientific, Waltham, MA, Antibiotic-Antimycotic [15240062]). The pH was adjusted to 7.2 and the total volume was brought to 90 mL. 10mL of fetal bovine serum (FBS, ThermoFisher Scientific, Waltham, MA [16000-044]) was added to bring the total volume to 100 mL and then the entire solution was sterile filtered. Next, porcine VIC medium consisting of Duplecco's Modified Eagle's Medium (DMEM; ThermoFisher Scientific, Waltham, MA [10566016]), 1% Fungizone, 1.85g/500mL sodium bicarbonate, and 10% FBS was made.

When the porcine hearts arrived at the biosafety cabinets, the whole aortic leaflets were isolated. A serial sterile wash was done, rinsing the leaflets for 3 minutes in first 2.5%, then 2%, 1.5% and 1 % Fungizone solutions, each for 3 minutes. The leaflets were then digested for 10 minutes in the collagenase solution. Periodically during the digestion sterile cotton swabs were used to gently scrap off the endothelial cell layer. The leaflets were then moved to a new conical of collagenase solution and incubated for 12-18 hours with slow mixing. After digestion, the leaflets were centrifuged for 5 minutes at 1000 RPM and the supernatant was aspirated. The VICs were then re-suspended in porcine VIC media, centrifuged with the supernatant being removed again, and then re-suspended in VIC media and plated in a T75 flask and allowed to adhere. VICs were kept at normal cell culture conditions (37°C at 5% CO₂) and fed porcine VIC media. Cells from passages 2-6 were used for experiments.

5.2.4 3D MeHA Gel Formation

Prior to MeHA formation, glass slides were activated to allow for chemical adhesion of gels. As previously described,²⁶¹ glass slides were sonicated for 5 minutes in ethanol (ThermoFisher Scientific, Waltham, MA, [04-355-305]), the ethanol was replaced, and the

slides were sonicated for an additional 5 minutes. The slides were then sonicated for 5 minutes in deionized water. A solution of 5% (v/v) of 3-(Trimethoxysilyl)propyl methacrylate (TMSPMA; Sigma-Aldrich, St. Louis, MO, [440159]) in toluene (Sigma-Aldrich, St. Louis, MO, [24529]) was prepared. Slides were placed in an oven at 60°C overnight in the prepared TMSPMA/toluene solution. The slides were then rinsed twice with ethanol and twice with deionized water before being stored at room temperature. Slides were sterilized with ethanol before use in cell culture.

The prepared MeHA powder was weighed out to create either a 2%, 3%, or 4% (w/v) solution. A 1M solution of ammonium persulfate (APS; Sigma-Aldrich, St. Louis, MO, [A3678]) in diH₂O was prepared. The MeHA powder was put into a sterile 2mL syringe with 1mL of either only porcine VIC media or porcine VIC media with VICs at a concentration of 10,000 cells/mL. The syringe was connected to a second syringe using a female-to-female Luer lock connector for mixing. The solution was mixed by moving the liquid back and forth until the MeHA was dissolved. Then, 1.5 μ L of tetramethylethylenediamine (TEMED; Sigma-Aldrich, St. Louis, MO, [T7024]) and 18 μ L of the APS solution was added to the syringes and quickly mixed. Before gelation, all of the solution was moved to one syringe a pipette was used to move small amounts of the solution to the glass slides. On the activated glass slides, 8 μ L dots were created and covered with a non-activated glass slide, with 2 coverslips acting as spacers on each side of the slide. Gels were allowed to fully form for 45 minutes in an incubator after being placed in a sterile 10 cm petri dishes. After gelation, 10 mL of VIC media was added to the petri dishes for culture.

5.2.5 Atomic Force Microscopy of MeHA Gels

MeHA gels of varying concentration were measured using atomic force microscopy (AFM). A Veeco Dimension 3100 AFM was used with Novascan borosilicate glass particle (20 μm diameter bead) probes. The probes had a rated spring constant value of 0.6 N/m and the Hertzian theory was used to calculate the Young's Modulus, assuming the samples were incompressible (the Poisson's ratio was assumed to be 0.5). The Young's Modulus was calculated using a MATLAB code for each indent curve over an entire 2D force volume and then averaging those calculated values for each sample. Standard error bars were calculated by measuring the modulus values for multiple gels of the same MeHA concentrations.

5.2.6 Immunostaining and Single Fluorescence Imaging

The MeHA gel dots containing VICs were fixed in 10% buffered formalin (ThermoFisher Scientific, Waltham, MA, [SF100]) for 20 minutes. After rinsing three times for five minutes with dH_2O , the gels were permeabilized with 0.1% TritonX-100 in PBS for 20 minutes and then blocked with 5% donkey serum in 1% bovine serum albumin (BSA; Sigma-Aldrich, St. Louis, MO, [A9418]) in PBS. Cell nuclei and actin fibers were stained with 4',6-Diamidino-2-Phenylindole, Dihydrochloride (DAPI; ThermoFisher Scientific, Waltham, MA, [D1306]) and Phalloidin (ThermoFisher Scientific, Waltham, MA [A12379]), respectively. Samples were then washed three times for five minutes and imaged using an Olympus IX81 microscope equipped with spinning disk confocal and Metamorph Basic software (version 7.7.4.0, Molecular Devices). Image analysis and compilation was done using ImageJ.¹⁰⁶

5.2.7 Multiphoton Imaging of MeHa Gels

The prepared MeHA gel dots were cultured with VICs under various cell culture conditions described above. Slides with the MeHA dots were imaged using a Leica TCS SP8 (Wetzlar, Germany) microscope. Z-stacks were collected with the following filters 400 nm \pm 10 nm (Chroma, Bellows Falls, VT, [ET400/20X]), 460 \pm 20 nm (Chroma, Bellows Falls, VT [HQ460/40m-2p]), and 525 \pm 25 nm (Chroma, Bellows Falls, VT, [ET525/50M-2P]) for each dot with the following specifications: 800nm excitation, emission 400nm, 460nm, and 525nm. All images were collected using a 25x water immersion objective.

For analysis, the mineralization associated fluorescence (MAF) was calculated as previously described,¹⁵⁴ by using emission signal from the 460nm and 525nm channels taken with a 800nm excitation. The SHG collagen signal was found by using the 800nm excitation with the 400nm filter. All calculations were done using custom MATLAB code.

5.3 Results

5.3.1 Network Analysis of the Genes Identified Using RNA-Seq

Using genes identified in the GEO2R software as significantly different in human CAVD valves as compared to normal human valve tissue, network analysis was done with the STRING database. By ranking the proteins associated with the ECM, via gene ontology process and function descriptions, using both the p value (as a level of difference between diseased and healthy) and the number of connections found with a 40% confidence or higher in the network analysis, several ECM proteins were found. **Figure 5.1** shows the network map that was created with the STRING database. From this list, several ECM proteins were identified as potential key players in CAVD. **Table 5.1** lists the ECM proteins and their descriptions used for the remainder of the experiments.

5.3.2 Creation and Testing of MeHA Gels

Small, 3D constructs of MeHA gels were made with and without cells. **Figure 5.2 A** shows the chemical process of methacrylating HA, while **Figure 5.2 B** and **C** gives a schematic and photograph of the gels created on activated glass slides. These gels were mechanically tested with AFM to determine how elastic modulus changed with MeHA concentration (**Figure 5.3 A**). Cell viability was also tested by incorporating pVICs into the MeHA solution, before gelation, and allowing them to set with the gels. After 3 days of culture, the MeHA gels with the pVICs showed that the cells had minimal stretching, maintaining a rounded morphology, but stayed encapsulated within the 3D constructs (**Figure 5.3 B**).

Images of the MeHA gels with pVICs were also taken to determine the MAF contribution inside the constructs after one week. A trend is seen in the MAF contribution showing an increase in signal, indicative of increased mineralization, in the 1% MeHA gels compared to the 3% MeHA gels (**Figure 5.4 A**). While this is opposite the results seen in the 2D studies, where stiffer environments tend to show more mineralization, further study is needed to fully understand the difference in pVIC response in a 3D environment.

5.4 Discussion

The development of pharmaceutical methods to treat CAVD could significantly improve both the quality of life and life expectancy of thousands of Americans. However, research into valve calcification has been hindered by the lack of model systems that accurately recapitulate the disease and an incomplete understanding of the beginning stages of the disease. The use of large data sets, such as genome-wide association studies, have been previously used to find²⁶² and investigate the subsequent results, leading to associations

of low-density lipoproteins,²⁶³ NOTCH1,⁵² as well as others²⁶⁴ with CAVD. Large scale studies like these have helped move research forward and the development of recent tools, such as transcriptomics, have the potential to accelerate this progress even more. Here, we wanted to leverage existing RNA-seq data to look for changes in RNA expression of ECM proteins.

By combining results from the GEO2R database showing changes in RNA expression levels between human stenotic and normal valves and a network analysis using the STRING database, we were able to find a set of ECM proteins that were both significantly altered with disease and connected to the expression of several other genes. These proteins - decorin, collagen type IV, periostin, aggrecan, and fibrinogen – can then be incorporated into the 3D, MeHA model that we have created. MeHA, which is created by introducing methacrylate groups to HA,²⁶⁵ is more mechanically robust than native HA²⁶⁶ and, we showed, can be tuned to physiologically relevant stiffnesses. This MeHA system can also be assessed, non-destructively using the endogenous fluorescence of many fluorophores. Rapid analysis of mineralization and fibular collagen production can all be achieved using non-linear microscopy that has been shown to work in our system. The five ECM proteins identified in the above study will be the first to be incorporated into our system.

Each of these chosen ECM proteins have properties that could already be associated with CAVD specifically or have attributes that could exacerbate valve stenosis, but have yet to be described. Decorin is a proteoglycan that is closely associated with collagen fibrillogenesis and degradation, including being upregulated in fibrosis.²⁶⁷ Increases in decorin have also been shown to occur in degenerative lesions found in aortic aneurysms and were shown to possibly facilitate the progression of the aneurysm by activating

macrophages.²⁶⁸ Collagen type IV (col IV) is a less ridged collagen that is known to form collagen networks.²⁶⁹ Interestingly, while col IV was upregulated in stenotic valve patients, previous studies have conflicting reports describing both a decrease in mineralization in cells grown on col IV²⁷⁰ and col IV has also been found in osteoarthritic cartilage.²⁷¹ Hopefully, our 3D MeHA system will be able to more clearly state the role of col IV in calcification. Periostin is already known to be very important in valve development²⁷² and can interact with both TGF- β and bone morphogenetic protein (BMP) during valve disease.²⁷³ Additionally, periostin has been directly linked to valve tissue remodeling and calcification²⁷⁴ through Notch1 signaling²⁷⁵ and so is an ideal candidate for additional *in vitro* testing. Aggrecan, another important valve development protein,²⁷⁶ can bind directly to HA.²⁷⁷ However, its role in valve disease is not well understood; though a study of chondrogenesis suggested aggrecan could play an inhibitory role to mineralization.²⁷⁸ Lastly, fibrinogen is primarily known for its role in clot formation, forming fibrin after cleavage with thrombin. In valves, however, the focus of fibrinogen has predominately been surrounding plasma fibrinogen as a possible valve disease biomarker.^{279,280} Therefore, understanding the direct role fibrinogen has on pVIC calcification may improve our broader comprehension of CAVD.

Initial next steps for this project is the full integration and testing of these five ECM proteins in the MeHA system. Our preliminary testing suggests the MeHA gels seeded with pVICs are a nontoxic and optical clear system in which we can track nodule growth and cell response. Subsequent studies can include different ECM proteins or could combined two or more ECM proteins within the same MeHA gel. Based on the results of these experiments, further testing can be repeatability conducted to look for mechanistic pathways with the potential for pharmaceutical intervention. Another potentially useful

imaging approach that could be used in tandem with the other non-linear microscopy techniques would be to collect signal from nicotinamide adenine dinucleotide (NAHD) and flavin adenine dinucleotide (FAD) to describe the metabolic activity of the pVICs in the MeHA system. However, use of this technique with the MAF method will require additional experiments to fully separate the fluorescence signals necessary for each imaging modality.

5.5 Conclusion

The development of a MeHA based 3D model system could help further our understanding of the role of ECM proteins in CAVD. Using existing RNA-seq data, we found a list of five ECM proteins that are significantly altered in human aortic valves with CAVD and are prominent players in gene networks. These ECM proteins will be incorporated into the MeHA system and optical techniques will be used to non-destructively measure calcification and fibular collagen formation.

5.6 Tables and Figures

Table 5.1: Genes identified through network analysis for testing the MeHA gels

Gene Symbol	Gene Name	Top 3 GO Functions	Top 3 GO Processes
DCN	Decorin	Collagen binding; extracellular matrix binding; glycosaminoglycan binding	Aging; chondroitin sulfate biosynthetic process; chondroitin sulfate catabolic process
COL4	Collagen type IV	Extracellular matrix structural constituent	Cell adhesion; collagen catabolic process; extracellular matrix organization
POSTN	Periostin	cell adhesion molecule binding; heparin binding; metal ion binding	bone regeneration; cell adhesion; cellular response to fibroblast growth factor stimulus
ACAN	Aggrecan	Carbohydrate binding; extracellular matrix structural constituent; hyaluronic acid binding	Cell adhesion; central nervous system development; extracellular matrix disassembly
FG	Fibrinogen	Contributes to cell adhesion molecule binding; metal ion binding; protein binding	Acute-phase response; adaptive immune response; blood coagulation

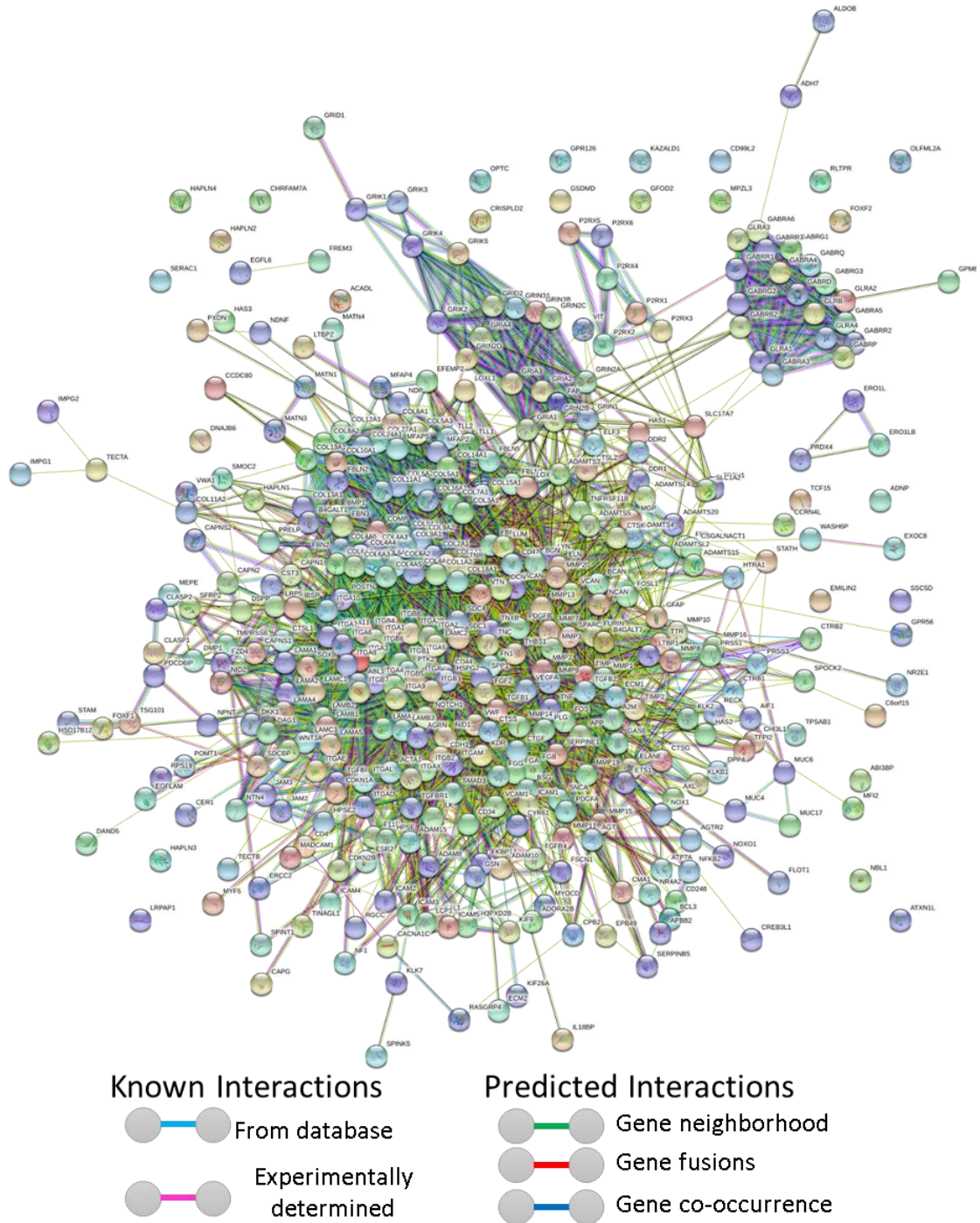


Figure 5.1: Network analysis of ECM proteins identified by RNA-seq.

Genes found to be significantly different in human CAVD patients compared to normal valves were found using RNA-seq. ECM proteins were further isolated using the gene ontology (GO) process and function descriptions and analyzed using the STRING database. The STRING network analysis is shown.

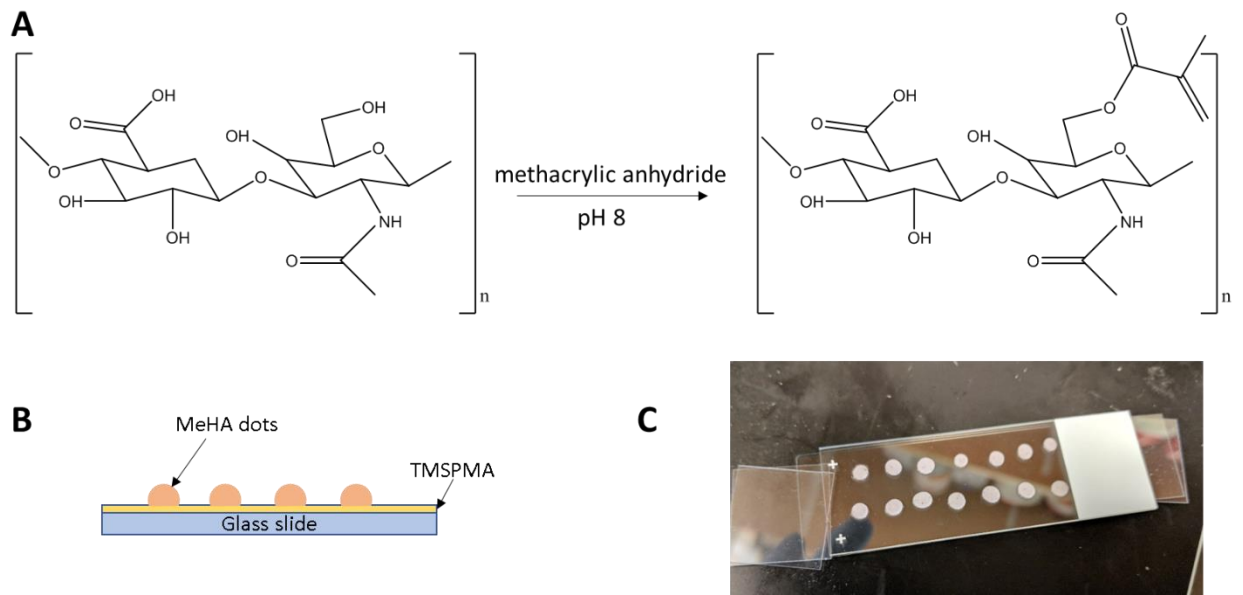


Figure 5.2: Development of a 3D MeHA gel system.

(A) Hyaluronate is reacted with methacrylic anhydride to create methacrylated HA (MeHA). The MeHA is polymerized with APS and TEMED with or without porcine VICs onto activated glass slides (B) and allowed to gel (C).

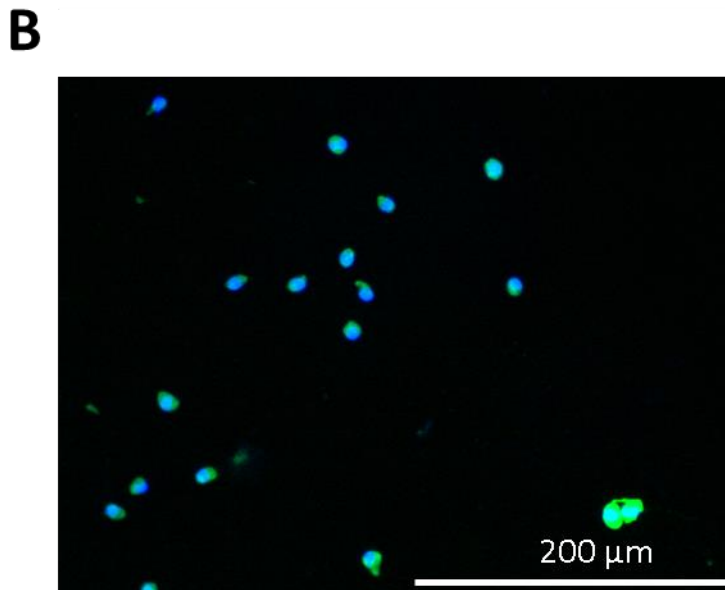
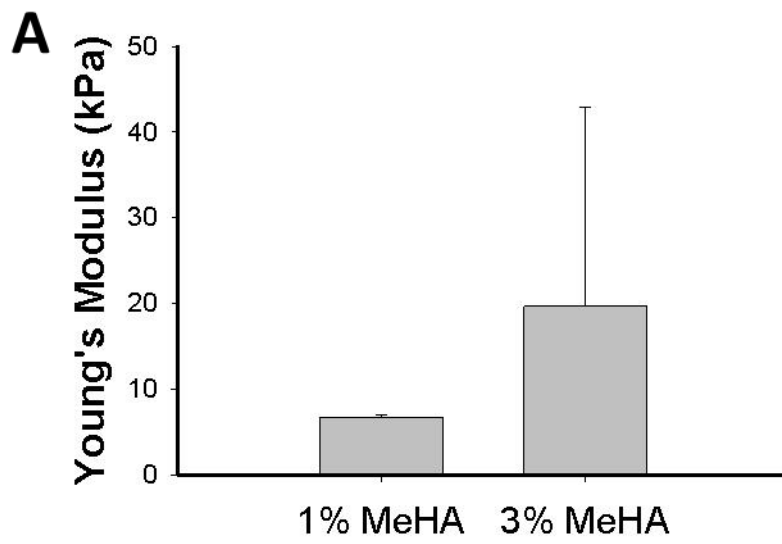


Figure 5.3: MeHA gel characteristics.

(A) Initial studies of different concentrations of MeHA gel modulus show physiologically relevant stiffness that can be used to culture porcine VICs. (B) Staining with DAPI (blue) and phalloidin (green) show that the cells have a rounded morphology, but are viable in the MeHA gels.

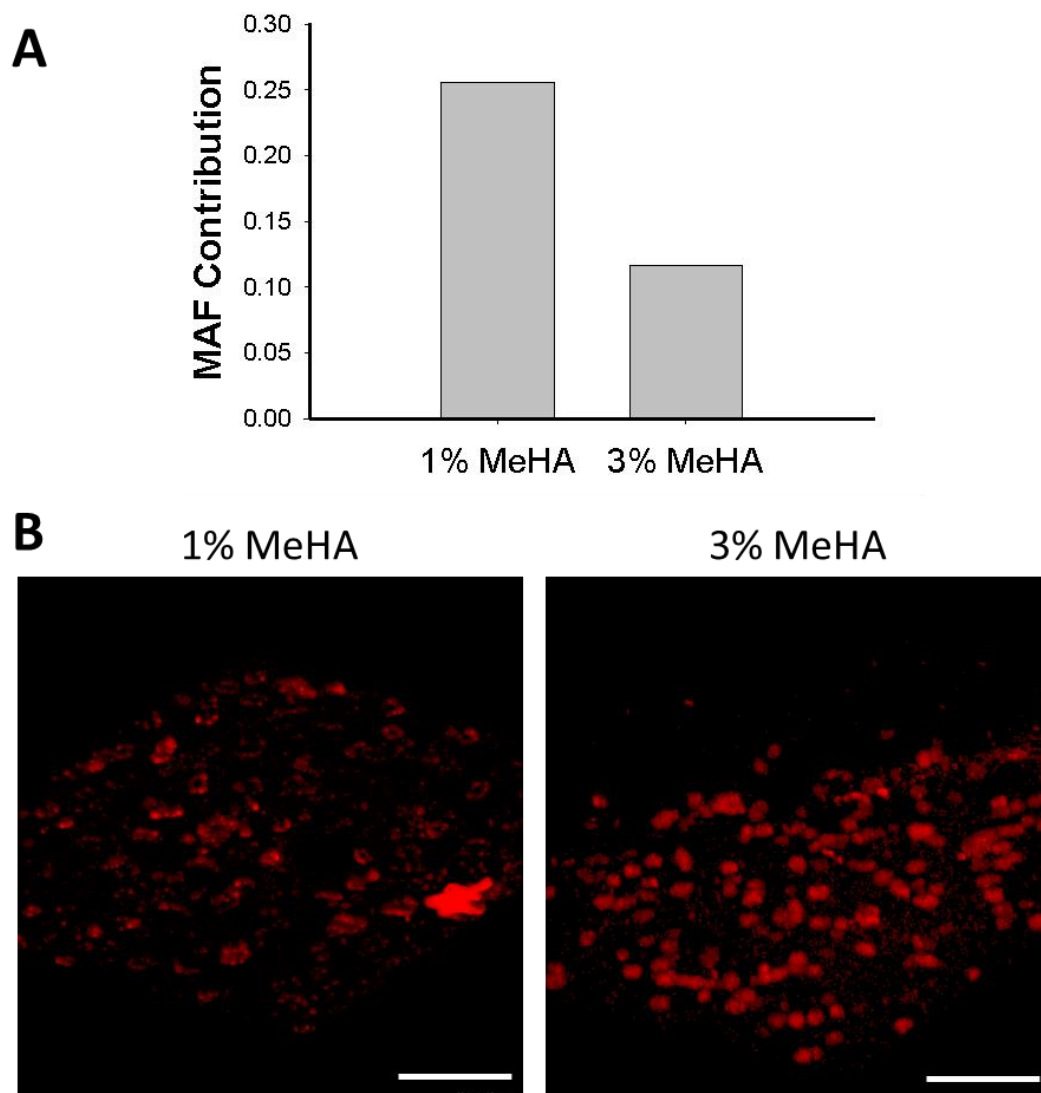


Figure 5.4: Optical measurements of MeHA gels.

(A) There is a trend of less MAF contribution signal seen in 3% MeHA gel than 1% MeHA gels after a week in culture. (B) Representative images of the 525nm channel (ex. 800nm) showing a rough estimate of the MAF contribution. Scale bars are 100 μm .

Chapter 6. Conclusions and Future Directions

The goal of this dissertation was to add to the body of knowledge surrounding CAVD. In this work, we showed that the ECM could play a critical role in the advancement of CAVD and we also identified a potential disease pathway as a target for pharmaceutical treatment. Additionally, we designed and tested a novel animal model of CAVD using a Tie2 driven knockout of pRb and came up with a new high throughput 3D *in vitro* approach to continue the study of ECM proteins on the calcification of VICs. In order to better assess mineralization not only in our *in vitro* systems, but also immediately *ex vivo* (with the reasonable expectation of being able to design for an *in vivo* system), we developed a non-destructive imaging technique that can quantify calcification. Both of these systems leveraged large data sets, including a genome-wide association study and existing transcriptomics data, to make advancements in the field. While there is still work to be done and to be continued in all aspects of this work, there have been noteworthy steps forward on many fronts in the battle against CAVD.

6.1 Conclusions

6.1.1 ECM Driven Treatment Possibilities of CAVD

The development of a 2D, polyacrylamide-based system combined the variables of physiologically relevant substrate stiffnesses with two separate ECM components – collagen and hyaluronic acid (HA). VICs were allowed to calcify after a 24-hour dose of TGF- β_1 over a three-week period. This showed that there had been remarkable variation in the amount of calcification with different ECM proteins. HA caused more mineralization after three weeks than the collagen, but this was the opposite effect seen after only a week in culture (**Figure 2.2**). Differences in cell spread area and changes in the substrate

surrounding nodules were also seen between VICs grown on HA versus collagen, with HA causing more pathological effects at later time points. This led to the study of two binding proteins of HA, RHAMM and CD44, using siRNA knockdown.

While knockdown of RHAMM did not produce any appreciable differences in mineralization levels, siRNA knockdown of CD44 significantly decreased calcification *in vitro*. In the CD44 knockdown samples, gene and protein expression, measured by qPCR and western blotting, showed an initial increase in the expression of osteopontin (OPN) – a gene associated with osteogenic processes. (**Figure 2.5** and **Figure 2.6**). Since OPN has been shown to decrease mineralization *in vitro*,¹¹³ it has the potential to influence the outcome of CAVD. Unfortunately, OPN is a complex molecule involved in many processes in the body^{118,281} so using OPN as a pharmaceutical target for CAVD may be challenging. CD44 on the other hand, is a less pervasive molecule in the body and could, therefore, be a potential target. Additionally, there have already been advances in developing drugs for CD44,¹²⁴ which could expedite the process of developing CAVD treatment.

While these experiments have potentially exciting and significant results for CAVD patients, there is still substantial work needed to verify these results, first in a 3D or animal model system. Better understanding of the mineralization progression could be obtained by using more frequent imaging time points, or even time-lapse imaging of calcific nodules forming. In addition to visualization methods, transcriptomic data methods could provide an even clearer picture of all the molecular players involved with this pathway, potentially pointing out other drug targets. Further application of the systems and tools developed during the course of this study is discussed in the next

chapters of this thesis. Immediate future studies surrounding the role of the ECM in CAVD could take advantage of this work to advance our understanding of CAVD.

6.1.2 Knockdown of pRb Leads to Valve Regurgitation – A Potential Model for CAVD

In a collaborative effort with Tufts Medical Center, the creation and testing of a mouse model of conditional retinoblastoma protein (pRb) knockout (cKO) in the aortic valve regulated by Tie2-Cre-mediated excision of floxed RB1 alleles is explored. For these studies, mice that were homozygous for RB1^{fl/fl} and heterozygous for the Tie2-Cre transgene are designated as the conditional knockout mice (pRb cKO) while RB1^{+fl};Tie2-Cre⁺ were used for the control (pRb het). Using echocardiography, it was determined that pRb cKO mice had more aortic regurgitation than the pRb het mice and that cKO leaflets showed other signs of advancing CAVD such as increased leaflet thickness and stiffness and ECM disorganization. The pRb cKO valve tissue also stained higher, at several time points, for α SMA, indicating increased VIC activation with decreasing pRb.

In addition to differences in cell response, significant changes in the ECM were measured between pRb cKO and control mice. SHG imaging of collagen revealed that pRb cKO mice had less fiber organization than control mice and measured a higher Young's Modulus by AFM – both characteristics of diseased aortic valves. Principle component analysis of proteomics data showed distinct differences in the ECM composition between the two mice groups, again highlighting the importance that ECM likely has in CAVD. An increase in cytokine expression was also measured in pRb cKO over het mice, including the pro-inflammatory cytokine IL-17. MAF imaging showed an increased mineralization signal in pRb cKO mice compared to pRb het mice and, finally, further studies using

porcine VICs transfected to knockout pRb showed increased mineralization *in vitro* over control cells (**Figure 3.3** and **Figure 6.1**).

While this animal model shows promise as a means of studying CAVD, there is still further analysis that is needed. As noted, the conditional knockout of pRb was achieved through the use of a Tie2-Cre system. However, it was not confirmed that the changes seen in the pRb cKO mice valves were from knockdown of pRb in the valves only, as opposed to a general lack of pRb in other parts of the body. Future studies with these mice would first need to fill in such gaps before the mice could then be used a model of CAVD. Studies looking at hyaluronic acid and CD44 as well as specific ECM proteins could also be accomplished. As seen in **Figure 3.6**, specific ECM components are altered in this model. In the loading scores plot (**Figure 3.6 C**), there are several ECM proteins that vary with specific functional measurements, suggesting that these proteins could also be studied as a way to better understand valve leaflet stiffening and the loss of collagen fiber organization with CAVD progression.

6.1.3 The Development of a Non-Destructive Imaging Approach to Better Visualize Mineralization

This work describes the development of a novel imaging approach that non-destructively quantifies mineralization by taking advantage of the endogenous fluorescence found in calcific nodules. Spectral analysis was done on various samples to assess signals from mineralization, including human CAVD valves, rat bone, and calcific nodules grown *in vitro*. Spectra were collected on all of the samples before the tissue samples were demineralized with EDTA and imaged again. This analysis described the signal by a two-component model, with one component that could be further isolated through the use

of filters to define calcification in the samples (**Figure 4.4**). A fully refined approach to collecting and processing the mineralization associated fluorescence (MAF) was developed and used to look at mineralization levels in two model systems.

A common animal model of CAVD is knockout apolipoprotein E (ApoE) mice fed a high fat diet. For this chapter, ApoE^{-/-} mouse hearts were received and the aortic valve leaflets were isolated for imaging. Compared to aortic valve leaflets of healthy mice, ApoE^{-/-} mouse leaflets had increased MAF signal indicating increased mineralization. MAF was also used to study the formation and growth of calcific nodules in an *in vitro* model. In this study, VICs were allowed to calcify on a physiologically stiff 2D substrate after being stimulated with TGF- β_1 . Time lapse imaging that collected the MAF signal showed significant heterogeneity in nodule growth. Growth rate was varied across all of the nodules and one nodule even had an overall decrease in volume over the five-day experiment (**Figure 4.8**). These experiments highlight both how much there is still to learn surrounding CAVD and calcification and how MAF could be a valuable tool in helping to better understand mineralization.

While this non-linear microscopy imaging approach has clear advantages when looking at samples *ex vivo*, there are still many limitations and opportunities for improvement. For example, the development of optical probes capable of handling non-linear signal would be necessary to use this technique *in vivo*, though it would be considered invasive with the use of a catheter. However, with the development of this type of probe, other non-linear techniques, such as SHG, could be employed to provide additional information about the ECM of valve tissue (and other organs of the body). Additionally, while this *in vivo* probe technology is being improved, this system could also be used to track

mineralization during *in vitro* growth. A significant strength of this imaging approach is its intrinsic non-destructive capabilities. Watching calcification develop and being able to track ECM and cellular changes surrounding nodule formation could provide valuable insight into the mechanisms surrounding mineralization in systems like tooth tissue engineering and understanding soft tissue calcification.

6.1.4 High Throughput Screening and Testing of ECM Proteins that Change in CAVD

Recent advancements in RNA and DNA sequencing technology has led to a plethora of new data and ways to study development and disease. To build on the results from the 2D PAAM gel model and the pRb cKO knockout model, a 3D model system was developed using methacrylated HA. By leveraging non-destructive imaging techniques like MAF and SHG, this new system has the advantage of being able to monitor various conditions and changes to ECM components simultaneously. Using existing RNA-sequencing (RNA-seq) data and network analysis software, ECM proteins that were either up or down regulated in CAVD and highly connected (determined with network analysis) with multiple other ECM proteins were identified. While the work on this system and set of experiments is still on-going, initial data suggests that MeHA gels of physiologically relevant stiffnesses can be created and that non-linear microscopy imaging the MeHA gels can provide data on mineralization and the metabolic states of the VICs.

ECM proteins identified by RNA-seq for further testing can be bulk incorporated into MeHa gels. This sets up an easy, repeatable system to collect MAF, SHG, and redox ratio signal that can be monitored over time through the use of the non-destructive imaging techniques. The ECM proteins found through the RNA-seq analysis, including but not limited to decorin, collagen IV, periostin, aggrecan, and fibrinogen can be incorporated

into the gels with VICs during MeHA cross-linking. By studying both the bulk reaction and mineralization of each 3D gel along with the individual reactions of VICs, a clearer picture of the effect of each of these ECM components on CAVD can be ascertained.

The results of this study could simply further our understanding of CAVD and the changes that occur in aortic leaflet ECM or they may result in a potentially more significant finding of a mechanistic approach that could pave the way for pharmaceutical intervention in CAVD. RNA-seq could also be beneficial in understanding more about the pRb cKO mouse model and about how cells differ with valve stenosis. The use of large transcriptomic data sets to direct benchtop research is a relatively new endeavor that has not fully been explored. These experiments and the ones that follow may help to rapidly increase the rate of new discoveries and the understanding of disease mechanisms to hopefully help patients afflicted with CAVD and other diseases.

6.2 Future Directions

6.2.1 Using Previous Findings and Imaging Techniques to Investigate the Role of pRb

Another area to further explore is pRb's role in mineralization through OPN and CD44 – two molecules that were identified as important in *in vitro* mineralization in Chapter 2. In addition to the roles of pRb discussed here and its known role in cell cycle repression, pRb has also been implicated in cell adhesion and cell-to-cell contacts.²⁸² RB^{-/-} mice have been shown to express early markers of osteogenesis, such as an increase in OPN, but do not show an increase in late stage markers.²⁸³ In normal bone development, late maturation markers, such as Bglap, are expressed specifically when runx2 becomes downregulated, so a loss of mature bone in RB^{-/-} mice is not surprising. Typically, the retinoblastoma binding protein-1 transcription factor, a known coactivator of runx2,²⁸⁴ links to the p204

protein to activate runx2.²⁸⁵ In our cKO pRb mice, the Tie2-cre mediated the loss of pRb to primarily endothelial cells, so that we could study the role of pRb in mineralization in soft tissues, outside of normal bone development.

Although there are known links of the retinoblastoma protein's role in mineralization, the majority of studies involving pRb are done in the context of the loss of pRb leading to cancer. In tumors caused by the loss of pRb, there has been a measured increase in CD44 expression which is attributed to the cells becoming more cancer-like.²⁸⁶ Another interesting aspect of cancer cells is that OPN has been shown to promote cancer cell characteristics, acting through CD44.²⁸⁷ Furthermore, there is a known relationship between OPN and CD44, where OPN promotes the production of CD44²⁸⁸. Finally, the bone morphogenetic protein 2 (BMP-2) may act as a potential link between Rb and CD44, acting through the PI3K/AKT pathway to downregulate Rb and increasing CD44 expression through a SMAD-mediating link.²⁸⁹ All of these pathways are summarized in

Figure 6.2.

Taking these data into consideration, it is possible that the Tie2+ endothelial cells in the pRb cKO mice caused changes in the aortic valve microenvironment. Since the loss of Rb can lead to less cell adhesion, this could cause VECs to migrate into the valve leaflets. IN valve development, EndoMT is responsible for the original formation of VICs, so the loss of Rb could convert VECs to VICs. Since these new VICs would already be activated and primed to alter the leaflet ECM, these transformed VECs may be responsible for change in organization and ECM composition seen in the cKO pRb mice. The altered valve microenvironment could then kick off a positive feedback loop leading to increase

calcification and matrix remodeling, leading to a potential HA-CD44 based calcification pathway.

To further examine the role of these factors in CAVD, we may be able to use an imaging probe developed to use our MAF technique *in vivo*. The probe would be able to quantify mineralization and changes to some ECM proteins such as collagen and elastin, providing a real time analysis to the changes in the aortic valve. In addition to monitoring disease induced changes in the valve, the probe could also track the effectiveness of potential pharmaceutical intervention methods. To test the hypothesis of loss-of-pRb- transformed VECs beginning CAVD through ECM manipulation, we could first test a drug designed to block CD44. Using the probe, we could monitor the changes to the ECM, but also evaluate if blocking CD44 effectively stops mineralization of the valve even with matrix reorganization.

6.2.2 How Collagen Crosslinking Can Influence CAVD

In patients with normal aortic valve anatomy, CAVD is a disease that occurs during advanced age (>60 years old).²⁹⁰ While there are many factors, known and unknown, that can influence CAVD, it is generally agreed that CAVD starts (or is first diagnosed) when fibrotic thickening in the fibrosa and spongiosa layers of leaflets leads to stenosis of the valve.⁷ If the disease progresses to calcification of the tissue, nearly all mineralization starts in the collagen I dominated fibrosa layer of the leaflet. Fibrosis and excess collagen deposition is not a malady solely of the valve tissue and can occur, for various reasons, in soft tissue throughout the body. Fibrosis is defined by an overgrowth of collagen and a hardening of the tissue that is partially caused by an increase in collagen crosslinking.²⁹¹

In recent years, collagen crosslinking has become important to the study of many diseases throughout the body,²⁹² and may play a role in CAVD.

Healthy collagen crosslinking is mediated by the enzyme lysyl oxidase (LOX). LOX acts on either lysine or hydroxylysine regions of collagen fibrils, creating divalent, immature collagen crosslinks that eventually spontaneously form mature, trivalent links.²⁹³ These connections help collagen provide structural support and function to each tissue and prevent collagen slippage and damage.²⁹² However, tissues rich in collagen, such as connective tissue, and even porcine non-CAVD valve tissue, have been shown to increase in stiffness with age.^{294,295} These changes could be attributed to non-enzymatic reactions caused by an oxidative reaction between collagen and glucose, creating advanced glycation end-products (AGEs).²⁹⁶ AGEs can accumulate in long lasting proteins with low turnover, such as collagen in the aortic valve, and have been shown to change the affinity of some proteoglycans to collagen I.²⁹⁷ It is possible that this may contribute to some of the age related shifts in GAG content seen in heart valves.⁵³ Additionally, diabetes mellitus is both a known risk factor for CAVD and, because of altered sugar metabolism, a recognized cause of AGE accumulation.²⁹⁸ Finally, the receptor for AGEs has also been identified as a marker for individuals with a bicuspid aortic valve,²⁹⁹ a significant risk factor for CAVD.

Mechanically, AGEs have been associated with both an increase in tissue stiffness and brittleness³⁰⁰ which presents an interesting suggestion as to how AGEs could contribute to CAVD: increased tissue modulus is known to activate VICs into myofibroblasts, but a more brittle tissue increases the propensity of small injuries to the valve tissue, further activating and maintaining myofibroblasts. In bone mineralization, there are conflicting

reports as to if an increase in AGEs promotes or inhibits mineralization, although higher AGEs tissue density is correlated with a decrease in bone quality, if not bone density.³⁰¹ AGEs have been shown to increase apoptosis of osteoblasts,³⁰² but also to inhibit osteoclast bone reabsorption,³⁰³ suggesting lower bone turnover which adversely affects bone quality.³⁰⁴ From a CAVD perspective, both an increase in cell apoptosis and a decrease in bone reabsorption could exacerbate disease progression.

It has also been shown that AGEs can increase calcification in the vascular system,³⁰⁵ suggesting that AGEs may also have a direct effect on valve mineralization; however, the mechanism for this is not yet understood. One hypothesis for how vascular and valve calcification could be occurring comes from looking at how AGEs can impact the development of Alzheimer's disease. In Alzheimer's disease, neuronal plaques form when proteins aggregate around nucleation sites, a process that can be significantly accelerated with AGEs.³⁰⁶ Similarly, a suggested hypothesis of how mineralization begins in vascular disease involves the aggregation of calcific microvesicles into larger, calcific nodules.³⁰⁷ Taken together, these data suggest that AGEs may play a role in both the initiation and progression of CAVD.

Imaging methods developed both at Tufts and by others show that signals from collagen crosslinks can be collected and quantified.^{308,309} These techniques, combined with the MAF imaging method developed in this thesis, may be able to capture the mineralization process and conclusively determine if AGEs play a role. Combined with the growing body of knowledge surrounding the impact of the ECM on the progression of CAVD, the study of AGEs and collagen crosslinking may improve understanding of the disease.

6.2.3 The Role of the Immune System in CAVD

While this thesis made strides in understanding some of the factors associated with CAVD, one area that warrants considerably more attention is the role of the immune system. Although there was some work with cytokine expression in the pRb cKO and het mice, the results from the RNA-sequencing network analysis indicated that the immune system in CAVD valves was significantly altered compared to normal valves. Studying the immune system in the context of CAVD is by no means a new idea;³¹⁰ however, the development of the model systems in this thesis may help in the understanding of how cytokines and other immunogenic factors influence the progression of CAVD.

VIC activation through the cytokine TGF- β_1 was used successfully in many experiments described in this work. The use of TGF- β_1 as an exacerbating factor was based on a working theory of CAVD that states that the activation of the immune system through an injury or some other perturbation to the valve leaflet creates a cascading positive feedback loop that drives continued remodeling and fibrosis of the valve tissue. Several factors of the innate immune system, including tumor necrosis factor alpha (TNF α)³¹¹ and interleukin 6 (IL-6),³¹² have been implicated in valve calcification. Interestingly, the pRb cKO mice, while showing several signs of valve disease, did not show differences in IL-6 levels, but did show a significant increase in IL-17, a cytokine typically associated with the adaptive immune system.³¹³ In the RNA-seq analysis described in Chapter 5, there were several genes with a gene ontology (GO) process description involving both IL-6 and IL-17 that were upregulated with CAVD. IL-6 has been shown to act with TGF- β_1 to promote the transcription of IL-17 in helper Th17 cells.³¹⁴ In the pRb cKO, the expected upregulation of TNF α occurred. However, even though the pRb knockdown cells responded to TGF- β_1 *in vitro*, there was paradoxically, no increase in IL-6, even with a significant increase in IL-17.

This leads to an interesting question that could be explored in both the pRb mouse model and the 3D MeHA model. An interesting future study, building on the hypothesis that the loss of Rb leads to VEC transformation, would be to see if IL-17 is part of the immune response to VEC EndMT. If there is some correlation, IL-17 may become an important biomarker to diagnosis CAVD. Furthermore, IL-17 has been associated with changes to the ECM protein composition, especially in the context of the tumor microenvironment,³¹⁵ and could be contributing to the pathological ECM remodeling occurring in cKO pRb mouse valve. Future experiments that focus on the role of IL-17, ECM remodeling, and the interaction with Rb^{-/-} cells may provide useful insight into CAVD progression as well as further avenues of pharmaceutical intervention.

Since one of the major findings of the pRb mouse study was the significant change in ECM protein composition and structure based on proteomic and imaging analysis, it makes sense to study immune response in the context of ECM proteins. The 3D model system is already set up to easily incorporate soluble factors to test the impact of aspects of the immune system on VIC mineralization with ECM. In particular, HA has already been shown to be an immune regulator³¹⁶ and to be involved in inflammation and wound response.³¹⁷ While the immediate next steps for the pRb cKO mouse model are to gain a better understand of the impacts on CAVD in particular, this model may prove to be insightful in understanding the role of parts of the immune system in valve stenosis. It could also include RNA-seq analysis of pRb cKO VICs to see how the knockout gene effects RNA translation.

The work in this thesis sets the stage, both in terms of avenues of study and the models and tools necessary for investigation, to further explore the multiple variables associated

with CAVD. The continued development of tools, such as transcriptomics mapping and analysis, will help paint a more holistic picture of all the players involved in disease. Additionally, the integration of the immune system as a variable in the already complex understanding of valve stenosis and CAVD is likely to be necessary to develop more effective treatment methods for CAVD. In conclusion, the progress and findings of this thesis may help move the understanding of CAVD forward, both in terms of the direct results and in terms of the potential for use of the developed tools in subsequent studies of valve disease.

6.3 Figures

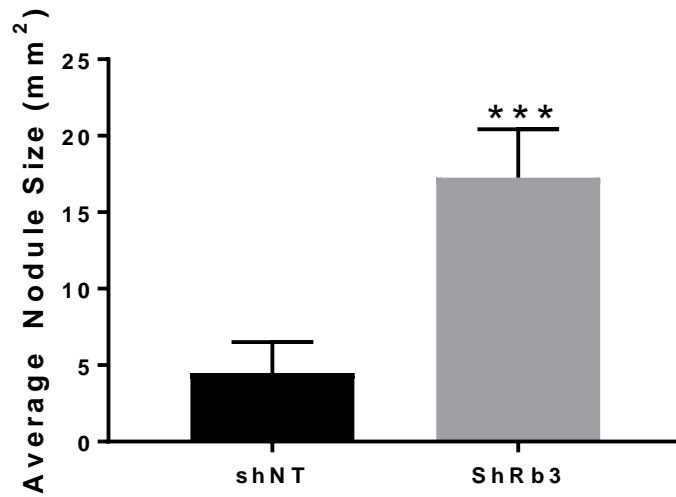


Figure 6.1: The average nodule size of nodules grown by transfected pVICs in culture.

After 15 days in culture, porcine VICs with Rb3 knockdown transfection showed more calcification than the control VICs (shNT) when grown on 5 kPa polyacrylamide gels with hyaluronic acid as the binding protein and simulated with TGF- β_1 . Mineralization was measured using the area of Alizarin Red staining fluorescence and a custom Matlab code. ***p<0.001

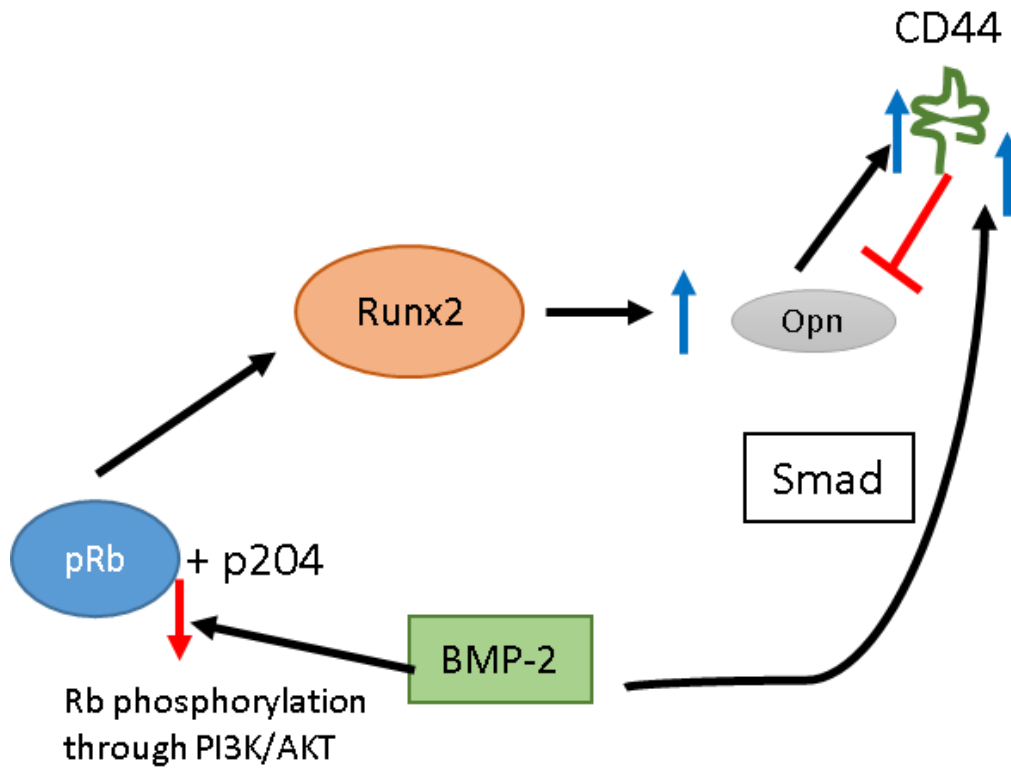


Figure 6.2: Schematic of known pathway links between molecules involved in mineralization.

pRb is a known coactivator, with p204, of Runx2. Runx2 upregulates OPN in normal bone development and OPN upregulates CD44, which has a feedback loop to block OPN. There is also a link between BMP-2 and pRb and CD44, where BMP-2 has been shown to decrease and increase the molecules, respectively.

Chapter 7. References

1. Rajamannan, N.M., *et al.* Calcific aortic valve disease: not simply a degenerative process. *Circulation* **124**, 1783-1791 (2011).
2. Mohler, E.R., *et al.* Bone Formation and Inflammation in Cardiac Valves. *Circulation* **103**, 1522-1528 (2001).
3. Go, A.S., *et al.* Heart disease and stroke statistics--2014 update: a report from the American Heart Association. *Circulation* **129**, e28-e292 (2014).
4. Nishimura, R.A., *et al.* 2014 AHA/ACC Guideline for the Management of Patients With Valvular Heart Disease: Executive Summary. *A Report of the American College of Cardiology/American Heart Association Task Force on Practice Guidelines* **129**(2014).
5. Leon, M.B., *et al.* Transcatheter or surgical aortic-valve replacement in intermediate-risk patients. *N Engl J Med* **2016**, 1609-1620 (2016).
6. Stewart, W.J., King, M.E., Gillam, L.D., Guyer, D.E. & Weyman, A.E. Prevalence of aortic valve prolapse with bicuspid aortic valve and its relation to aortic regurgitation: a cross-sectional echocardiographic study. *The American journal of cardiology* **54**, 1277-1282 (1984).
7. Freeman, R.V. & Otto, C.M. Spectrum of calcific aortic valve disease pathogenesis, disease progression, and treatment strategies. *Circulation* **111**, 3316-3326 (2005).
8. LaHaye, S., Lincoln, J. & Garg, V. Genetics of valvular heart disease. *Current cardiology reports* **16**, 487 (2014).
9. Hutcheson, J.D., Aikawa, E. & Merryman, W.D. Potential drug targets for calcific aortic valve disease. *Nature reviews. Cardiology* **11**, 218-231 (2014).
10. New, S.E.P. & Aikawa, E. Cardiovascular Calcification; An Inflammatory Disease. *Circulation Journal* **75**, 1305-1313 (2011).
11. Mizobuchi, M., Towler, D. & Slatopolsky, E. Vascular calcification: the killer of patients with chronic kidney disease. *Journal of the American Society of Nephrology* **20**, 1453-1464 (2009).
12. Cramariuc, D., *et al.* Sex differences in cardiovascular outcome during progression of aortic valve stenosis. *Heart*, heartjnl-2014-306078 (2014).

13. Porras, A.M., McCoy, C.M. & Masters, K.S. Calcific Aortic Valve Disease. (Am Heart Assoc, 2017).
14. Stella, J.A. & Sacks, M.S. On the Biaxial Mechanical Properties of the Layers of the Aortic Valve Leaflet. *Journal of Biomechanical Engineering* **129**, 757-766 (2007).
15. Rajamannan, N.M., *et al.* Calcific aortic valve disease: not simply a degenerative process: A review and agenda for research from the National Heart and Lung and Blood Institute Aortic Stenosis Working Group. Executive summary: Calcific aortic valve disease-2011 update. *Circulation* **124**, 1783-1791 (2011).
16. Schoen, F.J. Evolving concepts of cardiac valve dynamics. *Circulation* **118**, 1864-1880 (2008).
17. Schroeder, J.A., Jackson, L.F., Lee, D.C. & Camenisch, T.D. Form and function of developing heart valves: coordination by extracellular matrix and growth factor signaling. *Journal of molecular medicine* **81**, 392-403 (2003).
18. Combs, M.D. & Yutzey, K.E. Heart Valve Development. *Circulation research* **105**, 408-421 (2009).
19. Hinton, R.B., *et al.* Extracellular matrix remodeling and organization in developing and diseased aortic valves. *Circ Res* **98**, 1431-1438 (2006).
20. Kaden, J.J., *et al.* Inflammatory regulation of extracellular matrix remodeling in calcific aortic valve stenosis. *Cardiovascular Pathology* **14**, 80-87 (2005).
21. Mahler, G.J., Farrar, E.J. & Butcher, J.T. Inflammatory cytokines promote mesenchymal transformation in embryonic and adult valve endothelial cells. *Arteriosclerosis, thrombosis, and vascular biology* **33**, 121-130 (2013).
22. Chen, J.H. & Simmons, C.A. Cell-matrix interactions in the pathobiology of calcific aortic valve disease: critical roles for matricellular, matricrine, and matrix mechanics cues. *Circ Res* **108**, 1510-1524 (2011).
23. Jatene, M.B., *et al.* Aortic valve assessment. Anatomical study of 100 healthy human hearts. *Arquivos brasileiros de cardiologia* **73**, 81-86 (1999).
24. Taylor, P.M., Batten, P., Brand, N.J., Thomas, P.S. & Yacoub, M.H. The cardiac valve interstitial cell. *The international journal of biochemistry & cell biology* **35**, 113-118 (2003).
25. Miller, L.J. & Lincoln, J. Isolation of murine valve endothelial cells. *Journal of visualized experiments: JoVE* (2014).
26. Rabkin-Aikawa, E., Farber, M., Aikawa, M. & Schoen, F.J. Dynamic and reversible changes of interstitial cell phenotype during remodeling of cardiac valves. *Journal of Heart Valve Disease* **13**, 841-847 (2004).

27. Messier, R.H., *et al.* Dual structural and functional phenotypes of the porcine aortic valve interstitial population: characteristics of the leaflet myofibroblast. *Journal of Surgical Research* **57**, 1-21 (1994).
28. Imberti, B., Seliktar, D., Nerem, R. & Remuzzi, A. The response of endothelial cells to fluid shear stress using a co-culture model of the arterial wall. *Endothelium* **9**, 11-23 (2002).
29. Butcher, J.T. & Nerem, R.M. Valvular endothelial cells and the mechanoregulation of valvular pathology. *Philosophical Transactions of the Royal Society of London B: Biological Sciences* **362**, 1445-1457 (2007).
30. Bischoff, J. & Aikawa, E. Progenitor cells confer plasticity to cardiac valve endothelium. *Journal of cardiovascular translational research* **4**, 710-719 (2011).
31. Butcher, J.T. & Nerem, R.M. Valvular endothelial cells regulate the phenotype of interstitial cells in co-culture: effects of steady shear stress. *Tissue engineering* **12**, 905-915 (2006).
32. MuÈller, A.M., *et al.* Expression of endothelial cell adhesion molecules on heart valves: up-regulation in degeneration as well as acute endocarditis. *The Journal of pathology* **191**, 54-60 (2000).
33. Piera-Velazquez, S., Li, Z. & Jimenez, S.A. Role of endothelial-mesenchymal transition (EndoMT) in the pathogenesis of fibrotic disorders. *The American journal of pathology* **179**, 1074-1080 (2011).
34. Rajamannan, N.M. *Molecular Biology of Valvular Heart Disease*, (Springer Science & Business, 2014).
35. GINGHINĂ¹, C., *et al.* Calcific Aortic Valve Disease and Aortic Atherosclerosis—Two Faces of the Same Disease? *ROM. J. INTERN. MED* **47**, 319-329 (2009).
36. Aikawa, E., *et al.* Osteogenesis associates with inflammation in early-stage atherosclerosis evaluated by molecular imaging in vivo. *Circulation* **116**, 2841-2850 (2007).
37. Liu, A.C., Joag, V.R. & Gotlieb, A.I. The emerging role of valve interstitial cell phenotypes in regulating heart valve pathobiology. *The American journal of pathology* **171**, 1407-1418 (2007).
38. Pho, M., *et al.* *Cofilin is a marker of myofibroblast differentiation in cells from porcine aortic cardiac valves*, (2008).
39. Merryman, W.D., *et al.* Differences in tissue-remodeling potential of aortic and pulmonary heart valve interstitial cells. *Tissue engineering* **13**, 2281-2289 (2007).

40. Merryman, W.D., *et al.* Correlation between heart valve interstitial cell stiffness and transvalvular pressure: implications for collagen biosynthesis. *American Journal of Physiology-Heart and Circulatory Physiology* **290**, H224-H231 (2006).
41. Tamura, K., Jones, M., Yamada, I. & Ferrans, V. Wound healing in the mitral valve. *The Journal of heart valve disease* **9**, 53-63 (2000).
42. Durbin, A.D. & Gotlieb, A.I. Advances towards understanding heart valve response to injury. *Cardiovascular Pathology* **11**, 69-77 (2002).
43. Christoph J. Engelbrecht, R.S.J., Eric J. Seibel, Fritjof Helmchen. <Powell - 2000 - Myofibroblasts paracrine cells important in health and disease.pdf>. *Optics Express* (2008).
44. Rabkin, E., *et al.* Activated interstitial myofibroblasts express catabolic enzymes and mediate matrix remodeling in myxomatous heart valves. *Circulation* **104**, 2525-2532 (2001).
45. Hinz, B. The myofibroblast: paradigm for a mechanically active cell. *Journal of biomechanics* **43**, 146-155 (2010).
46. Hinz, B., *et al.* Recent developments in myofibroblast biology: paradigms for connective tissue remodeling. *The American journal of pathology* **180**, 1340-1355 (2012).
47. Quinlan, A.M. & Billiar, K.L. Investigating the role of substrate stiffness in the persistence of valvular interstitial cell activation. *Journal of biomedical materials research. Part A* **100**, 2474-2482 (2012).
48. Rajamannan, N.M., *et al.* Human aortic valve calcification is associated with an osteoblast phenotype. *Circulation* **107**, 2181-2184 (2003).
49. Boström, K.I., Rajamannan, N.M. & Towler, D.A. The regulation of valvular and vascular sclerosis by osteogenic morphogens. *Circulation research* **109**, 564-577 (2011).
50. Hutcheson, J.D., *et al.* Cadherin-11 Regulates Cell–Cell Tension Necessary for Calcific Nodule Formation by Valvular Myofibroblasts. *Arteriosclerosis, thrombosis, and vascular biology* **33**, 114-120 (2013).
51. Towler, D.A. Molecular and cellular aspects of calcific aortic valve disease. *Circulation research* **113**, 198-208 (2013).
52. Garg, V., *et al.* Mutations in NOTCH1 cause aortic valve disease. *Nature* **437**, 270-274 (2005).
53. Stephens, E.H., Chu, C.K. & Grande-Allen, K.J. Valve proteoglycan content and glycosaminoglycan fine structure are unique to microstructure, mechanical load

- and age: Relevance to an age-specific tissue-engineered heart valve. *Acta Biomater* **4**, 1148-1160 (2008).
54. Egan, K.P., Kim, J.H., Mohler, E.R. & Pignolo, R.J. Role for circulating osteogenic precursor cells in aortic valvular disease. *Arterioscler Thromb Vasc Biol* **31**, 2965-2971 (2011).
 55. Rutkovskiy, A., *et al.* Valve Interstitial Cells: The Key to Understanding the Pathophysiology of Heart Valve Calcification. *J Am Heart Assoc* **6**(2017).
 56. Kim, S.-H., Turnbull, J. & Guimond, S. Extracellular matrix and cell signalling: the dynamic cooperation of integrin, proteoglycan and growth factor receptor. *Journal of Endocrinology* **209**, 139-151 (2011).
 57. Aikawa, E., *et al.* Human Semilunar Cardiac Valve Remodeling by Activated Cells From Fetus to Adult Implications for Postnatal Adaptation, Pathology, and Tissue Engineering. *Circulation* **113**, 1344-1352 (2006).
 58. Balaoing, L.R., Post, A.D., Liu, H., Minn, K.T. & Grande-Allen, K.J. Age-related changes in aortic valve hemostatic protein regulation. *Arteriosclerosis, thrombosis, and vascular biology* **34**, 72-80 (2014).
 59. Rosenhek, R., *et al.* Mild and moderate aortic stenosis: natural history and risk stratification by echocardiography. *European Heart Journal* **25**, 199-205 (2004).
 60. Hutson, H.N., *et al.* Calcific Aortic Valve Disease Is Associated with Layer-Specific Alterations in Collagen Architecture. *PLoS One* **11**, e0163858 (2016).
 61. Yip, C.Y. & Simmons, C.A. The aortic valve microenvironment and its role in calcific aortic valve disease. *Cardiovascular pathology : the official journal of the Society for Cardiovascular Pathology* **20**, 177-182 (2011).
 62. Desmoulière, A., Badid, C., Bochaton-Piallat, M.-L. & Gabbiani, G. Apoptosis during wound healing, fibrocontractive diseases and vascular wall injury. *The international journal of biochemistry & cell biology* **29**, 19-30 (1997).
 63. Otto, C.M., Kuusisto, J., Reichenbach, D.D., Gown, A.M. & O'brien, K.D. Characterization of the early lesion of degenerative valvular aortic stenosis. Histological and immunohistochemical studies. *Circulation* **90**, 844-853 (1994).
 64. Rodriguez, K.J., Piechura, L.M. & Masters, K.S. Regulation of valvular interstitial cell phenotype and function by hyaluronic acid in 2-D and 3-D culture environments. *Matrix Biology* **30**, 70-82 (2011).
 65. Stephens, E.H., *et al.* Differential proteoglycan and hyaluronan distribution in calcified aortic valves. *Cardiovascular Pathology* **20**, 334-342 (2011).

66. Bernauer, W., *et al.* Corneal calcification following intensified treatment with sodium hyaluronate artificial tears. *British journal of ophthalmology* **90**, 285-288 (2006).
67. Andrews, J.P. & Dweck, M.R. Early detection of valvular calcification. *Nature Biomedical Engineering* **1**, 860 (2017).
68. Sider, K.L., Blaser, M.C. & Simmons, C.A. Animal Models of Calcific Aortic Valve Disease. *International Journal of Inflammation* **2011**, 364310 (2011).
69. Walker, G.A., Masters, K.S., Shah, D.N., Anseth, K.S. & Leinwand, L.A. Valvular myofibroblast activation by transforming growth factor-beta: implications for pathological extracellular matrix remodeling in heart valve disease. *Circ Res* **95**, 253-260 (2004).
70. Hjortnaes, J., *et al.* Simulation of early calcific aortic valve disease in a 3D platform: a role for myofibroblast differentiation. *Journal of molecular and cellular cardiology* **94**, 13-20 (2016).
71. van der Ven, C.F., *et al.* In vitro 3D model and miRNA drug delivery to target calcific aortic valve disease. *Clinical Science* **131**, 181-195 (2017).
72. Cirka, H.A., Uribe, J., Liang, V., Schoen, F.J. & Billiar, K.L. Reproducible in vitro model for dystrophic calcification of cardiac valvular interstitial cells: insights into the mechanisms of calcific aortic valvular disease. *Lab on a Chip* **17**, 814-829 (2017).
73. Mehrabian, M., Demer, L.L. & Lusis, A.J. Differential accumulation of intimal monocyte-macrophages relative to lipoproteins and lipofuscin corresponds to hemodynamic forces on cardiac valves in mice. *Arteriosclerosis, thrombosis, and vascular biology* **11**, 947-957 (1991).
74. Wexler, L., *et al.* Coronary Artery Calcification: Pathophysiology, Epidemiology, Imaging Methods, and Clinical Implications: A Statement for Health Professionals From the American Heart Association. *Circulation* **94**, 1175-1192 (1996).
75. Linefsky, J. & Otto, C. Ultrasound Imaging of Calcific Aortic Valve Disease. in *Cardiovascular Imaging* (ed. Aikawa, E.) 225-249 (Springer International Publishing, 2015).
76. Fuster, V., *et al.* Atherothrombosis and High-Risk Plaque: Part II: Approaches by Noninvasive Computed Tomographic/Magnetic Resonance Imaging. *Journal of the American College of Cardiology* **46**, 1209-1218 (2005).
77. New, S.E.P. & Aikawa, E. Molecular Imaging Insights into Early Inflammatory Stages of Arterial and Aortic Valve Calcification. *Circulation research* **108**, 1381-1391 (2011).

78. König, K., Schenke-Layland, K., Riemann, I. & Stock, U.A. Multiphoton autofluorescence imaging of intratissue elastic fibers. *Biomaterials* **26**, 495-500 (2005).
79. Alavi, S.H., Ruiz, V., Krasieva, T., Botvinick, E.L. & Kheradvar, A. Characterizing the collagen fiber orientation in pericardial leaflets under mechanical loading conditions. *Ann Biomed Eng* **41**, 547-561 (2013).
80. Gerson, C.J., Goldstein, S. & Heacock, A.E. Retained structural integrity of collagen and elastin within cryopreserved human heart valve tissue as detected by two-photon laser scanning confocal microscopy. *Cryobiology* **59**, 171-179 (2009).
81. Kherlopian, A., *et al.* A review of imaging techniques for systems biology. *BMC Systems Biology* **2**, 74 (2008).
82. Ballyns, J.J. & Bonassar, L.J. Image-guided tissue engineering. *Journal of cellular and molecular medicine* **13**, 1428-1436 (2009).
83. Bertazzo, S., *et al.* Nano-analytical electron microscopy reveals fundamental insights into human cardiovascular tissue calcification. *Nat Mater* **12**, 576-583 (2013).
84. Feuchtner, G. Imaging of cardiac valves by computed tomography. *Scientifica* **2013**(2013).
85. Dweck, M.R., *et al.* Assessment of valvular calcification and inflammation by positron emission tomography in patients with aortic stenosis. *Circulation*, CIRCULATIONAHA.111.051052 (2011).
86. Jenkins, W.S., *et al.* Valvular ¹⁸F-Fluoride and ¹⁸F-Fluorodeoxyglucose Uptake Predict Disease Progression and Clinical Outcome in Patients With Aortic Stenosis. *Journal of the American College of Cardiology* **66**, 1200-1201 (2015).
87. Goo, H.W. CT Radiation Dose Optimization and Estimation: an Update for Radiologists. *Korean J Radiol* **13**, 1-11 (2012).
88. Jaffer, F.A., Libby, P. & Weissleder, R. Optical and Multimodality Molecular Imaging: Insights Into Atherosclerosis. *Arteriosclerosis, Thrombosis, and Vascular Biology* **29**, 1017-1024 (2009).
89. Hjortnaes, J., *et al.* Arterial and aortic valve calcification inversely correlates with osteoporotic bone remodelling: a role for inflammation. *European heart journal* **31**, 1975-1984 (2010).
90. Lindroos, M., Kupari, M., Heikkilä, J. & Tilvis, R. Prevalence of aortic valve abnormalities in the elderly: an echocardiographic study of a random population sample. *J Am Coll Cardiol* **21**, 1220-1225 (1993).

91. Freeman, R.V. & Otto, C.M. Spectrum of calcific aortic valve disease: pathogenesis, disease progression, and treatment strategies. *Circulation* **111**, 3316-3326 (2005).
92. Leopold, J.A. Cellular mechanisms of aortic valve calcification. *Circulation: Cardiovascular Interventions* **5**, 605-614 (2012).
93. Kim, Y. & Kumar, S. CD44-mediated adhesion to hyaluronic acid contributes to mechanosensing and invasive motility. *Molecular Cancer Research* **12**, 1416-1429 (2014).
94. Ohri, R., Hahn, S.K., Hoffman, A.S., Stayton, P.S. & Giachelli, C.M. Hyaluronic acid grafting mitigates calcification of glutaraldehyde-fixed bovine pericardium. *Journal of Biomedical Materials Research Part A* **70**, 328-334 (2004).
95. Liu, H., Sun, Y. & Simmons, C.A. Determination of local and global elastic moduli of valve interstitial cells cultured on soft substrates. *Journal of biomechanics* **46**, 1967-1971 (2013).
96. Throm Quinlan, A.M., Sierad, L.N., Capulli, A.K., Firstenberg, L.E. & Billiar, K.L. Combining dynamic stretch and tunable stiffness to probe cell mechanobiology in vitro. *PLoS One* **6**, e23272 (2011).
97. Yang, B., Yang, B.L., Savani, R.C. & Turley, E.A. Identification of a common hyaluronan binding motif in the hyaluronan binding proteins RHAMM, CD44 and link protein. *The EMBO Journal* **13**, 286-296 (1994).
98. Krupinski, J., *et al.* Changes in hyaluronan metabolism and RHAMM receptor expression accompany formation of complicated carotid lesions and may be pro-angiogenic mediators of intimal neovessel growth. *Biomarker insights* **2**, 361 (2007).
99. Cuff, C.A., *et al.* The adhesion receptor CD44 promotes atherosclerosis by mediating inflammatory cell recruitment and vascular cell activation. *The Journal of clinical investigation* **108**, 1031-1040 (2001).
100. Agmon, Y., *et al.* Aortic valve sclerosis and aortic atherosclerosis: different manifestations of the same disease?: Insights from a population-based study. *Journal of the American College of Cardiology* **38**, 827-834 (2001).
101. Wang, Y.-L. & Pelham Jr, R.J. [39] Preparation of a flexible, porous polyacrylamide substrate for mechanical studies of cultured cells. in *Methods in Enzymology*, Vol. Volume 298 (ed. Richard, B.V.) 489-496 (Academic Press, 1998).
102. Chen, J.-H., Chen, W.L.K., Sider, K.L., Yip, C.Y.Y. & Simmons, C.A. β -catenin mediates mechanically regulated, transforming growth factor- β 1-induced myofibroblast differentiation of aortic valve interstitial cells. *Arteriosclerosis, thrombosis, and vascular biology* **31**, 590-597 (2011).

103. Chen, H., Cui, W., Hu, H. & Liu, J. Isolation and culture of rat aortic valve interstitial cells. *Anatol J Cardiol* **15**, 893-896 (2015).
104. Guatimosim, S., Guatimosim, C. & Song, L.S. Imaging calcium sparks in cardiac myocytes. *Methods in molecular biology* **689**, 205-214 (2011).
105. Guatimosim, S., Guatimosim, C. & Song, L.-S. Imaging calcium sparks in cardiac myocytes. *Light Microscopy: Methods and Protocols*, 205-214 (2011).
106. Schneider, C.A., Rasband, W.S. & Eliceiri, K.W. NIH Image to ImageJ: 25 years of image analysis. *Nature methods* **9**, 671-675 (2012).
107. Carpenter, A.E., *et al.* CellProfiler: image analysis software for identifying and quantifying cell phenotypes. *Genome biology* **7**, R100 (2006).
108. Califano, J.P. & Reinhart-King, C.A. Substrate stiffness and cell area predict cellular traction stresses in single cells and cells in contact. *Cellular and molecular bioengineering* **3**, 68-75 (2010).
109. Tee, S.-Y., Fu, J., Chen, C.S. & Janmey, P.A. Cell shape and substrate rigidity both regulate cell stiffness. *Biophysical journal* **100**, L25-L27 (2011).
110. Lesley, J., Hascall, V.C., Tammi, M. & Hyman, R. Hyaluronan binding by cell surface CD44. *The Journal of Biological Chemistry* **275**, 26967-26975 (2000).
111. Zhu, D., Mackenzie, N.C.W., Millán, J.L., Farquharson, C. & MacRae, V.E. The appearance and modulation of osteocyte marker expression during calcification of vascular smooth muscle cells. *PloS one* **6**, e19595 (2011).
112. Rittling, S.R., *et al.* Mice lacking osteopontin show normal development and bone structure but display altered osteoclast formation in vitro. *Journal of Bone and Mineral Research* **13**, 1101-1111 (1998).
113. Wada, T., McKee, M.D., Steitz, S. & Giachelli, C.M. Calcification of Vascular Smooth Muscle Cell Cultures. *Inhibition by Osteopontin* **84**, 166-178 (1999).
114. (!!! INVALID CITATION !!!).
115. Kohan, M., Breuer, R. & Berkman, N. Osteopontin induces airway remodeling and lung fibroblast activation in a murine model of asthma. *American journal of respiratory cell and molecular biology* **41**, 290-296 (2009).
116. Talley-Ronsholdt, D.J., Lajiness, E. & Nagodawithana, K. Transforming growth factor-beta inhibition of mineralization by neonatal rat osteoblasts in monolayer and collagen gel culture. *In Vitro Cellular & Developmental Biology-Animal* **31**, 274-282 (1995).
117. Midgley, A.C., *et al.* Transforming growth factor- β 1 (TGF- β 1)-stimulated fibroblast to myofibroblast differentiation is mediated by hyaluronan (HA)-

- facilitated epidermal growth factor receptor (EGFR) and CD44 co-localization in lipid rafts. *Journal of Biological Chemistry* **288**, 14824-14838 (2013).
118. Kahles, F., Findeisen, H.M. & Bruemmer, D. Osteopontin: A novel regulator at the cross roads of inflammation, obesity and diabetes. *Molecular metabolism* **3**, 384-393 (2014).
 119. Zhang, F.-J., *et al.* The effect of hyaluronic acid on osteopontin and CD44 mRNA of fibroblast-like synoviocytes in patients with osteoarthritis of the knee. *Rheumatology international* **33**, 79-83 (2013).
 120. Stephens, E.H., *et al.* Differential proteoglycan and hyaluronan distribution in calcified aortic valves. *Cardiovascular pathology : the official journal of the Society for Cardiovascular Pathology* **20**, 334-342 (2011).
 121. Grande-Allen, K.J., *et al.* Glycosaminoglycan synthesis and structure as targets for the prevention of calcific aortic valve disease. *Cardiovascular research* **76**, 19-28 (2007).
 122. Denhardt, D.T. & Guo, X. Osteopontin: a protein with diverse functions. *The FASEB journal* **7**, 1475-1482 (1993).
 123. Hao, C., *et al.* Human osteopontin: Potential clinical applications in cancer. *International Journal of Molecular Medicine* **39**, 1327-1337 (2017).
 124. Canella, A., *et al.* HDAC inhibitor AR-42 decreases CD44 expression and sensitizes myeloma cells to lenalidomide. *Oncotarget* **6**, 31134 (2015).
 125. Paranya, G., *et al.* Aortic valve endothelial cells undergo transforming growth factor- β -mediated and non-transforming growth factor- β -mediated transdifferentiation in vitro. *The American journal of pathology* **159**, 1335-1343 (2001).
 126. Zhao, L., *et al.* CD44 regulates vascular gene expression in a proatherogenic environment. *Arteriosclerosis, thrombosis, and vascular biology* **27**, 886-892 (2007).
 127. Freytsis, M., *et al.* Conditional deletion of RB1 in the Tie2 lineage leads to aortic valve regurgitation. *PLOS ONE* **13**, e0190623 (2018).
 128. Benjamin, E.J., *et al.* Heart Disease and Stroke Statistics-2017 Update: A Report From the American Heart Association. *Circulation* **135**, e146-e603 (2017).
 129. Nkomo, V.T., *et al.* Burden of valvular heart diseases: a population-based study. *Lancet* **368**, 1005-1011 (2006).
 130. Chan, K.L., *et al.* Effect of Lipid lowering with rosuvastatin on progression of aortic stenosis: results of the aortic stenosis progression observation: measuring effects of rosuvastatin (ASTRONOMER) trial. *Circulation* **121**, 306-314 (2010).

131. Rossebo, A.B., *et al.* Intensive lipid lowering with simvastatin and ezetimibe in aortic stenosis. *N Engl J Med* **359**, 1343-1356 (2008).
132. Lincoln, J., Alfieri, C.M. & Yutzey, K.E. Development of heart valve leaflets and supporting apparatus in chicken and mouse embryos. *Dev Dyn* **230**, 239-250 (2004).
133. Butcher, J.T. & Markwald, R.R. Valvulogenesis: the moving target. *Philos Trans R Soc Lond B Biol Sci* **362**, 1489-1503 (2007).
134. de Lange, F.J., *et al.* Lineage and morphogenetic analysis of the cardiac valves. *Circ Res* **95**, 645-654 (2004).
135. Gomez-Stallons, M.V., Wirrig-Schwendeman, E.E., Hassel, K.R., Conway, S.J. & Yutzey, K.E. Bone Morphogenetic Protein Signaling Is Required for Aortic Valve Calcification. *Arterioscler Thromb Vasc Biol* **36**, 1398-1405 (2016).
136. Kisanuki, Y.Y., *et al.* Tie2-Cre transgenic mice: a new model for endothelial cell-lineage analysis in vivo. *Dev Biol* **230**, 230-242 (2001).
137. Anstine, L.J., Horne, T.E., Horwitz, E.M. & Lincoln, J. Contribution of Extra-Cardiac Cells in Murine Heart Valves is Age-Dependent. *Journal of American Heart Association*, e007097 (2017).
138. Tang, Y., Harrington, A., Yang, X., Friesel, R.E. & Liaw, L. The contribution of the Tie2+ lineage to primitive and definitive hematopoietic cells. *Genesis* **48**, 563-567 (2010).
139. Rabkin-Aikawa, E., Farber, M., Aikawa, M. & Schoen, F.J. Dynamic and reversible changes of interstitial cell phenotype during remodeling of cardiac valves. *J Heart Valve Dis* **13**, 841-847 (2004).
140. Taylor, P.M., Batten, P., Brand, N.J., Thomas, P.S. & Yacoub, M.H. The cardiac valve interstitial cell. *Int J Biochem Cell Biol* **35**, 113-118 (2003).
141. Hammer, P.E., Pacak, C.A., Howe, R.D. & del Nido, P.J. Straightening of curved pattern of collagen fibers under load controls aortic valve shape. *J Biomech* **47**, 341-346 (2014).
142. Messier, R.H., *et al.* Dual structural and functional phenotypes of the porcine aortic valve interstitial population: characteristics of the leaflet myofibroblast. *J Surg Res* **57**, 1-21 (1994).
143. Stephens, E.H., *et al.* Extracellular matrix remodeling in wound healing of critical size defects in the mitral valve leaflet. *Heart Vessels* **31**, 1186-1195 (2016).
144. Rabkin, E., *et al.* Activated interstitial myofibroblasts express catabolic enzymes and mediate matrix remodeling in myxomatous heart valves. *Circulation* **104**, 2525-2532 (2001).

145. Krishnamurthy, V.K., Guilak, F., Narmoneva, D.A. & Hinton, R.B. Regional structure-function relationships in mouse aortic valve tissue. *Journal of biomechanics* **44**, 77-83 (2011).
146. Otto, C.M., Kuusisto, J., Reichenbach, D.D., Gown, A.M. & O'Brien, K.D. Characterization of the early lesion of 'degenerative' valvular aortic stenosis. Histological and immunohistochemical studies. *Circulation* **90**, 844-853 (1994).
147. Thomas, D.M., *et al.* The retinoblastoma protein acts as a transcriptional coactivator required for osteogenic differentiation. *Mol Cell* **8**, 303-316 (2001).
148. Gutierrez, G.M., *et al.* Impaired bone development and increased mesenchymal progenitor cells in calvaria of RB1-/- mice. *Proceedings of the National Academy of Sciences of the United States of America* **105**, 18402-18407 (2008).
149. Calo, E., *et al.* Rb regulates fate choice and lineage commitment in vivo. *Nature* **466**, 1110-1114 (2010).
150. Arima, Y., *et al.* Rb depletion results in deregulation of E-cadherin and induction of cellular phenotypic changes that are characteristic of the epithelial-to-mesenchymal transition. *Cancer Res* **68**, 5104-5112 (2008).
151. Lincoln, J., Kist, R., Scherer, G. & Yutzey, K.E. Sox9 is required for precursor cell expansion and extracellular matrix organization during mouse heart valve development. *Dev Biol* **305**, 120-132 (2007).
152. Casanovas, O., Hager, J.H., Chun, M.G. & Hanahan, D. Incomplete inhibition of the Rb tumor suppressor pathway in the context of inactivated p53 is sufficient for pancreatic islet tumorigenesis. *Oncogene* **24**, 6597-6604 (2005).
153. Carpenter, A.E., *et al.* CellProfiler: image analysis software for identifying and quantifying cell phenotypes. *Genome Biol* **7**, R100 (2006).
154. Baugh, L.M., *et al.* Non-destructive two-photon excited fluorescence imaging identifies early nodules in calcific aortic-valve disease. *Nature Biomedical Engineering* **1**, 914 (2017).
155. Quinn, K.P. & Georgakoudi, I. Rapid quantification of pixel-wise fiber orientation data in micrographs. *J Biomed Opt* **18**, 046003 (2013).
156. Qian, H.S., *et al.* Quantification and Comparison of Anti-Fibrotic Therapies by Polarized SRM and SHG-Based Morphometry in Rat UUO Model. *PLoS One* **11**, e0156734 (2016).
157. Williams, C., Quinn, K.P., Georgakoudi, I. & Black, L.D. Young developmental age cardiac extracellular matrix promotes the expansion of neonatal cardiomyocytes in vitro. *Acta Biomater* **10**, 194-204 (2014).

158. Nishimura, S., *et al.* Global gene expression analysis following spinal cord injury in non-human primates. *Exp Neurol* **261**, 171-179 (2014).
159. Agarwal, U., *et al.* Age-Dependent Effect of Pediatric Cardiac Progenitor Cells After Juvenile Heart Failure. *Stem Cells Transl Med* **5**, 883-892 (2016).
160. Launay, G., Salza, R., Multedo, D., Thierry-Mieg, N. & Ricard-Blum, S. MatrixDB, the extracellular matrix interaction database: updated content, a new navigator and expanded functionalities. *Nucleic Acids Res* **43**, D321-327 (2015).
161. Jacks, T., *et al.* Effects of an Rb mutation in the mouse. *Nature* **359**, 295-300 (1992).
162. Macleod, K.F. The role of the RB tumour suppressor pathway in oxidative stress responses in the haematopoietic system. *Nat Rev Cancer* **8**, 769-781 (2008).
163. Walkley, C.R., Shea, J.M., Sims, N.A., Purton, L.E. & Orkin, S.H. Rb regulates interactions between hematopoietic stem cells and their bone marrow microenvironment. *Cell* **129**, 1081-1095 (2007).
164. Weinberg, R.A. The retinoblastoma protein and cell cycle control. *Cell* **81**, 323-330 (1995).
165. Wirrig, E.E., Hinton, R.B. & Yutzey, K.E. Differential expression of cartilage and bone-related proteins in pediatric and adult diseased aortic valves. *J Mol Cell Cardiol* **50**, 561-569 (2011).
166. Miller, J.D., Weiss, R.M. & Heistad, D.D. Calcific aortic valve stenosis: methods, models, and mechanisms. *Circ Res* **108**, 1392-1412 (2011).
167. Sider, K.L., Blaser, M.C. & Simmons, C.A. Animal models of calcific aortic valve disease. *Int J Inflamm* **2011**, 364310 (2011).
168. Abeyratne, L.R., Kingston, J.E., Onadim, Z. & Dubrey, S.W. Heritable retinoblastoma and accelerated aortic valve disease. *BMJ Case Rep* **2013**(2013).
169. Combs, M.D. & Yutzey, K.E. Heart valve development: regulatory networks in development and disease. *Circ Res* **105**, 408-421 (2009).
170. Schoen, F.J. Cardiac valves and valvular pathology: update on function, disease, repair, and replacement. *Cardiovasc Pathol* **14**, 189-194 (2005).
171. Kim, W., *et al.* RUNX1 is essential for mesenchymal stem cell proliferation and myofibroblast differentiation. *Proc Natl Acad Sci U S A* **111**, 16389-16394 (2014).
172. Ballatori, S.E. & Hinds, P.W. Osteosarcoma: prognosis plateau warrants retinoblastoma pathway targeted therapy. *Signal Transduction and Targeted Therapy* **1**, 16001 (2016).

173. Lebrun, J.J. The Dual Role of TGF β in Human Cancer: From Tumor Suppression to Cancer Metastasis. *ISRN Mol Biol* **2012**, 381428 (2012).
174. Nagy, E., *et al.* Upregulation of the 5-lipoxygenase pathway in human aortic valves correlates with severity of stenosis and leads to leukotriene-induced effects on valvular myofibroblasts. *Circulation* **123**, 1316-1325 (2011).
175. Galeone, A., Paparella, D., Colucci, S., Grano, M. & Brunetti, G. The role of TNF- α and TNF superfamily members in the pathogenesis of calcific aortic valvular disease. *ScientificWorldJournal* **2013**, 875363 (2013).
176. Miossec, P., Korn, T. & Kuchroo, V.K. Interleukin-17 and type 17 helper T cells. *N Engl J Med* **361**, 888-898 (2009).
177. Olsson, M., *et al.* Accumulation of T lymphocytes and expression of interleukin-2 receptors in nonrheumatic stenotic aortic valves. *J Am Coll Cardiol* **23**, 1162-1170 (1994).
178. Sherlock, J.P., *et al.* IL-23 induces spondyloarthritis by acting on ROR- γ t+ CD3+CD4-CD8- enthesial resident T cells. *Nat Med* **18**, 1069-1076 (2012).
179. Reinhardt, A., *et al.* Interleukin-23-Dependent γ/δ T Cells Produce Interleukin-17 and Accumulate in the Enthesis, Aortic Valve, and Ciliary Body in Mice. *Arthritis Rheumatol* **68**, 2476-2486 (2016).
180. Strupler, M., *et al.* Second harmonic imaging and scoring of collagen in fibrotic tissues. *Opt Express* **15**, 4054-4065 (2007).
181. Guvendiren, M., Perepelyuk, M., Wells, R.G. & Burdick, J.A. Hydrogels with differential and patterned mechanics to study stiffness-mediated myofibroblastic differentiation of hepatic stellate cells. *J Mech Behav Biomed Mater* **38**, 198-208 (2014).
182. Huebsch, N., *et al.* Harnessing traction-mediated manipulation of the cell/matrix interface to control stem-cell fate. *Nat Mater* **9**, 518-526 (2010).
183. Klein, E.A., *et al.* Cell-cycle control by physiological matrix elasticity and in vivo tissue stiffening. *Curr Biol* **19**, 1511-1518 (2009).
184. Xiao, Z., *et al.* Analysis of the extracellular matrix vesicle proteome in mineralizing osteoblasts. *J Cell Physiol* **210**, 325-335 (2007).
185. Frantz, C., Stewart, K.M. & Weaver, V.M. The extracellular matrix at a glance. *J Cell Sci* **123**, 4195-4200 (2010).
186. Licup, A.J., *et al.* Stress controls the mechanics of collagen networks. *Proc Natl Acad Sci U S A* **112**, 9573-9578 (2015).

187. Baldock, C., *et al.* The supramolecular organization of fibrillin-rich microfibrils. *J Cell Biol* **152**, 1045-1056 (2001).
188. Li, D., Clark, C.C. & Myers, J.C. Basement membrane zone type XV collagen is a disulfide-bonded chondroitin sulfate proteoglycan in human tissues and cultured cells. *J Biol Chem* **275**, 22339-22347 (2000).
189. Sabatelli, P., *et al.* Collagen VI deficiency affects the organization of fibronectin in the extracellular matrix of cultured fibroblasts. *Matrix Biol* **20**, 475-486 (2001).
190. Schroeder, J.A., Jackson, L.F., Lee, D.C. & Camenisch, T.D. Form and function of developing heart valves: coordination by extracellular matrix and growth factor signaling. *J Mol Med (Berl)* **81**, 392-403 (2003).
191. Johnson, J.L., *et al.* Regulation of matrix metalloproteinase genes by E2F transcription factors: Rb-Raf-1 interaction as a novel target for metastatic disease. *Cancer Res* **72**, 516-526 (2012).
192. Anstine, L.J., Horne, T.E., Horwitz, E.M. & Lincoln, J. Contribution of Extra-Cardiac Cells in Murine Heart Valves is Age-Dependent. *Journal of American Heart Association* **6**, e007097 (2017).
193. Fang, M., Alfieri, C.M., Hulin, A., Conway, S.J. & Yutzey, K.E. Loss of β -catenin promotes chondrogenic differentiation of aortic valve interstitial cells. *Arterioscler Thromb Vasc Biol* **34**, 2601-2608 (2014).
194. Wu, B., *et al.* Nfatc1 coordinates valve endocardial cell lineage development required for heart valve formation. *Circ Res* **109**, 183-192 (2011).
195. Nkomo, V.T., *et al.* Burden of valvular heart diseases: a population-based study. *The Lancet* **368**, 1005-1011 (2006).
196. Sider, K.L., Blaser, M.C. & Simmons, C.A. Animal models of calcific aortic valve disease. *International journal of inflammation* **2011**(2011).
197. Dweck, M., *et al.* 18F-SODIUM FLUORIDE IS A MARKER OF ACTIVE CALCIFICATION AND DISEASE PROGRESSION IN PATIENTS WITH AORTIC STENOSIS. *Journal of the American College of Cardiology* **61**, E836 (2013).
198. Vesey, A., Dweck, M. & Newby, D. PET/CT Imaging of Inflammation and Calcification in CAVD: Clinical Studies. in *Cardiovascular Imaging* (ed. Aikawa, E.) 201-223 (Springer International Publishing, 2015).
199. Williams, R.M., Zipfel, W.R. & Webb, W.W. Multiphoton microscopy in biological research. *Current Opinion in Chemical Biology* **5**, 603-608 (2001).
200. Georgakoudi, I. & Quinn, K.P. Optical imaging using endogenous contrast to assess metabolic state. *Annu Rev Biomed Eng* **14**, 351-367 (2012).

201. So, P.T., Dong, C.Y., Masters, B.R. & Berland, K.M. Two-photon excitation fluorescence microscopy. *Annu Rev Biomed Eng* **2**, 399-429 (2000).
202. Zipfel, W.R., *et al.* Live tissue intrinsic emission microscopy using multiphoton-excited native fluorescence and second harmonic generation. *Proceedings of the National Academy of Sciences* **100**, 7075-7080 (2003).
203. Cui, J.Z., *et al.* Quantification of aortic and cutaneous elastin and collagen morphology in Marfan syndrome by multiphoton microscopy. *Journal of Structural Biology* **187**, 242-253 (2014).
204. König, K., Schenke-Layland, K., Riemann, I. & Stock, U. Multiphoton autofluorescence imaging of intratissue elastic fibers. *Biomaterials* **26**, 495-500 (2005).
205. Fitzmaurice, M., *et al.* Argon ion laser-excited autofluorescence in normal and atherosclerotic aorta and coronary arteries: Morphologic studies. *American Heart Journal* **118**, 1028-1038 (1989).
206. Benninger, R.K. & Piston, D.W. Two-photon excitation microscopy for the study of living cells and tissues. *Current protocols in cell biology*, 4.11. 11-14.11. 24 (2013).
207. Huang, S., Heikal, A.A. & Webb, W.W. Two-photon fluorescence spectroscopy and microscopy of NAD(P)H and flavoprotein. *Biophys J* **82**, 2811-2825 (2002).
208. Croce, A. & Bottiroli, G. Autofluorescence spectroscopy and imaging: a tool for biomedical research and diagnosis. *European Journal of Histochemistry* **58**(2014).
209. Perry, S.W., Burke, R.M. & Brown, E.B. Two-photon and second harmonic microscopy in clinical and translational cancer research. *Annals of biomedical engineering* **40**, 277-291 (2012).
210. Chen, X., Nadiarynk, O., Plotnikov, S. & Campagnola, P.J. Second harmonic generation microscopy for quantitative analysis of collagen fibrillar structure. *Nature protocols* **7**, 654 (2012).
211. Sullivan, K., Quinn, K., Tang, K., Georgakoudi, I. & Black, L., III. Extracellular matrix remodeling following myocardial infarction influences the therapeutic potential of mesenchymal stem cells. *Stem Cell Res Ther* **5**, 1-16 (2014).
212. Cho, A., Suzuki, S., Hatakeyama, J., Haruyama, N. & Kulkarni, A.B. A Method for Rapid Demineralization of Teeth and Bones. *The Open Dentistry Journal* **4**, 223-229 (2010).
213. Liao, P.-S., Chen, T.-S. & Chung, P.-C. A fast algorithm for multilevel thresholding. *J. Inf. Sci. Eng.* **17**, 713-727 (2001).

214. Levitt, J.M., *et al.* Diagnostic cellular organization features extracted from autofluorescence images. *Optics letters* **32**, 3305-3307 (2007).
215. Xylas, J., Alt-Holland, A., Garlick, J., Hunter, M. & Georgakoudi, I. Intrinsic optical biomarkers associated with the invasive potential of tumor cells in engineered tissue models. *Biomedical optics express* **1**, 1387-1400 (2010).
216. Xylas, J., *et al.* Noninvasive assessment of mitochondrial organization in three-dimensional tissues reveals changes associated with cancer development. *Int J Cancer* **136**, 322-332 (2015).
217. Pouli, D., *et al.* Imaging mitochondrial dynamics in human skin reveals depth-dependent hypoxia and malignant potential for diagnosis. *Sci Transl Med* **8**, 367ra169 (2016).
218. Tanaka, K., *et al.* Age-associated aortic stenosis in apolipoprotein E-deficient mice. *J Am Coll Cardiol* **46**, 134-141 (2005).
219. Zeadin, M., *et al.* Effect of leptin on vascular calcification in apolipoprotein E-deficient mice. *Arteriosclerosis, thrombosis, and vascular biology* **29**, 2069-2075 (2009).
220. Cicchi, R., *et al.* Scoring of collagen organization in healthy and diseased human dermis by multiphoton microscopy. *Journal of Biophotonics* **3**, 34-43 (2010).
221. Williams, R.M., Zipfel, W.R. & Webb, W.W. Interpreting second-harmonic generation images of collagen I fibrils. *Biophys J* **88**, 1377-1386 (2005).
222. Campagnola, P.J. & Loew, L.M. Second-harmonic imaging microscopy for visualizing biomolecular arrays in cells, tissues and organisms. *Nature biotechnology* **21**, 1356-1360 (2003).
223. Liu, Z., *et al.* Rapid three-dimensional quantification of voxel-wise collagen fiber orientation. *Biomedical optics express* **6**, 2294-2310 (2015).
224. Liu, Z., *et al.* Automated quantification of three-dimensional organization of fiber-like structures in biological tissues. *Biomaterials* **116**, 34-47 (2017).
225. Zoumi, A., Yeh, A. & Tromberg, B.J. Imaging cells and extracellular matrix in vivo by using second-harmonic generation and two-photon excited fluorescence. *Proceedings of the National Academy of Sciences of the United States of America* **99**, 11014-11019 (2002).
226. Richards-Kortum, R. & Sevick-Muraca, E. Quantitative optical spectroscopy for tissue diagnosis. *Annu Rev Phys Chem* **47**, 555-606 (1996).
227. Berzina-Cimdina, L. & Borodajenko, N. Research of calcium phosphates using Fourier transform infrared spectroscopy. in *Infrared Spectroscopy-Materials Science, Engineering and Technology* (InTech, 2012).

228. Ko, A.C.T., *et al.* Multimodal nonlinear optical imaging of atherosclerotic plaque development in myocardial infarction-prone rabbits. *Journal of Biomedical Optics* **15**, 020501-020501-020503 (2010).
229. Verbunt, R.J.A.M., *et al.* Characterization of ultraviolet laser-induced autofluorescence of ceroid deposits and other structures in atherosclerotic plaques as a potential diagnostic for laser angioplasty. *American Heart Journal* **123**, 208-216 (1992).
230. Le, T.T., Langohr, I.M., Locker, M.J., Sturek, M. & Cheng, J.-X. Label-free molecular imaging of atherosclerotic lesions using multimodal nonlinear optical microscopy. *Journal of Biomedical Optics* **12**, 054007-054007-054010 (2007).
231. O'Brien, K.D. Pathogenesis of calcific aortic valve disease: a disease process comes of age (and a good deal more). *Arteriosclerosis, thrombosis, and vascular biology* **26**, 1721-1728 (2006).
232. Evans, C.L. & Xie, X.S. Coherent anti-Stokes Raman scattering microscopy: chemical imaging for biology and medicine. *Annu. Rev. Anal. Chem.* **1**, 883-909 (2008).
233. Giachelli, C.M. Ectopic calcification. *The American journal of pathology* **154**, 671-675 (1999).
234. Richards-Kortum, R., *et al.* Spectroscopic diagnosis of colonic dysplasia. *Photochemistry and photobiology* **53**, 777-786 (1991).
235. Guerraty, M. & Mohler, E.R. Models of aortic valve calcification. *Journal of Investigative Medicine* **55**, 278-283 (2007).
236. Hutcheson, J.D., *et al.* Genesis and growth of extracellular-vesicle-derived microcalcification in atherosclerotic plaques. *Nature materials* (2016).
237. Clark, C.R., Bowler, M.A., Snider, J.C. & Merryman, W.D. Targeting Cadherin-11 Prevents Notch1-Mediated Calcific Aortic Valve Disease. *Circulation* **135**, 2448-2450 (2017).
238. Perosky, J.E., *et al.* Early detection of heterotopic ossification using near-infrared optical imaging reveals dynamic turnover and progression of mineralization following Achilles tenotomy and burn injury. *Journal of Orthopaedic Research* **32**, 1416-1423 (2014).
239. Zhang, Y., *et al.* A compact fiber-optic SHG scanning endomicroscope and its application to visualize cervical remodeling during pregnancy. *Proceedings of the National Academy of Sciences of the United States of America* **109**, 12878-12883 (2012).
240. Murari, K., *et al.* Compensation-free, all-fiber-optic, two-photon endomicroscopy at 1.55 μm . *Optics letters* **36**, 1299-1301 (2011).

241. Nishimura, R., *et al.* 2014 AHA/ACC guideline for the management of patients with valvular heart disease: executive summary: a report of the American College of Cardiology/American Heart Association Task Force on Practice Guidelines. *J Am Coll Cardiol* 2014; 63: 2438-88. Correction. *Journal of the American College of Cardiology* **63**(2014).
242. Mathieu, P., *et al.* The pathology and pathobiology of bicuspid aortic valve: state of the art and novel research perspectives. *The Journal of Pathology: Clinical Research* **1**, 195-206 (2015).
243. Sethuraman, S., Amirian, J.H., Litovsky, S.H., Smalling, R.W. & Emelianov, S.Y. Spectroscopic intravascular photoacoustic imaging to differentiate atherosclerotic plaques. *Optics express* **16**, 3362-3367 (2008).
244. Wang, B., *et al.* Intravascular Photoacoustic Imaging. *IEEE journal of quantum electronics* **16**, 588-599 (2010).
245. Fu, H.L., *et al.* Flexible miniature compound lens design for high-resolution optical coherence tomography balloon imaging catheter. *J Biomed Opt* **13**, 060502 (2008).
246. Hassan, T., Piton, N., Lachkar, S., Salaun, M. & Thiberville, L. A Novel Method for In Vivo Imaging of Solitary Lung Nodules Using Navigational Bronchoscopy and Confocal Laser Microendoscopy. *Lung* **193**, 773-778 (2015).
247. Achenbach, S., *et al.* Detection of calcified and noncalcified coronary atherosclerotic plaque by contrast-enhanced, submillimeter multidetector spiral computed tomography: a segment-based comparison with intravascular ultrasound. *Circulation* **109**, 14-17 (2004).
248. Radi, M.J. Calcium oxalate crystals in breast biopsies. An overlooked form of microcalcification associated with benign breast disease. *Arch Pathol Lab Med* **113**, 1367-1369 (1989).
249. Guauque-Olarte, S., *et al.* RNA expression profile of calcified bicuspid, tricuspid, and normal human aortic valves by RNA sequencing. *Physiological genomics* **48**, 749-761 (2016).
250. Otto, C.M., Lind, B.K., Kitzman, D.W., Gersh, B.J. & Siscovick, D.S. Association of aortic-valve sclerosis with cardiovascular mortality and morbidity in the elderly. *New England Journal of Medicine* **341**, 142-147 (1999).
251. Hinton Jr, R.B., *et al.* Mouse heart valve structure and function: echocardiographic and morphometric analyses from the fetus through the aged adult. *American Journal of Physiology-Heart and Circulatory Physiology* **294**, H2480-H2488 (2008).
252. Bowler, M.A. & Merryman, W.D. In vitro models of aortic valve calcification: solidifying a system. *Cardiovascular Pathology* **24**, 1-10 (2015).

253. Wang, Z., Gerstein, M. & Snyder, M. RNA-Seq: a revolutionary tool for transcriptomics. *Nature reviews genetics* **10**, 57-63 (2009).
254. Matkovich, S.J., Zhang, Y., Van Booven, D.J. & Dorn, G.W. Deep mRNA sequencing for in vivo functional analysis of cardiac transcriptional regulators. *Circulation research* **106**, 1459-1467 (2010).
255. Lee, J.-H., *et al.* Analysis of Transcriptome Complexity Through RNA Sequencing in Normal and Failing Murine Hearts Novelty and Significance. *Circulation research* **109**, 1332-1341 (2011).
256. Wiltz, D., *et al.* Extracellular matrix organization, structure, and function. in *Calcific aortic valve disease* (InTech, 2013).
257. Brigham, M.D., *et al.* Mechanically robust and bioadhesive collagen and photocrosslinkable hyaluronic acid semi-interpenetrating networks. *Tissue Engineering Part A* **15**, 1645-1653 (2008).
258. Jensen, L.J., *et al.* STRING 8—a global view on proteins and their functional interactions in 630 organisms. *Nucleic acids research* **37**, D412-D416 (2008).
259. Fenn, S.L. & Oldinski, R.A. Visible light crosslinking of methacrylated hyaluronan hydrogels for injectable tissue repair. *Journal of Biomedical Materials Research Part B: Applied Biomaterials* **104**, 1229-1236 (2016).
260. Gould, R.A. & Butcher, J.T. Isolation of valvular endothelial cells. *Journal of visualized experiments: JoVE* (2010).
261. Lee, J.M. & Yeong, W.Y. A preliminary model of time-pressure dispensing system for bioprinting based on printing and material parameters: This paper reports a method to predict and control the width of hydrogel filament for bioprinting applications. *Virtual and Physical Prototyping* **10**, 3-8 (2015).
262. Thanassoulis, G., *et al.* Genetic associations with valvular calcification and aortic stenosis. *New England Journal of Medicine* **368**, 503-512 (2013).
263. Smith, J.G., *et al.* Association of low-density lipoprotein cholesterol-related genetic variants with aortic valve calcium and incident aortic stenosis. *Jama* **312**, 1764-1771 (2014).
264. Bossé, Y., Mathieu, P. & Pibarot, P. Genomics: the next step to elucidate the etiology of calcific aortic valve stenosis. *Journal of the American College of Cardiology* **51**, 1327-1336 (2008).
265. Burdick, J.A. & Prestwich, G.D. Hyaluronic acid hydrogels for biomedical applications. *Advanced materials* **23**(2011).

266. Xu, X., Jha, A.K., Harrington, D.A., Farach-Carson, M.C. & Jia, X. Hyaluronic acid-based hydrogels: from a natural polysaccharide to complex networks. *Soft matter* **8**, 3280-3294 (2012).
267. Kalamajski, S. & Oldberg, Å. The role of small leucine-rich proteoglycans in collagen fibrillogenesis. *Matrix Biology* **29**, 248-253 (2010).
268. Ueda, K., *et al.* Possible dual role of decorin in abdominal aortic aneurysm. *PLoS one* **10**, e0120689 (2015).
269. Sand, J.M.B., Genovese, F. & Karsdal, M.A. Chapter 4 - Type IV Collagen. in *Biochemistry of Collagens, Laminins and Elastin* 31-41 (Academic Press, 2016).
270. Watson, K.E., Parhami, F., Shin, V. & Demer, L.L. Fibronectin and collagen I matrixes promote calcification of vascular cells in vitro, whereas collagen IV matrix is inhibitory. *Arteriosclerosis, thrombosis, and vascular biology* **18**, 1964-1971 (1998).
271. Foldager, C.B., Toh, W.S., Gomoll, A.H., Olsen, B.R. & Spector, M. Distribution of basement membrane molecules, laminin and collagen type IV, in normal and degenerated cartilage tissues. *Cartilage* **5**, 123-132 (2014).
272. Snider, P., *et al.* Periostin is required for maturation and extracellular matrix stabilization of noncardiomyocyte lineages of the heart. *Circulation research* **102**, 752-760 (2008).
273. Conway, S.J., Doetschman, T. & Azhar, M. The inter-relationship of periostin, TGF β , and BMP in heart valve development and valvular heart diseases. *The Scientific World Journal* **11**, 1509-1524 (2011).
274. Hakuno, D., *et al.* Periostin advances atherosclerotic and rheumatic cardiac valve degeneration by inducing angiogenesis and MMP production in humans and rodents. *The Journal of clinical investigation* **120**, 2292 (2010).
275. Tkatchenko, T.V., *et al.* Lack of periostin leads to suppression of Notch1 signaling and calcific aortic valve disease. *Physiological genomics* **39**, 160-168 (2009).
276. Lincoln, J., Lange, A.W. & Yutzey, K.E. Hearts and bones: shared regulatory mechanisms in heart valve, cartilage, tendon, and bone development. *Developmental biology* **294**, 292-302 (2006).
277. Zhu, W., Mow, V.C., Rosenberg, L.C. & Tang, L.-H. Determination of kinetic changes of aggrecan-hyaluronan interactions in solution from its rheological properties. *Journal of biomechanics* **27**, 571-579 (1994).
278. Chang, W., Tu, C., Pratt, S., Chen, T.-H. & Shoback, D. Extracellular Ca²⁺-sensing receptors modulate matrix production and mineralization in chondrogenic RCJ3.1C5.18 cells. *Endocrinology* **143**, 1467-1474 (2002).

279. Aykan, A.C., *et al.* Value of serum fibrinogen levels in the assessment of mechanical prosthetic valve thrombosis. *J Heart Valve Dis* **23**(2014).
280. Lip, G.Y., Rumley, A., Dunn, F.G. & Lowe, G.D. Thrombogenesis in mitral regurgitation and aortic stenosis. *Angiology* **47**, 1117-1125 (1996).
281. Gravallesse, E.M. Osteopontin: a bridge between bone and the immune system. *Journal of Clinical Investigation* **112**, 147 (2003).
282. Sosa-García, B., *et al.* A role for the retinoblastoma protein as a regulator of mouse osteoblast cell adhesion: implications for osteogenesis and osteosarcoma formation. *PLoS One* **5**, e13954 (2010).
283. Gündüz, V., Kong, E., Bryan, C.D. & Hinds, P.W. Loss of the retinoblastoma tumor suppressor protein in murine calvaria facilitates immortalization of osteoblast-adipocyte bipotent progenitor cells characterized by low expression of N-cadherin. *Molecular and cellular biology* **32**, 2561-2569 (2012).
284. Monroe, D.G., Hawse, J.R., Subramaniam, M. & Spelsberg, T.C. Retinoblastoma binding protein-1 (RBP1) is a Runx2 coactivator and promotes osteoblastic differentiation. *BMC musculoskeletal disorders* **11**, 104 (2010).
285. Luan, Y., *et al.* The retinoblastoma protein is an essential mediator of osteogenesis that links the p204 protein to the Cbfa1 transcription factor thereby increasing its activity. *Journal of Biological Chemistry* **282**, 16860-16870 (2007).
286. Balla, M.M., Vemuganti, G.K., Kannabiran, C., Honavar, S.G. & Murthy, R. Phenotypic characterization of retinoblastoma for the presence of putative cancer stem-like cell markers by flow cytometry. *Investigative ophthalmology & visual science* **50**, 1506-1514 (2009).
287. Pietras, A., *et al.* Osteopontin-CD44 signaling in the glioma perivascular niche enhances cancer stem cell phenotypes and promotes aggressive tumor growth. *Cell stem cell* **14**, 357-369 (2014).
288. Liu, G.-X., *et al.* OPN promotes survival of activated T cells by up-regulating CD44 in patients with oral lichen planus. *Clinical Immunology* **138**, 291-298 (2011).
289. Huang, P., *et al.* BMP-2 induces EMT and breast cancer stemness through Rb and CD44. *Cell death discovery* **3**, 17039 (2017).
290. Eveborn, G.W., Schirmer, H., Heggelund, G., Lunde, P. & Rasmussen, K. The evolving epidemiology of valvular aortic stenosis. the Tromsø study. *Heart* **99**, 396-400 (2013).
291. Last, J.A., King, T., Nerlich, A. & Reiser, K.M. Collagen cross-linking in adult patients with acute and chronic fibrotic lung disease. *Am Rev Respir Dis* **141**, 307-313 (1990).

292. Snedeker, J.G. & Gautieri, A. The role of collagen crosslinks in ageing and diabetes-the good, the bad, and the ugly. *Muscles, ligaments and tendons journal* **4**, 303 (2014).
293. Eyre, D.R., Weis, M.A. & Wu, J.-J. Advances in collagen cross-link analysis. *Methods* **45**, 65-74 (2008).
294. Brüel, A. & Oxlund, H. Changes in biomechanical properties, composition of collagen and elastin, and advanced glycation endproducts of the rat aorta in relation to age. *Atherosclerosis* **127**, 155-165 (1996).
295. Stephens, E.H., de Jonge, N., McNeill, M.P., Durst, C.A. & Grande-Allen, K.J. Age-related changes in material behavior of porcine mitral and aortic valves and correlation to matrix composition. *Tissue Eng Part A* **16**, 867-878 (2010).
296. Avery, N. & Bailey, A. Enzymic and non-enzymic cross-linking mechanisms in relation to turnover of collagen: relevance to aging and exercise. *Scandinavian journal of medicine & science in sports* **15**, 231-240 (2005).
297. Reigle, K.L., *et al.* Non-enzymatic glycation of type I collagen diminishes collagen–proteoglycan binding and weakens cell adhesion. *Journal of cellular biochemistry* **104**, 1684-1698 (2008).
298. Tomasek, J.J., Meyers, S.W., Basinger, J.B., Green, D.T. & Shew, R.L. Diabetic and age-related enhancement of collagen-linked fluorescence in cortical bones of rats. *Life sciences* **55**, 855-861 (1994).
299. Branchetti, E., *et al.* Circulating Soluble Receptor for Advanced Glycation End Product Identifies Patients With Bicuspid Aortic Valve and Associated AortopathiesSignificance. *Arteriosclerosis, thrombosis, and vascular biology* **34**, 2349-2357 (2014).
300. Reddy, G.K. Cross-linking in collagen by nonenzymatic glycation increases the matrix stiffness in rabbit achilles tendon. *Experimental Diabetes Research* **5**, 143-153 (2004).
301. Yamamoto, M. & Sugimoto, T. Advanced glycation end products, diabetes, and bone strength. *Current osteoporosis reports* **14**, 320-326 (2016).
302. Alikhani, M., *et al.* Advanced glycation end products stimulate osteoblast apoptosis via the MAP kinase and cytosolic apoptotic pathways. *Bone* **40**, 345-353 (2007).
303. Valcourt, U., *et al.* Non-enzymatic glycation of bone collagen modifies osteoclastic activity and differentiation. *Journal of Biological Chemistry* **282**, 5691-5703 (2007).
304. Burr, D.B. Bone quality: understanding what matters. (2004).

305. Taki, K., Takayama, F., Tsuruta, Y. & Niwa, T. Oxidative stress, advanced glycation end product, and coronary artery calcification in hemodialysis patients. *Kidney international* **70**, 218-224 (2006).
306. Münch, G., *et al.* Influence of advanced glycation end-products and AGE-inhibitors on nucleation-dependent polymerization of β -amyloid peptide. *Biochimica et Biophysica Acta (BBA)-Molecular Basis of Disease* **1360**, 17-29 (1997).
307. Hutcheson, J.D., *et al.* Genesis and growth of extracellular-vesicle-derived microcalcification in atherosclerotic plaques. *Nat Mater* **15**, 335-343 (2016).
308. Marturano, J.E., Xylas, J.F., Sridharan, G.V., Georgakoudi, I. & Kuo, C.K. Lysyl oxidase-mediated collagen crosslinks may be assessed as markers of functional properties of tendon tissue formation. *Acta biomaterialia* **10**, 1370-1379 (2014).
309. Paschalis, E., *et al.* Spectroscopic characterization of collagen cross-links in bone. *Journal of Bone and Mineral Research* **16**, 1821-1828 (2001).
310. Mathieu, P., Bouchareb, R. & Boulanger, M.-C. Innate and adaptive immunity in calcific aortic valve disease. *Journal of immunology research* **2015**(2015).
311. Yu, Z., *et al.* Tumor necrosis factor- α accelerates the calcification of human aortic valve interstitial cells obtained from patients with calcific aortic valve stenosis via the BMP2-Dlx5 pathway. *Journal of Pharmacology and Experimental Therapeutics* **337**, 16-23 (2011).
312. El Hussein, D., *et al.* P2Y2 receptor represses IL-6 expression by valve interstitial cells through Akt: implication for calcific aortic valve disease. *Journal of molecular and cellular cardiology* **72**, 146-156 (2014).
313. Miossec, P., Korn, T. & Kuchroo, V.K. Interleukin-17 and type 17 helper T cells. *New England Journal of Medicine* **361**, 888-898 (2009).
314. Zhou, L., *et al.* TGF- β -induced Foxp3 inhibits TH17 cell differentiation by antagonizing ROR γ t function. *Nature* **453**, 236-240 (2008).
315. Skurikhin, E., *et al.* Response of Inflammatory Mediators, Extracellular Matrix Proteins and Stem and Progenitor Cells to Emphysema. *Bulletin of experimental biology and medicine* **161**, 566-570 (2016).
316. Jiang, D., Liang, J. & Noble, P.W. Hyaluronan as an immune regulator in human diseases. *Physiological reviews* **91**, 221-264 (2011).
317. Litwiniuk, M., Krejner, A., Speyrer, M., Gauto, A. & Grzela, T. Hyaluronic Acid in Inflammation and Tissue Regeneration. *Wounds: a compendium of clinical research and practice* **28**, 78-88 (2016).